Aerodynamics of a freight train passing through a tunnel

Panagiotis Iliadis

A thesis submitted to the University of Birmingham for the degree of

DOCTOR OF PHILOSOPHY

School of Engineering

College of Engineering and Physical Science

University of Birmingham

August 2019

Abstract

This research aims to investigate the pressure transients, flow separation and slipstream velocities around a freight train passing through a tunnel. The methodology consists of moving model-scale experiments at the TRAIN Rig and numerical simulations using unsteady RANS combined with the sliding mesh technique. The 1/25th scaled model represents a Class 66 locomotive connected to container wagons, entering a circular tunnel at 33.5m/s with a blockage ratio of 0.202. The effects of loading configuration, nose roundness, train length and speed are examined and the results are synthesized with 1D analytical modelling for further analysis.

For the first time, it is shown that for partially loaded trains, the maximum pressure rise inside the tunnel can occur after the initial compression wave. This is attributed to the generation of low energy waves in the gaps between containers. Independent of the loading configuration, the blunt nose of the Class 66 locomotive produces a single part pressure gradient for the initial compression wave, contrary to the two-gradient rise caused by rounded noses. This pressure rise is defined by the large separation bubble around the blunt nose, which reduces the effective area and increases the blockage ratio. As the train enters the confined space of the tunnel, the separation length reduces by 31% at the sides and 32% at the roof, compared to open air. Then, its size remains unchanged throughout the tunnel with maximum lengths observed at the mid-vertical and mid-lateral positions. Separation affects the slipstream velocities which are also maximum at these locations. Velocities change with time as they are affected by the pressure waves and the position of the train along the tunnel length.

Acknowledgements

During this journey, there have been a number of people who contributed to this project and supported me, both technically and personally.

First of all, I would like to thank my supervisors Professor Chris J. Baker, Dr Hassan Hemida and Dr David Soper for introducing me to the scientific world and their continuous support during this PhD. Their expertise in the subject, provision of constructive feedback and their availability for discussions and meetings, were critical in the success of this research project. Special thanks for trusting me and letting the experimental facilities in my hands as well as for providing me with the required computational resources.

In addition, I would like to thank Drs Dominic Flynn and Mingzhe He, Mr. Frederick Bourriez, Mr. Giulio Vita and Miss Anam Hashmi for their help and willingness to travel to the TRAIN Rig and assist me with the experiments.

I am also thankful to a number of people who reviewed my research and acknowledged its importance. Professors Mark Sterling and John Bridgeman were my internal reviewers during this PhD and gave me useful advice for the overall direction of the research. Another important contribution to the quality of this thesis was made by the five anonymous reviewers of the two journal papers published, who acknowledged the novelty of the research and made constructive comments.

On a personal level, I am really grateful to my parents and brother whose love and support is with me throughout my whole life and they were always there when I needed them.

Last but by no means least, I would like to thank my partner Vily for always being by my side during this journey. Her love, support and personal sacrifices are invaluable to me.

Contents

List of figures

List of tables

Nomenclature

Principal symbols

A	Cross sectional area of the tunnel (m^2)
a	Speed of sound (m/s)
Cp	Pressure coefficient
c_{PR}	Specific heat capacity at constant pressure
H	Maximum height of separation bubble vortex
h	Locomotive height (m)
I	Turbulence Intensity (%)
k	Turbulence Kinetic Energy (J/kg)
L	Locomotive length (m)
l	Distance from the tunnel entrance (m)
p	Pressure (Pa)
p_{abs}	Absolute pressure (Pa)
R	Universal gas constant (Joules / (moles • Kelvin))
Re	Reynolds number (-)
r	Residual
T	Temperature (K)
t	Time (s)
t*	Dimensionless time

U	Air velocity (m/s)
U_x	Longitudinal component of flow velocity (m/s)
V	Train speed (m/s)
w	Molecular weight (kg/mol)
v	Volume (m^3)
x	Distance from the origin of the longitudinal axis (m)
y	Distance from the origin of the vertical axis (m)
Z	Acoustic impedance ($Pa \cdot s/m^3$)
z	Distance from the origin of the lateral axis (m)
ρ	Density (kg/m^3)
μ	Dynamic viscosity ($Pa \cdot s$)
τ	Wall shear stress (Pa)
ω	Specific Dissipation rate (s^{-1})

Subscripts

p_N	The pressure rise caused by the train nose entry (Pa)
p_{Fr}	The second part of pressure rise including friction effects (Pa)
p_{SP}	The pressure rise caused by the separation bubble entry (Pa)
p_T	The change in pressure as the tail enters the tunnel (Pa)

List of Abbreviations

1D	One-dimensional
3D	Three-dimensional
CEL	CFX Expression Language
CEN	European Committee for Standardization (COMITÉ EUROPÉEN DE NORMALISATION)
CFD	Computational Fluid Dynamics
DDES	Delayed Detached Eddy Simulations
DNS	Direct Numerical Simulations
LES	Large Eddy Simulations
RAIB	Rail Accident Investigation Branch
RANS	Reynolds-Averaged Navier-Stokes equations
TSI	Technical Specifications for Interoperability

Chapter 1

Introduction

1.1 Outline of studies

This thesis presents an investigation on the pressure transients, flow separation and velocity field around a freight train passing through a tunnel. Two methods are used; physical experiments using a moving scaled model and computational simulations using the sliding mesh technique. The results from the two methods are synthesized with analytical formulae to assess the suitability of current 1D models for the cases of this study and to provide additional information. Chronologically, the experiments were conducted first, analysing the pressure transients inside the tunnel and pointing towards the important areas that need further investigation through numerical simulations. The simulations form a larger part of this study and, following an experimental validation, explore areas which are less accessible through physical tests.

The results of this study have been published in two journal and two conference papers, listed below:

Journal papers:

- Iliadis, P., Soper, D., Baker, C., & Hemida, H. (2018). *Experimental investigation of the aerodynamics of a freight train passing through a tunnel using a moving model*. *Proceedings of the Institution of Mechanical Engineers, Part F: Journal of Rail and Rapid Transit*.
- Iliadis, P., Hemida, H., Soper, D. & Baker, C. (2019). *Numerical simulations of the separated flow around a freight train passing through a tunnel using the sliding mesh technique. Proceedings of the Institution of Mechanical Engineers, Part F: Journal of Rail and Rapid Transit*.

Conference papers:

- P. Iliadis (2016), C. Baker, H. Hemida, D. Soper. Aerodynamics of a Freight Train Passing Through a Tunnel. Paper presented at the *Proceedings of the* 12th *UK* Conference on *Wind Engineering*, University of Nottingham, Nottingham, 5-7 September (pp. 143-146)

- P. Iliadis (2018), H. Hemida, C. Baker, D. Soper. *A CFD analysis on the aerodynamics of a freight train passing through a tunnel.* Paper presented at The Fourth International Conference on Railway Technology, Sitges, Barcelona, Spain, 3-7 September

1.2 Background

1.2.1 Significance of freight train aerodynamics

‘’Increasing the speed of freight trains creates the potential to expand the capacity of the UK rail network, which is one of the reasons researchers have recently investigated the aerodynamics of freight trains (Flynn et al., 2014,Soper, Baker and Sterling, 2015)’’ (Iliadis et al., 2019, p. 1). ‘’The majority of train aerodynamics research has traditionally tended to focus on passenger trains rather than on freight trains. The focus on higher speed passenger trains (Howe, 1999,Kwon et al., 2006,Gilbert, Baker and Quinn, 2013) is justified by the fact that in very broad terms the aerodynamic forces in open air conditions present a proportional relation to the square of velocity (Baker, 2014 b). Consequently, amplitudes of pressure change proportionally to the square of speed (Li et al., 2011)’’ (Iliadis et al., 2018, p. 1).

In light of the potential increases in freight train speeds, flow phenomena that have been studied for passenger trains in the past, now need to be considered for freight trains as well. Results from aerodynamic investigations can help engineers to design more efficient and safer freight trains in the future.

1.2.2 Differences between freight and passenger trains

The speed at which freight trains operate is lower than passenger trains, with exact figures varying across the world. In the UK, the maximum operating speed is 75mph (33.5m/s) for freight trains and 186mph (83.15m/s) for passenger trains. With a potential rise in operating speed, aerodynamic characteristics such as slipstream and

crosswind velocities, tunnel pressure transients and drag generation are expected to become more critical. These characteristics are more intense for freight trains (see Chapter 2), which is a limiting factor for equalizing their speed to passenger trains. Therefore, a speed increase should be accompanied by geometric improvements at the nose of the train (as found in the current study), following a detailed aerodynamic investigation of the current shapes. The blunt nose shape of freight trains is one of the most distinct differences with passenger trains. However, it must be mentioned that there are loco-hauled or multiple unit passenger trains that have non-streamlined nose and may share aerodynamic features of both types.

Another unique characteristic of freight trains is that they may consist of partially loaded wagons. The importance of this unique characteristic of freight trains is proved through the focus of recent research in the topic. In open air, this can result in complex flow phenomena in the empty space between containers. However, it is unknown whether the loading configuration can influence complex flow phenomena such as the pressure transients generated when a train passes through a tunnel. This is due to the absence of research on such cases.

1.2.3 **Freight trains in tunnels**

Although there has been extensive research on the aerodynamics of trains in tunnels, freight trains have not been studied in detail. The complex flow phenomena generated during the train's journey through the tunnel depend on a number of geometric and flow parameters. These parameters are discussed in detail in Chapter 2 of this thesis.

One of them is the nose shape, which as discussed above is blunt for freight trains and its effects require investigations. As mentioned before, the other unique characteristic of freight trains is the loading configuration. This is another characteristic that needs investigation, as the discontinuous main body of freight trains differs from passenger trains, where most of the knowledge in tunnel aerodynamics is coming from.

1.2.4 Applicability of analytical formulas for freight trains in tunnels

It is common to use 1D analytical formulae to calculate flow characteristics such as the initial pressure rise for trains in tunnels. However, the applicability of these formulas for the unique characteristics of freight trains such as the blunt nose and partial loading has not been examined. Regarding the former characteristic, although these formulas allow for a different nose coefficient to be used, they have been built around noses which are likely to cause significantly less levels of flow separation. The latter characteristic attracts interest because all current formulas assume a constant cross section area of the main body of the train. This is in contrast to partially loaded freight trains of which the cross sectional area can vary along their length.

1.2.5 Compliance with regulations

Trains in tunnels need to conform to specific limits related to the initial pressure rise after the train's nose entry, as this is the maximum increase during its journey.

Compliance of freight trains with current regulations and the effect of speed increase need to be assessed. Then, potential modifications for reducing pressure rises can be recommended.

1.3 Aim and objectives

The primary aim of this study is to investigate the aerodynamics of a freight train passing through a tunnel in order to provide information for future train design and to assess compliance with current regulations.

In order to achieve this aim, the following objectives have been identified:

- Plan and develop an experimental methodology for providing the pressure time histories at various locations inside the tunnel, at the entrance portal and on the train surface.
- Create a CAD model which best represents the real geometry and develop a numerical methodology which accurately captures all flow effects (pressure transients, separation and velocity magnitudes) around the train.
- Investigate the pressure transients generated by the Class 66 locomotive connected to container wagons and unravel how these differ from a passenger train. The compliance of the above effects with current regulations will be presented.
- Explore the effects of train length, nose shape and loading configuration on the pressure transients using experiments and numerical simulations.

- Study the tunnel effect on the separation length around the train nose and show in detail the separation levels around the nose.
- Analyse the velocity magnitudes around, ahead and behind the train. Show how this differs from open air results.
- Use the results obtained from this study to investigate the effectiveness of 1D analytical models in predicting the maximum pressures inside the tunnel, caused by freight trains.

1.4 Research overview

The research undertaken consists of a) 3 physical experiments, b) 9 numerical simulations and c) 1D analytical modelling. A breakdown of the three items is given below referring to a visual representation of these cases in Figure 1.1.

The 3 physical experiments were performed using the Class 66 locomotive at 33.5m/s (see cases 1-3 in Figure 1.1). These experiments focused on the pressure transients measured at various locations inside and outside of the tunnel and examined the effect of train length and loading configuration. The findings of the experimental results from cases 1-3 led to the need of conducting CFD simulations.

A total of 10 CFD simulations were performed, as follows:

- 5 simulations with a train speed of 33.5m/s to analyse the pressure transients, flow separation and velocity field around the train (see cases 4-8 in Figure 1.1).

- 4 simulations with a train speed of 33.5m/s to validate the CFD model through mesh and timestep independence, as well as a comparison with another RANS model (see ‘Validation of CFD’ in Figure 1.1).
- 1 simulation with a train speed of 38.5m/s to confirm that the normalised results do not change with a speed increase of 5m/s and to investigate compliance with regulations at higher speeds.

The results from all methods were combined with 1D analysis, where theory from literature was implemented into a computer program to perform analytical calculations.

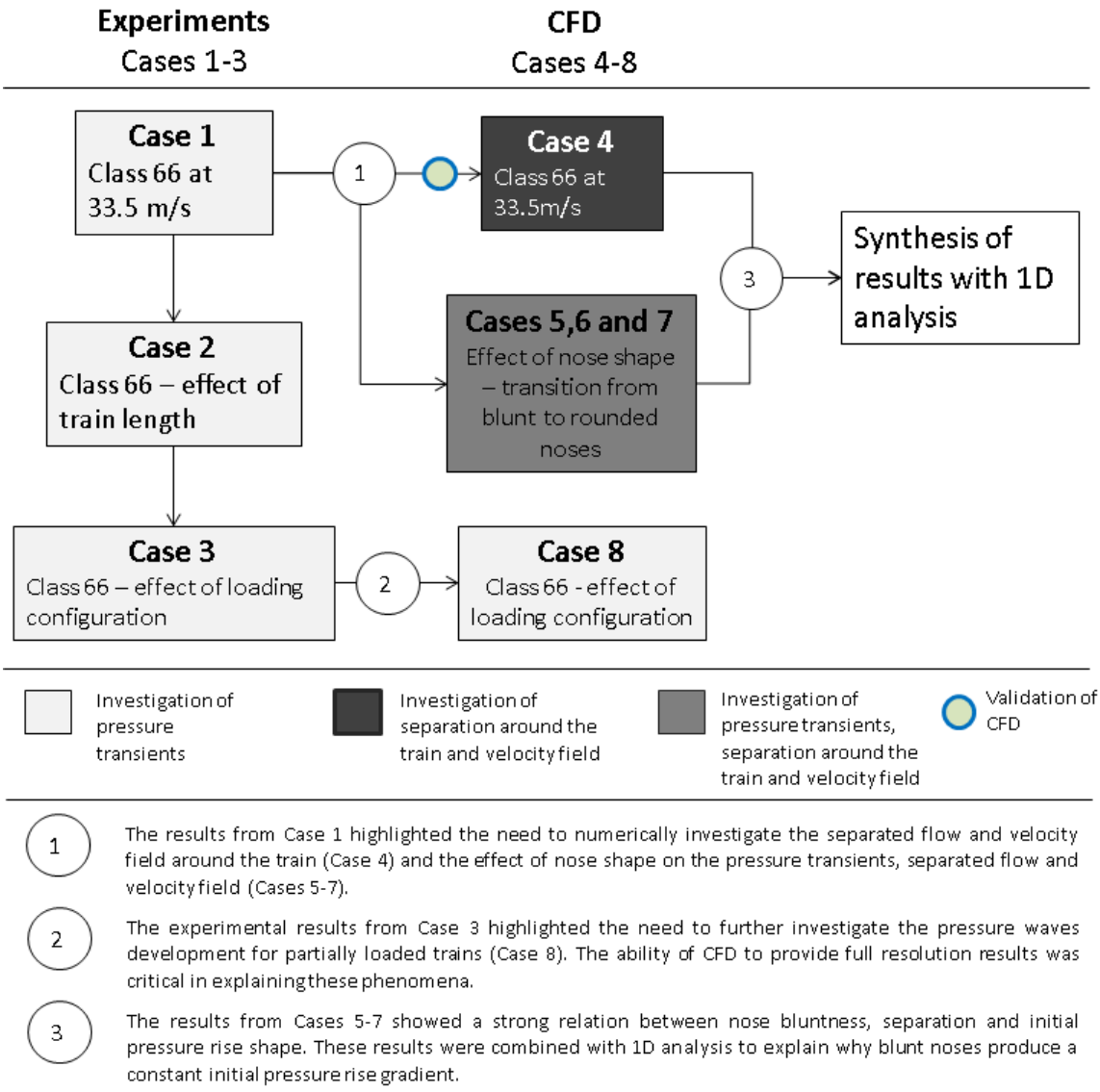

Figure 1.1: Overview of model-scale experiments, numerical simulations and 1D analysis

1.5 Thesis structure

Chapter 2 is the literature review which critically analyses the findings of previous researchers in the field of train aerodynamics. The chapter starts with bluff body and general train aerodynamics, and then narrows to tunnel aerodynamics. The importance of investigating freight trains is highlighted, as it is a relatively unexplored area of research, which is confirmed from the relatively small number of studies reported in this literature review. As expected, the main body of this chapter is an in-depth analysis of train aerodynamics in tunnels, explaining the flow phenomena required to understand the analysis of the current study and justify its significance. The literature gap is identified, defining the research aim of this novel study. To that end, an in-depth analysis of the train aerodynamics methodology is presented, playing a critical role in defining a suitable approach for obtaining trustable results.

Chapter 3 describes the experimental methodology for investigating the pressure transients inside the tunnel. The information presented in this chapter confirms that all model-scale experiments have been conducted according to the aerodynamic test requirements as defined in the European standards (CEN, 2003) and (CEN, 2010). This chapter provides all the details required for repeating a similar test in the future. Any characteristics related to the interpretation of results such as shape simplifications are discussed thoroughly.

Chapter 4 discusses the numerical methodology for investigating the pressure transients, flow separation and velocity field around the train. For all numerical simulations performed in this study, this chapter describes the computational

geometry and domain, sliding mesh technique and numerical model setup. Due to nature of the term modelling which includes a number assumptions and adaption of approaches for simulating a real flow, the numerical results are validated with experiments at various locations and for a number of flow properties.

Chapter 5 analyses and discusses the experimental results, showing the development and effects of pressure transients on the tunnel walls, entrance portal and train surface. Using a model-scale Class 66 locomotive, the variation of these effects with different train length and loading configuration is unpacked. All variables are clearly defined in the beginning of the section. The flow phenomena behind the presented results are explained and reference to literature findings is made when necessary. For most of the graphs, the location of the train in the tunnel at different instants is shown for better interpretation of results. Due to the nature of freight train shapes being blunt, comparison to passenger train results from other studies takes place to point out remarkable differences. For comparison purposes, the data is converted to its full-scale form. However, for the remainder of the results, the scaled form of the timebase is retained. For easier reference in the analysis, discussion and comparison of the results, all measurement points and areas are identified by unique numbers. The data obtained in this chapter act as a validation source for the numerical results in Chapter 6. The main recommendation drawn from this study is the need for further analysis on the effect of nose shape and loading configuration on the pressure transients, as well as the need to study the flow separation and velocity field around the train. This recommendation forms the research basis of the computational study in Chapter 6.

Chapter 6 presents the numerical results, analysing the pressure transients and flow field around the train. The results presented in this chapter were not possible to obtain through the model-scale experiments in Chapter 5, and consist of additional cases to the ones presented before. Starting with the pressure transients, the effect of nose shape and loading configuration are discussed in detail and the phenomena observed in the experiments are explored further. Then, the separated flow and velocity field around the train is explored, linked when required to the pressure transients findings. This chapter shows that the ability of CFD to provide full-resolution results plays a critical role in explaining the flow phenomena. At the same time, it suggests that the development of pressure waves is linked the separation levels around the train, highlighting the difference between the effective and geometric blockage area inside the tunnel. These findings lead to Chapter 7, which focuses on the relation between separation size and prediction of the pressure waves using analytical models.

Chapter 7 synthesises the results with 1D formulae to predict the initial pressure rise inside the tunnel. After selecting a suitable analytical model, the CFD results from Chapter 6 are used for the estimation of the required coefficients. Following implementation of the model, its suitability for freight trains is evaluated and discussed, suggesting modifications for its usage with blunt noses. These modifications are related to the difference between geometric and effective blockage ratio, which increases with nose bluntness.

Chapter 8 critically links and judges the findings from chapters 5-7, drawing conclusions and recommendations. The aim and objectives are discussed,

explaining how they have been addressed. The novelty of the study is clearly explained in this chapter, as well as the contribution to the current knowledge. This chapter closes with the research limitations and recommendations for further work.

Chapter 2

Literature review

A significant amount of sections 2.3.1 and 2.41-2.4.7 has been published elsewhere, see Iliadis et al. (2018, 2019). The author of this thesis is the first author of the published journal articles.

2.1 Aerodynamics of bluff bodies

A bluff body can be defined as a non-streamlined shape which satisfies one of the following criteria (Wolf, 2013):

1. The body size perpendicular to the flow is the same or larger to its size parallel to the flow direction.
2. There is a sudden change at the front part of the body which causes flow separation.

It is noted however by Wolf (2013) that in some cases bodies may behave as bluff bodies only under certain conditions. Typical heavy vehicles with bluff body behaviour are trains and trucks. When the body of interest is a freight train, criterion 2 is valid due to the blunt nose at the front.

The above geometry characteristics of bluff bodies are linked to certain flow phenomena such as flow separation and vortex shedding. The most commonly used bodies for investigating the above phenomena are circular, square and spherical cylinders studies (Bearman and Obasaju, 1982) (Sheard, Thomson and Hourigan, 2003) (Ozgoren, 2006). Such flow investigations can be used as benchmark to investigate the effect of a number of parameters and/or validate new methodologies.

The application of findings from bluff bodies research in vehicles and the influence of the ground in the flow field are thoroughly discussed in the review paper of Bearman (1980). The author suggests that most of the research in bluff bodies aerodynamics has been conducted in 2-D or axisymmetric shapes which focus on the above discussed shape configurations. These have limited relevance to bluff land vehicles because the drag generation on vehicles is not defined by the shedding of vortices. In addition, the majority of such studies do not take account the influence of the ground which is believed to be important (Bearman, 1980). When considering a cube, the most important effects of the ground when compared to axisymmetric flow (no ground) of a cylinder are believed to be:

- The stagnation point due to the incoming air at the front face moves downwards from the middle height of the vehicle towards the ground. This affects the lift force on the body due to different pressure distributions at the

top and bottom faces. Such an effect can be related to a freight train where the clearance between the vehicle and the ground is relatively insignificant.

- For cubes and circular cylinders, it has been observed that when reducing the clearance between the bottom face of the body and the ground, negative lift is generated (downforce) while drag is almost independent of the ground clearance (Bearman, 1980). According to Roshko (1993), one of the flow characteristics that define bluff bodies is high coefficients of drag, which is mainly composed of pressure drag.
- The vortex shedding behind a cylinder can be prevented if there is a wall close to its bottom side (Bosch, Kappler and Rodi, 1996).

Using a fixed ground instead of a moving belt can also be a source of error, as the upcoming boundary layer thickness cannot be controlled. This affects the incidence angle which plays a critical role in value of the lift coefficient (Bearman, 1980).

Using an automotive model, the study of Wang et al. (2019) has proved that the lift coefficient is sensitive to the ground movement, as the pressures in the underbody of the vehicle are affected.

Apart from the effects of the ground to the flow behaviour around bluff bodies, the shape of the nose has also been the focus of many researchers. For example, the study of Ota and Kon (1979) tested a number of blunt noses by changing angle α shown in Figure 2.1 below, where an angle of 180° represents a square front. It was found that the higher the angle α, the higher the separation length. The term separation length refers to the distance between the separation and reattachment

points (shown in Figure 2.1) and depends on a number of other parameters. For example, Schewe (2001) highlights that flow separation often depends on Reynolds number (separation length increases with increasing Re). Other parameters that affect the flow separation length are surface roughness and turbulent intensity (Derakhshandeh and Mahbud Alam, 2019).

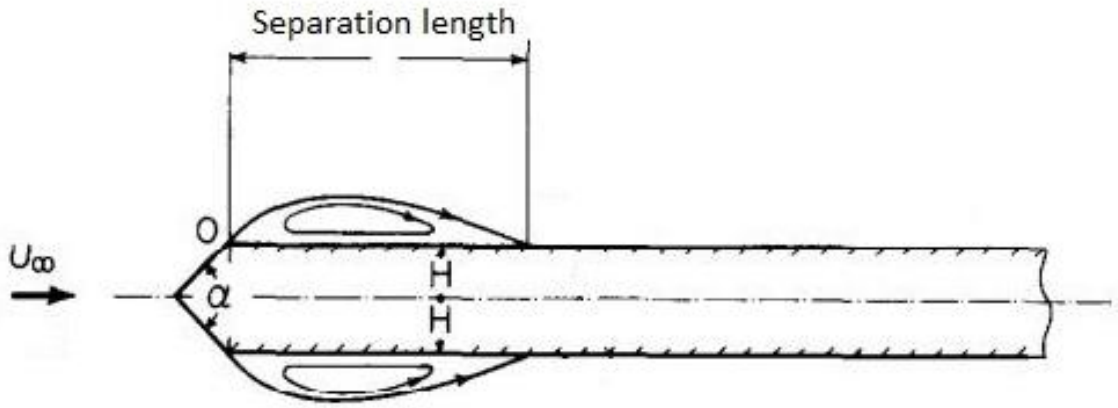

Figure 2.1: Angle α and separation length (Ota and Kon, 1979)

Relatively small angles α in Figure 2.1 can be linked to a streamlined passenger train, while larger angles approach the nose of a freight train. Thus, freight trains are expected to have longer separation compared to streamlined trains. It must be noted however that the aforementioned relationship between α and separation length has been derived from axisymmetric flow investigations (no ground).

2.2 General train aerodynamics

This section is an overview of train aerodynamics, starting from open air and narrowing to confined spaces and tunnel flows. Although the majority of research in train aerodynamics has been conducted on passenger trains, there is a small body of literature on freight trains, which has been included in this section.

2.2.1 Flow around the train (slipstream)

According to Baker et al. (2001), the flow around the train is divided into a number of key areas. These flow regions are discussed below:

- Nose of the train: measurements are made at a fixed distance from the centre of the track near the train side, aiming to measure the velocity and pressure field using a number of methods. The majority of trains create a positive peak for pressure and the normalized longitudinal component of velocity u_x at this region, which is followed by a negative peak. Hemida, Baker and Gao (2012) showed that some air particles in this region travel to the opposite direction of the train. According to Baker (2014 b), for most passenger trains, the normalized velocity at approximately 3m from the centre of the track (full scale) is between 0.05-0.1 but higher for freight trains due to their blunt nose shape. This is verified by the study of Soper (2014) which focused on the slipstream around a Class 66 freight connected to container wagons (the same model used for the current study) and u_x was approximately 1.2. Figure 2.2 shows

that the nose peak has the most intense velocity gradient compared to the rest of flow regions.

- Boundary layer region: at the roof and sides, the boundary layer is relatively thick, large scale (equivalent to the width and height of the train) and three dimensional (Baker, 2014 b). It has been found that its thickness varies along the length of the train (Sterling et al., 2008). This can be confirmed from Figure 2.2.
- Near wake: the form of flow in this area depends on the shape of the train at the tail. Blunt ended trains produce a vortex which travels towards all three directions (longitudinal, vertical and lateral) while for streamlined trains a pair of vortices travelling towards the longitudinal direction have been observed (Baker, 2010). The study of Bell et al. (2014) showed the presence of a near wake velocity peak, which has the highest magnitude among all other velocities around the train. Apart from velocity, Baker (2014 b) showed that the pressure peak observed for HST is the reverse pressure peak occurring at the nose, but at less intense magnitude.
- Far wake: in this region behind the train, velocities are expected to reduce as the distance from the tail increases (evident from Figure 2.2). In general, there is no significant research interest in this region.
- Underbody flow: research for this region usually focuses on ballast flight using pressure and velocity measurements. Along the train length, the most intense changes or peaks are observed at the nose and tail of the train with relatively constant values between these them (Quinn et al., 2010).

- Flow over the roof of the train: measurements over the roof usually aim in predicting the boundary layer thickness and pressure/velocity distribution along its length. This area is characterized by Baker (2014 b) as a topic which needs further investigation due to the lack of research data available.

Therefore, it can be clearly observed from the above that the closer to the train nose, the more significant and intense the flow phenomena (in terms of the velocity gradient). The effects of nose bluntness are remarkable while the roof of the train is noted as an area with promising research potential.

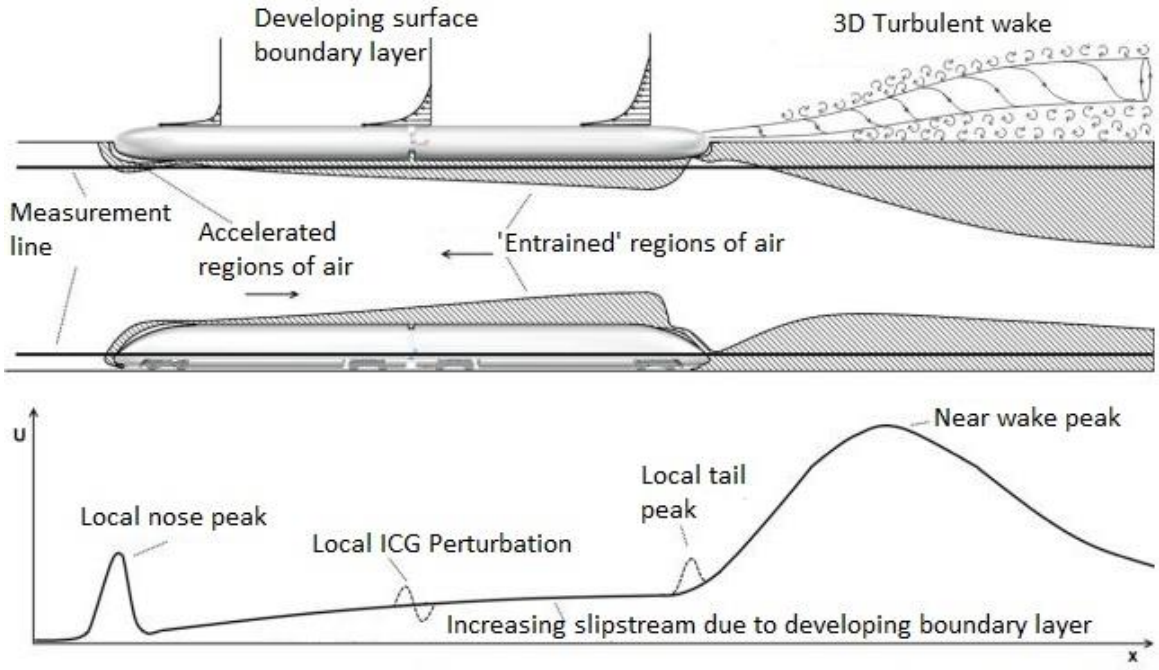

Figure 2.2: Flow regions and velocity distribution around a high speed train (Bell et al., 2014)

2.2.2 **Flow constraints and tunnels**

The term ‘flow constraints’ describes various trackside structures such as bridges, hoardings, station canopies or walls. Investigations can focus on both the loading on these structures but also on the forces experienced by the train. For example, the study of Baker et al. (2014) measured pressure forces on the surface of these flow constraints. A positive peak followed by a negative one was found in all cases, as observed for slipstream measurements in section 2.2.1. Figure 2.3 confirms the presence of these nose peaks which then appear in the reverse order at the tail. Their magnitude is significantly affected by the train shape, with the highest values observed for freight trains. In a review paper, Baker (2014 b) suggests that these peaks are higher compared to open air measurements (no flow constraints) performed at equivalent distances from the train.

Other studies, such as the investigation of Johnson and Dalley (2002) conducted measurements on the surface of a stationary train passed by a moving train. It was shown that pressure loadings decrease with increasing the gap between the trains. This can be related to a stationary structure and a moving train where similar effects are expected.

Tunnels differ from the above structures as they enclose the train from all sides, showing a distinctive characteristic in the nature of the flow (Baker, 2014 b); and the generation of pressure waves which reflect at each end of the tunnel. The pressure waves are related to a number of important effects:

- High amplitude and steep gradient waves which can influence the stability of the train and cause fatigue problems. For passenger trains, this can cause passenger discomfort, introducing the needs for well-sealed trains (CEN, 2003).
- Emission of environmentally harmful micro-pressure waves, which are pulses of pressure emitted to the environment from the tunnel ends (Baron, Molteni and Vigevano, 2006).
- Additional drag because of the tunnel walls which can affect the efficiency of the train (Baker, 2014 a).
- Affected velocity field at the sides of the train which can potentially displace trackside objects inside the tunnel and be uncomfortable for tunnel workers (CEN, 2003).

The above effects have made it necessary for researchers to focus on the topic, aiming to improve the safety and efficiency of trains in tunnels. These flow phenomena are discussed in detailed in the remainder chapter, focusing on the most relevant parts to this study.

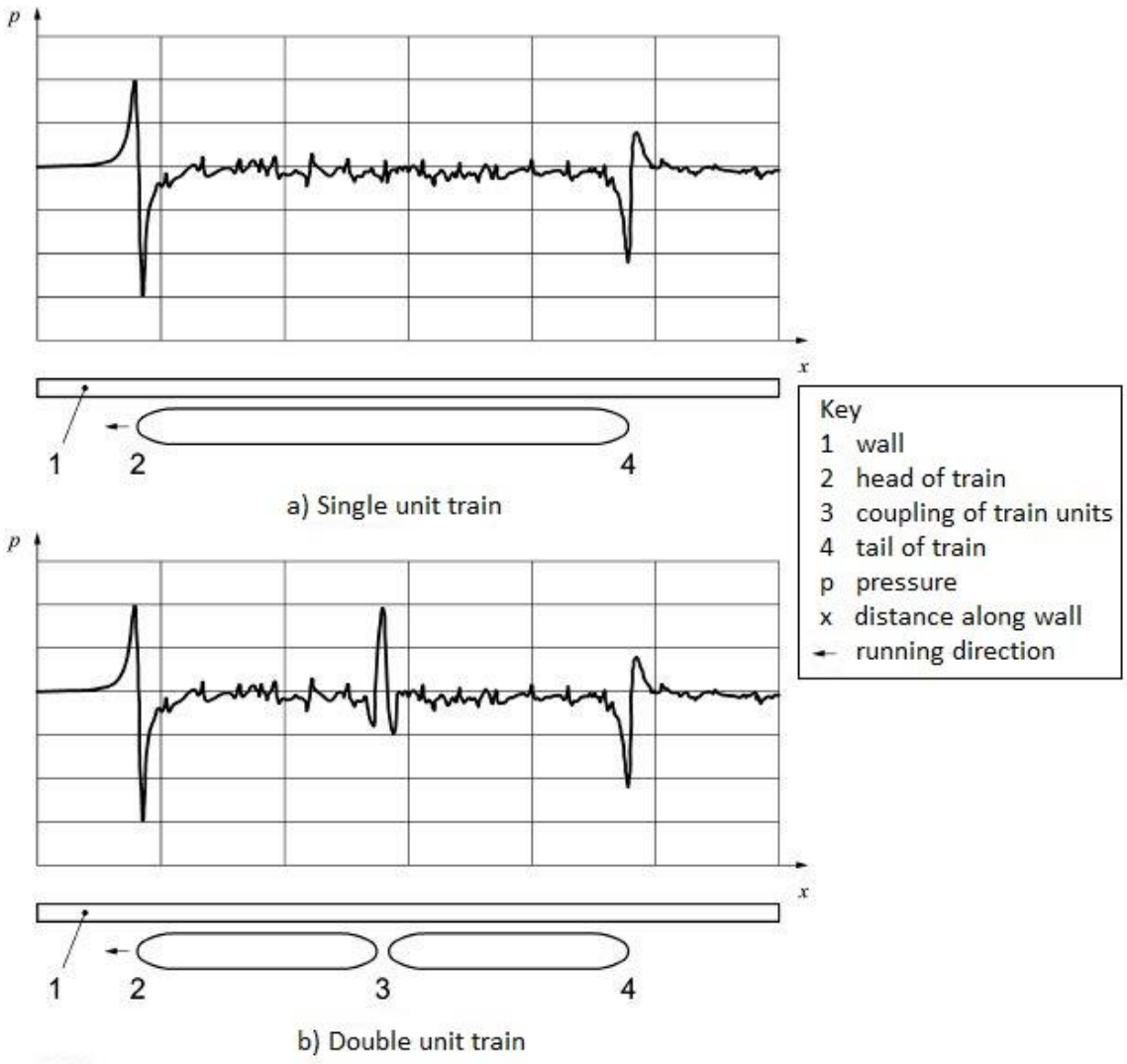

Figure 2.3: Instantaneous pressures on a vertical wall caused when a train passes by. An additional pressure peak is observed on b) because of the gap between the two units (CEN, 2013)

2.3 **Freight train aerodynamics**

The rough shape of freight trains has been used in a number of studies and was found to be less aerodynamic efficient than passenger trains.

‘’In open air, the flow around the train, known as the slipstream, has been shown to produce higher slipstream magnitudes for freight trains when compared to passenger trains, primarily due to the bluff nature of the train shape’’ (Iliadis et al., 2019, p. 1). For example, Rigby (1993) showed that at a distance of 2 meters from the platform, the maximum normalized velocities are 0.15-0.17, 0.2 and 0.38 for streamlined passenger trains, passenger trains with bluff end and fully loaded freight trains respectively. Similarly, in the study of Baker et al. (2014), the surface pressure coefficients on the hoardings were higher for the Class 66 freight train compared to Class 158 and Class 390, which are non-streamlined and streamlined passenger trains respectively (see Figure 2.4 below).

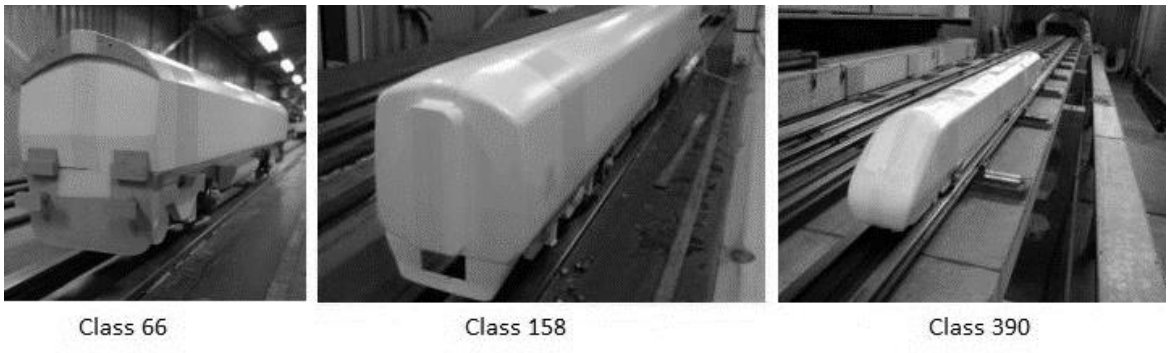

Figure 2.4: Scale test models; Left: Freight train; Middle: Non-streamlined passenger train; Right: Streamlined passenger train (Baker et al., 2014)

In terms of skin friction, full scale measurements have shown that the estimated skin friction coefficient for a freight train with irregular wagons was as high as 0.01, which was 300% higher than a streamlined passenger train (Vardy and Reinke, 1999).

2.3.1 Separated flow around the train head

The flow at the head of a freight train can be related to a bluff body where it separates at the front part, forming a vortex, which is followed by a stagnant air region. Then, the flow curves back to the surface forming a reverse flow region (Curie, 2012). The generation of turbulence occurs mainly in the reverse flow region (Singh and Sarkar, 2011). The above phenomenon is called the separation bubble and can be either pressure or geometry induced. In general, flow separation causes energy losses (dissipated as heat) and deviation of streamlines (Chang, 1961). Similarly, it is believed to have a significant effect on the slipstream velocity magnitudes at the sides of freight trains(Soper, 2014). High velocity magnitudes can create slipstream forces, which are capable of interacting with trackside objects. To quantify the size of the separation bubble, several studies have investigated the length and height of the bubble (Jahanmiri, 2011,Diwan and Ramesh, 2007,Kim and Moin, 1985,Kiya and Sasaki, 1983,Arakeri and Acosta, 1973). The length of the bubble is the distance between the point of separation and point of reattachment and its height is the distance between the surface and the point where the velocity is equal to the freestream velocity. The mean bubble length and height decrease with increasing Re

(attributed to outer flow layers activity) (Samson, Sarkar and Anand, 2012) and surface roughness (Bokhortst et al., 2015).

2.4 Trains in tunnels

2.4.1 Aerodynamic efficiency - Drag

When a train enters a tunnel, additional drag is present (Novak, 2006), as a repeated pattern of reflective pressure waves is formed. The drag inside the tunnel is divided into skin friction and pressure drag. Skin friction drag increases with higher blockage ratio, train length and surface roughness (Vardy, 1996b) while the pressure waves inside the tunnel generate drag as they contain energy. The additional drag inside the tunnel is translated to a tunnel friction factor (CEN, 2010) which can be related to the drag coefficient in open air (Baker, 2014 a). As a result, the additional amount of drag reduces the aerodynamic efficiency.

One of the main causes of drag inside the tunnel is pressure stagnation losses believed to occur at the nose of the train (Vardy, 1996b). Consequently, these effects have driven many researchers to study the optimum nose shape for passenger trains aiming to reduce the strength of the initial compression wave which has the highest pressure amplitude (Kikuchi, Lida and Fukuda, 2011). However, due to the blunt nature of many freight train noses, combined with the need for higher train speeds, it is believed that the flow around freight trains is an increasingly important area of research.

The generation of pressure drag is believed to be linked to flow separation (Bushnell and Moore, 1991,Chang, 1961). However, aerodynamic drag is believed to have a remarkable impact on performance only in long tunnels.(Vardy, 1996a) In short tunnels (<1km), the generation of drag is mostly associated with passenger comfort, which is not applicable to freight trains.

2.4.2 **Pressure waves**

Reduced aerodynamic efficiency is not the only consequence of the pressure waves formation. The intense aerodynamic forces produced from these waves can cause structural and stability problems on the train and track.

The pressure waves take the form of a complex pattern of compressive and expansive waves (see Figure 2.5). The nose of the train pushes the air ahead of it, and generates a compression wave (Bellenoue, Moriniere and Kageyama, 2002). This is marked as point 1 in Figure 2.5, where the compression wave meets the measurement point. At the tunnel walls, the pressure increase is composed by a two-part pressure gradient. The high pressure of this planar wave occurs due to the fact that the air molecules are closer to each other (compression wave). The wave travels with the speed of sound, and then reflects back as an expansive pressure wave similarly to the open-end piston effect (Howe, 2014). Then it follows a repeated pattern of reflective waves which change sign during reflection. In addition to the above pattern triggered by the nose entry, when the tail enters the tunnel an expansion wave is generated, which reflects back as a compression wave. Point 2 on

the same figure, represents the expansion wave passing by the measurement location. Similarly, pressure changes at points 3-5 occur because of the reflected waves of the two above patterns. For stationary measurements inside the tunnel, pressure increases and decreases when the train head and tail pass by, respectively (see points 7 and 8). According to the CEN (2003), a third and fourth pattern of pressure waves form when the head and tail exit the tunnel. However, these seem to have minor or negligible effect on pressure (see point 6).

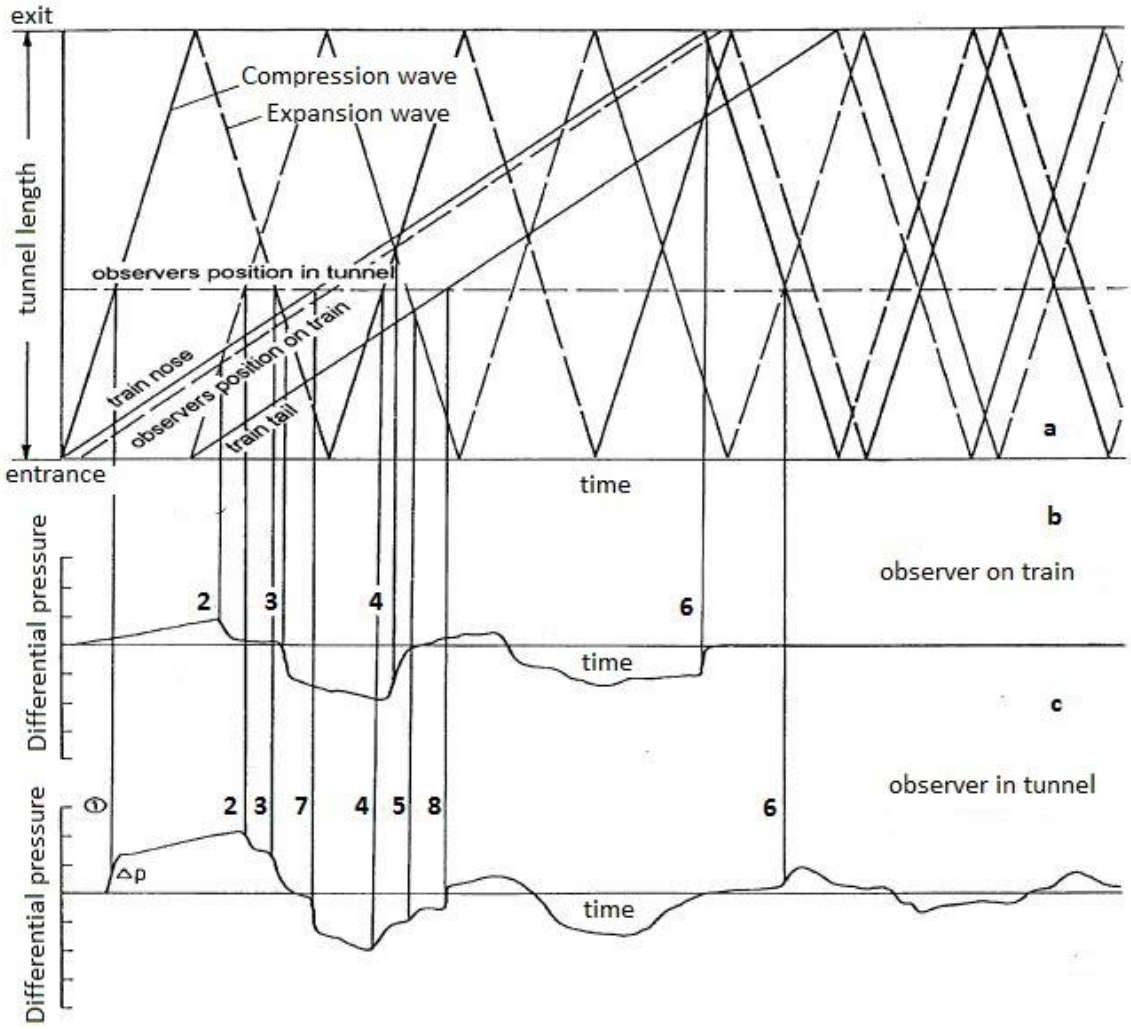

Figure 2.5: Top: Location of pressure waves and train head and tail in relation to the tunnel length; Middle: Pressure history recorded at the train surface; Bottom: Pressure history recorded inside the tunnel. The location of the measurement point is shown at the top graph (dotted line), adapted from (CEN, 2003)

Among all waves in the tunnel, the initial compression wave during nose entry produces the highest magnitude of pressure increase and the most intense pressure gradient. As a result, several researchers have focused on the development of the initial compression wave using 1-D analytical theory (Howe, 1998a). Such studies

highlight the effects of the train nose, encouraging the investigation of a freight train, since the nose coefficient for freight trains is significantly higher compared to passenger trains. In an effort to find the optimal shape, a number of studies have investigated the topic (Choi and Kim, 2014) (Maeda et al., 1993) (see Figure 2.6).

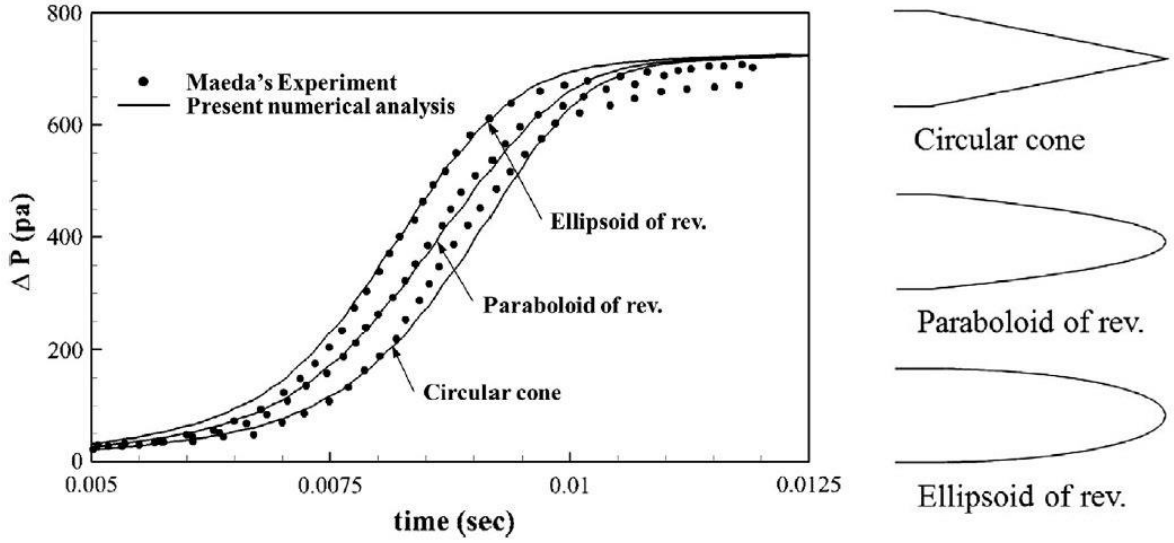

Figure 2.6: Effect of three nose shapes on the initial compression wave. Comparison of the numerical study of Choi and Kim (Choi and Kim, 2014) to the experiments of Maeda et al. (1993)

Apart from the nose shape, Howe (1998b) showed the train speed plays a critical role on the amplitude and gradient of the initial compression wave. The higher the speed, the higher the amplitude and gradient of the initial compression wave (Figure 2.7). Other parameters which influence the initial pressure gradient are the blockage ratio and the shape of the tunnel portal.

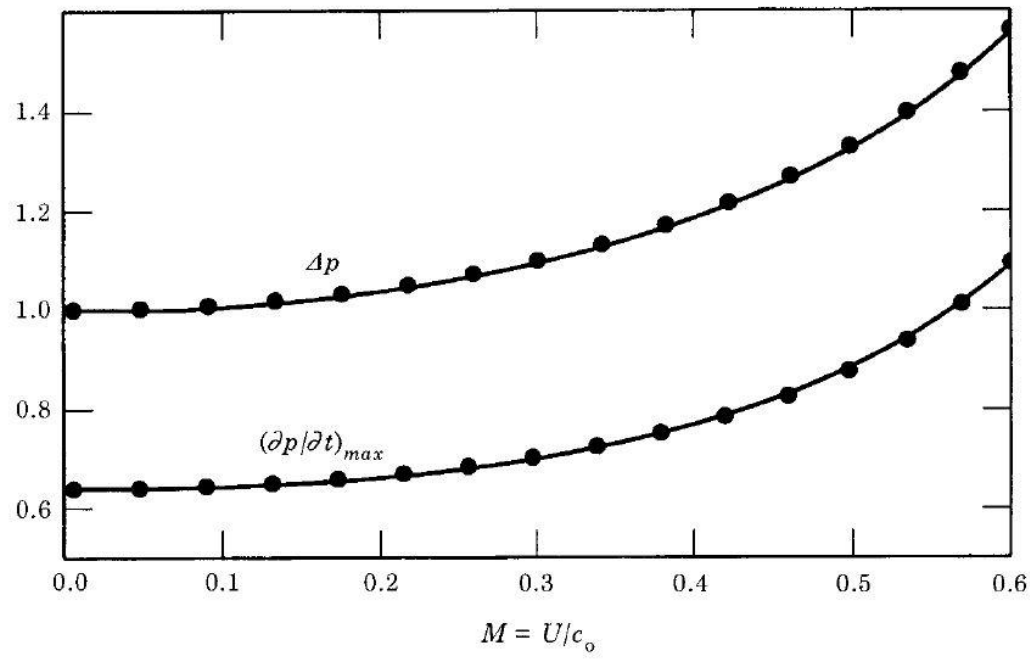

Figure 2.7: Mach number dependence of the amplitude and gradient of the initial compression wave during nose entry (Howe, 1998b)

The effects mentioned above, make it essential to investigate in detail the nature of the generated pressure waves and their interaction with the 'blunt' nose and the rough discontinuous sides of a freight train.

2.4.3 **Environmental effects – Micro-pressure waves**

During the reflection, a small part of the pressure wave is radiated to the environment as a micro-pressure wave. The micro-pressure waves are pulses of pressure emitted to the environment which, at high train speeds, can generate a noise of up to 140-150 dB, becoming environmentally harmful (Shin and Park, 2003).

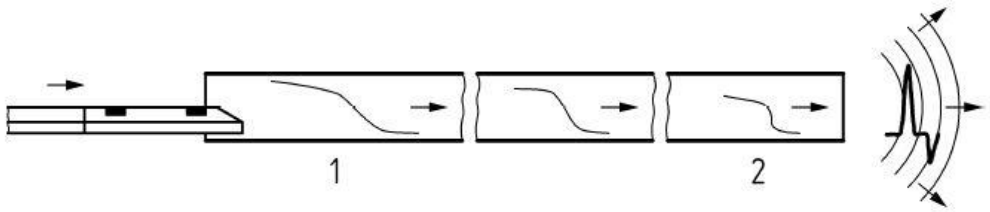

Key

1 tunnel entrance portal

2 tunnel exit portal

Figure 2.8: Pressure wave generation, propagation and radiation (CEN, 2010)

They are caused by nonlinear steepening and their amplitude depends on the gradient of the initial compression wave (Howe et al., 2000,Shin and Park, 2003). There is a strong variation of the magnitude of the micro-pressure waves with train speed. Noise emissions are a particular problem with high speed trains in excess of 250 km/h (Maeda, 1999). The extent to which the micro-pressure waves are emitted to the environment directly influence the attenuation of the pressure waves inside the tunnel (because some energy is lost to the environment), and therefore they should not be ignored.

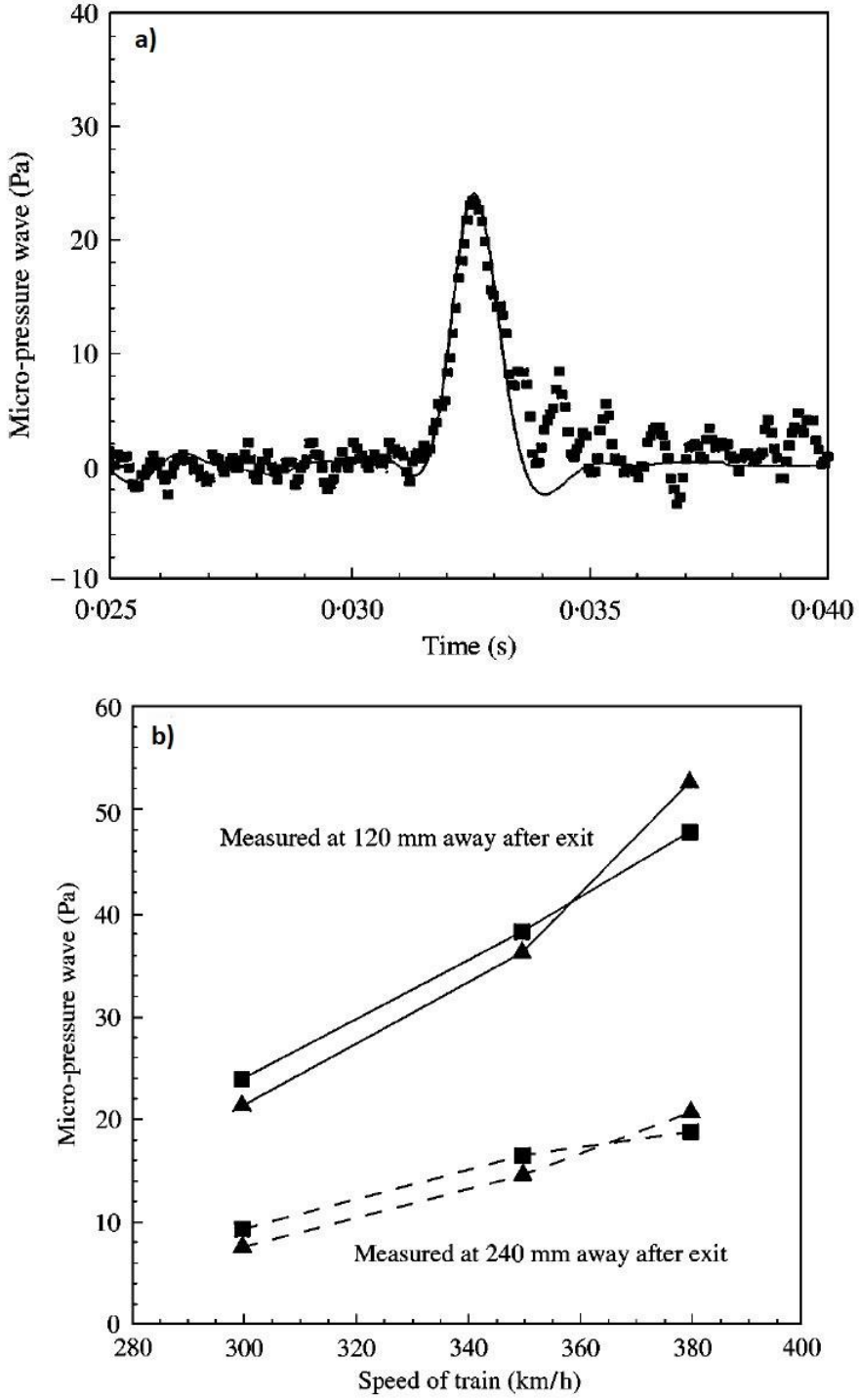

Figure 2.9: Micro-pressure wave ; a)300km/hr; b) Variation of micropressure wave intentsity with speed, at a fixed distance from the exit portal (Yoon et al., 2001)

2.4.4 **Reflection of pressure waves inside the tunnel**

The propagation of a wave depends on the acoustic impedance (or flow impedance) (Mechel, 2008) which is defined as the ratio of sound pressure to volumetric flow rate. ‘’The acoustic impedance Z is the property of a particular geometry and medium: we can discuss for example the Z of a particular duct filled with air’’ (UNSW, 2010). This is different from specific acoustic impedance which only specifies the impedance of a medium (i.e. air or water). Acoustic impedance is:

$$Z = \frac{p}{Q} \tag{1}$$

Where the volumetric flow rate is the volume of fluid passing per unit time:

$$Q = \frac{dv}{dt} \tag{2}$$

In the case of a tunnel, when the wave travels a distance $dy = \mathrm{a} \times dt$, the air volume is $A \times dy$. Substitution into (2) gives:

$$Q = A\frac{dy}{dt} = A\mathrm{a} \tag{3}$$

Therefore, the acoustic impedance for a pipe/tunnel becomes

$$Z = \frac{p}{A\mathrm{a}} \tag{4}$$

Eq. (4) shows the direct dependence of impedance to the cross-section area. When the wave reaches the exit of the tunnel, the sudden increase in cross section area reduces the value of acoustic impedance. The impedance mismatch at the boundary of the tunnel exit causes the reflection of the pressure wave. Impedance drops to a

lower value and therefore changes the sign of the pressure wave (a compressive wave turns into an expansive wave and vice versa). In cases where the impedance of the new medium is higher (moving into a smaller cross-sectional area) the reflected wave keeps its sign.

2.4.5 **TSI Requirements**

The Technical Specifications of Interoperability (TSI) define the requirements that railway systems need to meet to ensure interoperability in Europe (TSI, 2014). The maximum pressure changes occurring in the tunnel have been specified in terms of the initial compression wave which is divided into two parts; the steep gradient increase Δp_N caused when the nose enters the tunnel and the second pressure increase Δp_{fr} due to friction effects when the main part of the train enters the tunnel (CEN, 2010). The above pressure changes are shown in Figure 2.10 which includes two additional pressure changes Δp_T and Δp_{HP} , caused by the tail entry and the train head passing by the measurement point respectively. These requirements refer to tube-like tunnels of constant cross section area (no airshafts or other air release mechanisms), applicable to single trains passing through a tunnel. Meeting the requirements of Table 2.1 below is important for maintaining safety in the operation of railway systems.

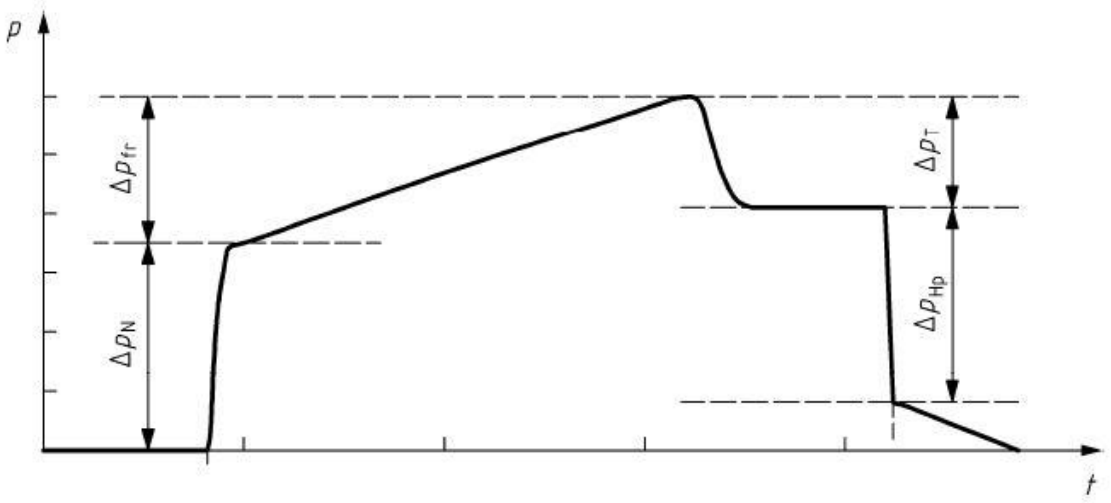

Figure 2.10: Initial compression wave recorded at a fixed position in a tunnel. The pressure changes are split into 4 parts (CEN, 2010)

Table 2.1: TSI Requirements (TSI, 2014)

Train type	**Reference case**		**Criteria for the reference case**	
	V [m/s]	A [m^2]	Δp_N [Pa]	$\Delta p_N + \Delta p_{fr}$ [Pa]
$V_{tr,max}$ ≤69.4 m/s	55.5	53.6	≤1750	≤3000
$V_{tr,max}$ ≥69.4m/s	69.4	63	≤1600	≤3000

2.4.6 **Similarity criteria**

The use of a reduced scaled model arises from the complexity and cost of full-scale experiments in tunnels. According to CEN train experiments can be conducted with a minimum of 1/25 scale, for minimizing Reynolds number effects (CEN, 2010), while

the full-scale train speed must be respected for Mach ≤ 0.3, although the characteristic length changes (CEN, 2010). Similarly, the open track railway aerodynamics requirements state that a minimum Re = 250,000 should be used to represent full scale tests (CEN, 2013). Reynolds number and Mach number are the similarity parameters for viscosity and compressibility respectively. Reynolds number is the ratio of inertial to viscous forces. Using a Reynolds number which is close to the full-scale tests can capture the effects of viscous forces correctly.

Previous studies have confirmed the validity of this minimum size for the flow field around passenger trains (Baker, 2010) and for trains in tunnels through comparison to full-scale data. Johnson and Dalley (2002) have conducted 1/25th scaled experiments for a passenger train passing through a tunnel at the TRAIN RIG, and the comparison of pressures inside the tunnel with full scale results showed excellent agreement. The results of their study can be seen in Figure 2.11 which shows the pressure histories at the tunnel wall, when the ETR500 train passes through the tunnel. The full scale 9 coach train and the 4 coach scaled model travel at speeds of 50m/s and 51.38m/s respectively. Therefore, the slightly larger values for the scaled model are justified by the higher speed.

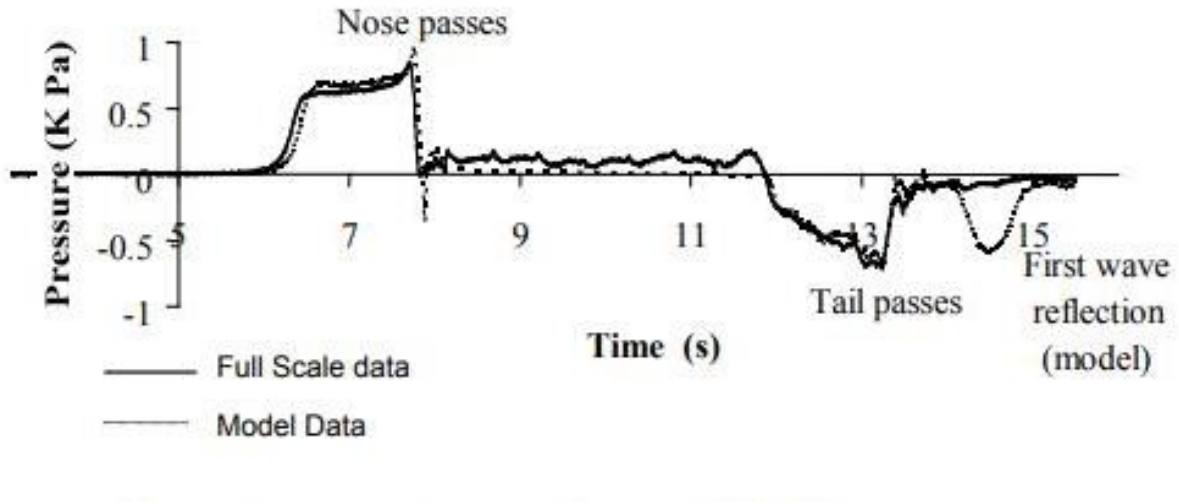

Figure 2.11: Pressure histories comparison for full scale and scaled model [Johnson and Dalley 2002]

Similar experiments to the current study have been successfully performed recently by Zhang et al. (2017) using a scaled moving model. The pressure amplitudes do not change in full scale, but the pressure traces in the scaled tunnel occur 25 times faster than in full scale. The Re number of this test is 384,000 and its calculation is based on the height of the scaled model. When conducting scaled tests on trains in tunnels with Re>360,000, the similarity criterion is satisfied (Zhang et al., 2017,Auvity and Kageyama, 1996). Apart from the prediction of the pressure waves, the Reynolds number effects on the separated flow around the train is of significant interest. When investigating the flow around the train in open air (slipstream) using the current scaled model in the TRAIN Rig facility, the boundary layer growth and velocity/pressure magnitudes are comparable in full and model-scale (Soper, 2014). However, the same study suggests that different Reynolds number influences at which scales

dissipation occur, and the finer small turbulent scales are different. Therefore, the results can only be used to offer an insight into key flow characteristics.

2.4.7 **Overview of techniques in Train aerodynamics**

The above phenomena can be predicted using a variety of techniques. Current methods in train aerodynamics include analytical models, physical experiments (at both full and model-scale) and numerical simulations (Baker, 2014 b). The use of analytical models can prove difficult when choosing coefficients, which depend on the train/tunnel system as a whole (Sajben, 1970) and detailed information about the flow separation cannot be obtained. Results from full-scale experiments are accurate (if performed correctly) but complex to conduct. Model-scale physical experiments reduce complexity and offer cost efficiency compared to full scale testing, usually using moving models for simulating the relative motion between the tunnel/ground to the motion of the train (Soper, Baker and Sterling, 2015,Zhang et al., 2017). Figure 2.12 below shows two moving model facilities, which consist of firing, testing and braking zones.

Figure 2.12: a) TRAIN Rig facility of the University of Birmingham, UK (Soper, 2014) b) Key Laboratory of Traffic Safety, Central South University, China (Zhang et al., 2017)

The main advantage of moving models over stationary models in wind tunnels is the ability to predict the flow phenomena associated with the interaction between the ground and the vehicle (Baker, 2014 b). The use of Computational Fluid Dynamics (CFD) has the advantage of full resolution results for obtaining detailed information (i.e. for the separated flow over the train). Although validation with experiments is required in most cases, CFD plays a key role in train aerodynamics and it is widely used to analyse the effect of crosswind on trains (Flynn, Hemida and Baker, 2016), slipstream around the train (Flynn et al., 2014) and tunnel effects (Khayrullina et al., 2015). For the latter case, using moving zones to simulate the relative motion can give validated results. For example, the study of Huang, Hong and Kim obtained experimentally validated results using RANS for investigating the unsteady flow inside the tunnel (Huang, Hong and Kim, 2012). When comparing different RANS models, k-ω has been found to be best choice for predicting the reattachment length and mean velocity profile, providing very good agreement with DNS (Araujo and Rezende,

2017). Other approaches include the use of LES (at the expense of higher computational cost), for which the results of Khayrullina et. al. (2015) and Hemida and Krajnovic (2010) indicated the required level of agreement with experiments.

2.4.8 **1D formulae**

Using 1D analytical models is a cost and time efficient method to predict the pressure transients inside the tunnel. The formulae are expressed in the form of algebraic equations and can be solved analytically without the need for a numerical scheme. They can predict the initial pressure rise, attributed to the nose and main body entry into the tunnel, as well as the tail entrance pressure changes. However, the amount of results from this approach is limited to pressure changes inside the tunnel. At the same time, this approach requires a significant amount of input values, accompanied with a number of uncertainties and difficulties:

a. Knowing important geometric and flow parameters such as the nose and tail coefficients (either in open air or inside the tunnel) are prerequisites to use 1D analytical formulae (CEN, 2010). Depending on the selected formula/approach, other parameters such as the tunnel and friction coefficients are required. This limits their use as standalone tools.
b. Knowing the train and tunnel cross sectional areas with adequate accuracy can be challenging (Vardy, 1996b). These values are used for the calculation of blockage ratio which plays an important role in the final pressure calculations.

c. The models do not take into account detailed geometric features between the nose and the tail of the train (i.e. gaps).
d. Generally programs with 1D formulae do not account for 3D effects around the train ends (nose and tail), in order to maintain low CPU usage. However, it is possible to introduce specific terms to treat these phenomena (William-Louis and Tournier, 2005).

Despite the above challenges, when used correctly, 1D formulae can achieve very good agreement with experiments (Mei, 2013). Part 5 of the European Standards (CEN, 2010) gives a list of different approaches that can be used, along with a description of them. It must be mentioned that all methods contain the nose coefficient term. This can be computed using theory derived from Bernoulli equations and conversation of energy (Vardy, 1996a).

Selection of the most suitable formulas can be based on which input coefficients are available, as these differ between models. Coefficients can be obtained through experiments or numerical simulations, and even from during routine operation of trains (Vardy and Reinke, 1999). For the current study, the formulae from Vardy (2008) have been selected and implemented. Forming a supplementary part of this research, these formulae were combined with the results of this study to assess their suitability for freight trains and to provide additional information. A complete analysis and implementation of these formulas is presented in Chapter 7 of this thesis.

2.4.9 **CEN**

Part 3 of the European Standards for aerodynamics in tunnels define the basic flow phenomena for single trains and crossing trains in a tunnel (CEN, 2003). The most relevant points to the current study are presented below:

- Drag: According to CEN, the most important factor influencing the additional drag is the blockage ratio of the train to the tunnel cross sectional area. Other important parameters include the train shape and length, while the train speed and tunnel length need to be considered for short tunnels only. According to CEN, short tunnels have a length shorter than 2km.
- Analytical formulas: An introduction to a basic 1D formula for calculating the pressure change during the generation of the initial compression wave is made. Detailed description of additional models is presented in Part 5 of the same standards.
- Aerodynamic forces around the train: For the flow field at a fixed point between the train and the tunnel walls, the highest forces are expected by the passing of the tail and the wake behind it.

Part 5 of the European Standards provides the guidelines and requirements of conducting measurements, including scale moving models similar to the current studies (CEN, 2010). The requirements below need to be met:

- The shape of the tunnel needs to have a constant cross section and no airshafts should be used.

- No initial flow should be present in the tunnel. i.e. pressure waves from a previous train.
- The train speed accuracy needs to be known with maximum 1% deviation and needs to be constant during entry at 1% of the train speed.
- The scale of the train shall be 1/25th or larger to ensure minimum Re effects. When converting the results to full scale, the pressure amplitudes remain the same but the time-base must be multiplied by 25, if a 1/25th model is used.
- The pressure transducers need to be calibrated before use, allowing for a maximum measurement error of 1%.
- When leading and end cars are used, a minimum of two intermediate wagons shall be used.

2.5 Conclusions for literature review

The literature review presented in this chapter showed that the majority of research in the past has focused on passenger trains. The prospect of increasing the speed of freight trains introduces the need to investigate their aerodynamics in tunnels, as it has only previously been done for higher speed passenger trains. The unique characteristic of freight trains is their rough and blunt shape. Previous research has shown that this can influence a number of effects, with the most significant listed

below. It must be mentioned that when investigating the effects below, compliance with European Standards must be ensured.

a. The amplitude and gradient of the pressure waves inside the tunnel: High amplitudes of pressure waves can be linked to structural and stability problems on the train and track.
b. The separated flow around the train inside the tunnel: High velocity peaks and long separations around the train are unwanted for safety, comfort and efficiency.

The literature review showed that no study has investigated in detail the above phenomena for freight trains in the past, making this study necessary.

The pressure transients' analysis in this study focuses on addressing effect a. above, while the flow separation and velocity field investigation around the train provides an in-depth analysis on effect b.

Chapter 3

Experimental methodology

3.1 Introduction

This chapter describes the methodology of the model-scale experiments (cases 1-3 in Figure 1.1) performed to explore the pressure field at the tunnel walls, entrance portal and locomotive surface.

3.2 TRAIN Rig and model

The experiments used a 1/25th scale moving model at the TRAIN Rig facility. The facility has been used for numerous aerodynamic tests, including tunnel flows, slipstream flow development, crosswind effect, ballast projection and platooning vehicles. Speeds up to approximately 75m/s can be achieved (depending on model weight), ensuring the safe firing of the model. It can be used both for trains and road

vehicles. The length of the facility is 155m and the track makes up 150m of the total length. It is divided into three 50m long sections where testing occurs, as discussed below:

1. The first 50 meters are used for firing the model using a mechanical propulsion system. The system uses a pre-tensioned elastic system attached to the bottom of the train, causing rapid acceleration. The required speed is obtained by the level of tension in the system, which is controlled and measured by the operators located in a safe control room separated from the test track. The higher the tension, the higher the train speed. With increasing the tension level, the model is pulled further back near the starting point of the testing track. However, it must be mentioned that the levels of tension depend on the model weight which varies with model loading configuration and length. As the current sets of experiments consisted of different loading configuration and train lengths, a number of trial runs were needed in order to establish the target tension load, for obtaining the required model speed.
2. The second section of the test track is where measurements take place. The tunnel, light gates, and photoelectron sensors are all located in this section of the facility. What differentiates it from the section 1 and 3 is the fact that the speed of the model is almost steady in this area. There is a minor reduction in the speed due to the track friction but also due to drag on the surface of the model. During testing, the speed reduction between the tunnel entrance and exit was found to be less than 0.5% of the train's speed at entry. This is line

with current codes of practice which require the speed to be constant with a maximum deflection of 1% (CEN, 2010).

3. The third 50 meters section is where the train is brought to rest using a piston braking system. The train is equipped with a custom design hook for catching the elastic rope located at the centre of the track and connected to the braking system. The hook pulls the piston deformable system and activates the brake. For safety reasons, a second brake exists in case that the hook and the elastic rope do not come in contact because of misalignment. For extra safety, the end of this section is filled with foam to prevent model damage, in case that neither of the brakes is enabled. However, during the current experiments, neither the second brake nor the additional safety measures were used, as the first brake functioned as required.

All tests are operated from the control room which has visual contact with the track and controls the firing of the model. A schematic of the accelerating (Section 1) and the braking section (Section 3) is presented in Figure 3.1 below, showing the details of the mechanism.

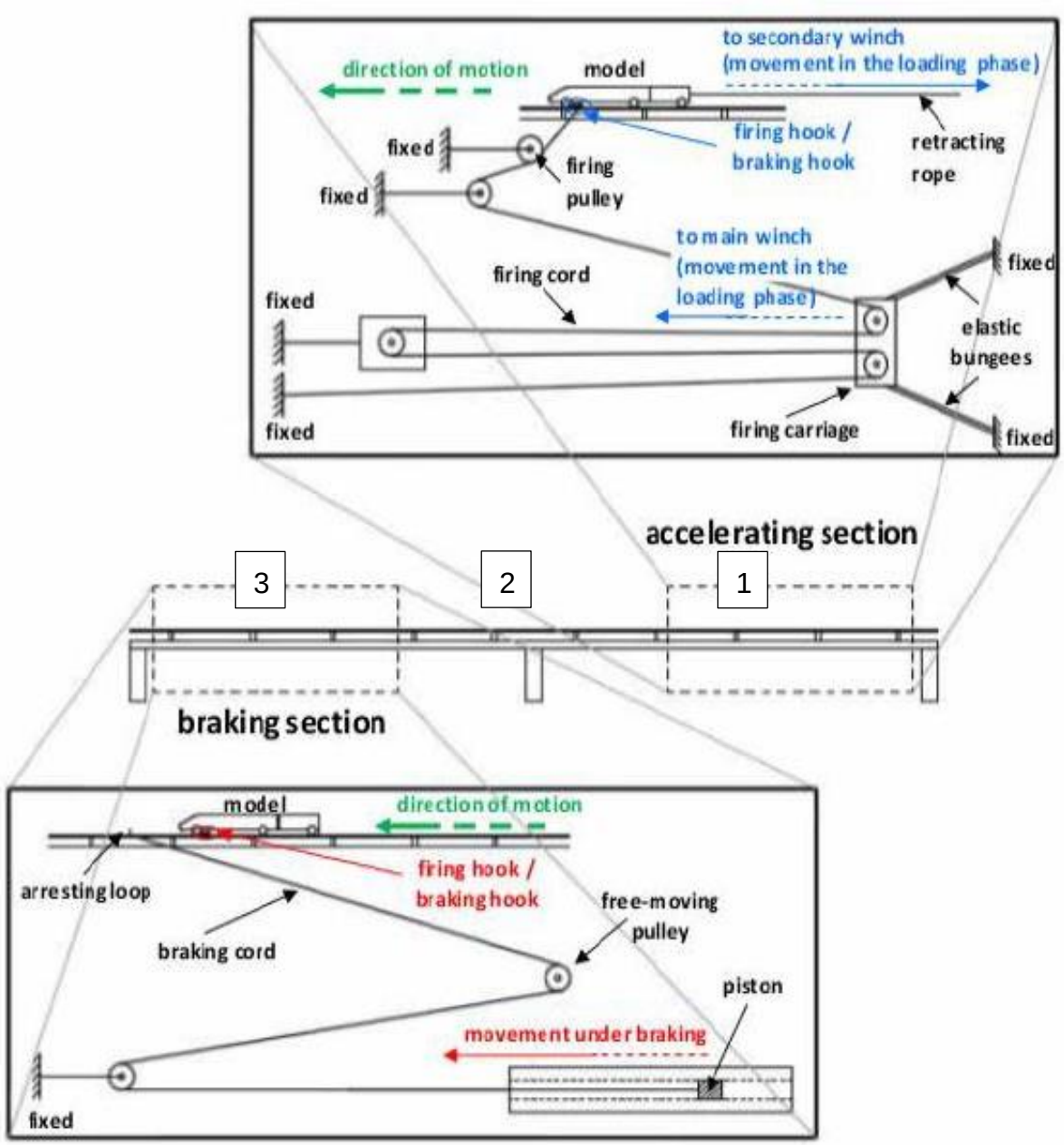

Figure 3.1: Schematic of sections 1, 2 & 3 of the TRAIN Rig, accelerating, testing and braking section respectively (Dorigatti, 2013)

3.2.1 **Model-scale train**

‘’The term ‘train’ in this study refers to a Class 66 locomotive which is connected to FEA type B wagons carrying containers’’ (Iliadis et al., 2018, p. 3). ‘’The use of container freight is justified by the fact that it is among the largest freight sections in the UK (Soper, Baker and Sterling, 2015)’’ (Iliadis et al., 2019, p. 2-3). ‘’Simplifications were made both on the locomotive and wagons, and more details about them can be found in the study of Soper, Baker and Sterling (2014). The shape of the train nose and front cross-sectional area have been retained, as these are believed to be the main factors influencing the development of the pressure waves in the tunnel. The bogie region is highly simplified and it is accepted that the flow at this region will differ from the real full scale train. Similarly, the underbody region of the FEA wagons is simplified at the same level. The current scaled model has been used in the study of Soper (2014) for slipstream measurements where the shape of the train at the sides, roof and underbody play a significant role, and satisfactory agreement with full scale data was obtained’’ (Iliadis et al., 2018, p. 3). Soper (2014) presented the detailed geometric features of the model-scale train, which are presented in Figure 3.2. Moreover, a visual comparison between the real full scale train and the scaled model can be found in Appendix A.

The scale of the model is 1/25th and its dimensions are 0.85m length, 0.106m width and 0.156m height. The length of each wagon is 0.8m. The containers are represented by a square box with a smooth surface at the roof and sides. This differs from the real surface of a container which is relatively rough. However, roughness

effects are considered to be negligible due to the size of the model compared to full scale. The interior of the train is designed to accommodate measuring equipment. More details about the setup are given in section 3.3.2. Figure 3.3 shows that the train surface is drilled for pressure measurement purposes.

a) Train Rig CLASS 66 model

b) TRAIN Rig FEA-B wagons model

c) TRAIN Rig CLASS 66 bogie

d) TRAIN Rig FEA-B wagon bogie

Figure 3.2: Detailed model used at the TRAIN Rig (Soper, 2014)

Figure 3.3: Model-scale locomotive connected to 4 container wagons (case 1). The locomotive surface is drilled to accommodate the pressure taps.

3.2.2 **Train length (cases 1 and 2)**

Two different train lengths have been used for this study. Case 1 consists of the Class 66 locomotive connected to 4 fully loaded container wagons. To investigate the effect of train length (case 2 in Figure 1.1), the number of wagons increases to 8.

3.2.3 **Loading configuration (case 3)**

Previous slipstream studies have tested a wide range of loading configurations and showed significant variation between them (Soper, 2014). For this study, the two

extreme cases of loading configuration have been tested. The fully loaded and partially loaded trains are illustrated in Figure 3.3 and Figure 3.4 respectively.

‘’For the partially loaded train, a number of containers were removed. The remaining containers were placed in the middle of each flatbed, representing 33% of the fully loaded case (by volume)’’ (Iliadis et al., 2018, p. 3). The train consists of 8 wagons, allowing direct comparison to the fully loaded results.

Figure 3.4: Partially loaded train (33%) with 8 wagons (case 3)

3.2.4 **Measurement of the train speed**

Train speed is measured before and after entering and exiting the tunnel respectively, thus detecting any speed reduction. The equipment used for these measurements are light sensors which are activated when the train passes by. There are 4 pairs of photoelectric sensors, with each pair consisting of two sensors opposite to each other (see Figure 3.5). Pairs 1 and 2 were placed before the tunnel entrance one meter away from each other (see Figure 3.6) and pairs 3 and 4 were placed at the exit of the tunnel. This setup is capable of detecting the train speed instantly using the time difference between the activation of each set of sensors and the distance between them.

Figure 3.5: Four pairs of light sensors

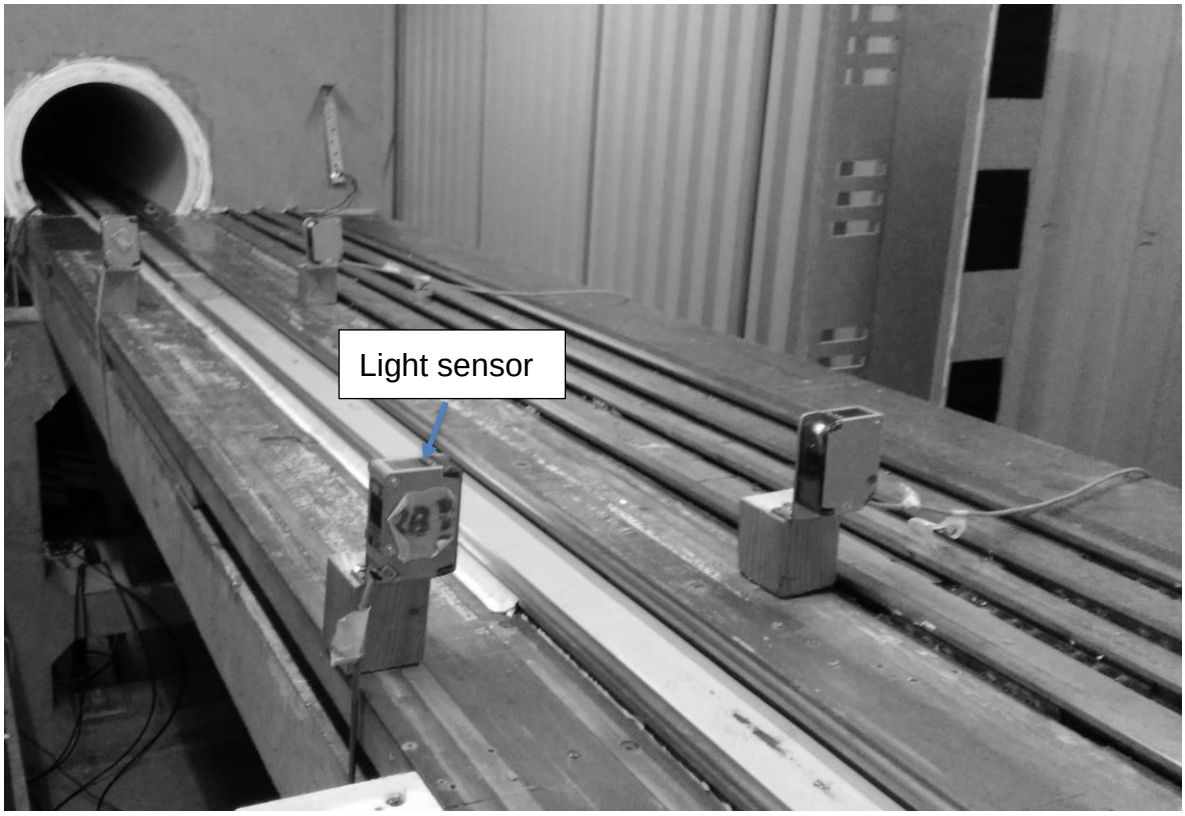

Figure 3.6: Pairs of light sensors at the tunnel entrance

The maximum deflection from the required speed is 1%, ensuring alignment with current codes of practice (CEN, 2010). The two speeds (before entry and after exit from the tunnel) are recorded for every run. Plots of train speed in this thesis represent the average speed of all runs.

3.2.5 **Position of the train**

The position of the train in relation to the pressure histories is monitored for interpretation of results. A stationary trackside laser light at the tunnel entrance and two light detectors are used, connected to the onboard and stationary data loggers. For the onboard sensor, a sharp voltage increase occurs when exposed to the laser light, which is recorded by the data logger. The stationary light detector is connected to the data loggers next to the track and its voltage decreases when the train front passes by (as it prevents the light from reaching the detector). Post-testing, the voltage outputs are analysed, showing the train entry in relation to the pressure histories, which are recorded simultaneously by the same logger.

Figure 3.7 and Figure 3.8 show the position of the sensors. The laser light and the stationary sensor are located far enough from the centre of the track to avoid influencing the flow in the area of interest.

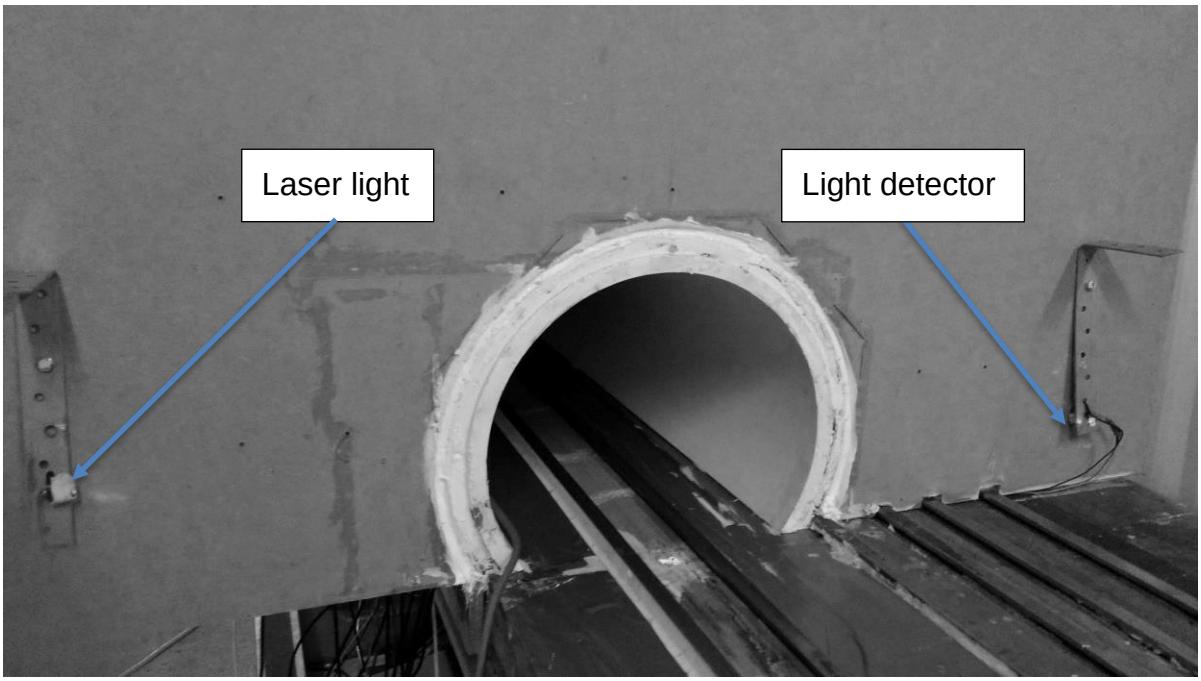

Figure 3.7: Laser light and detector at the tunnel entrance wall

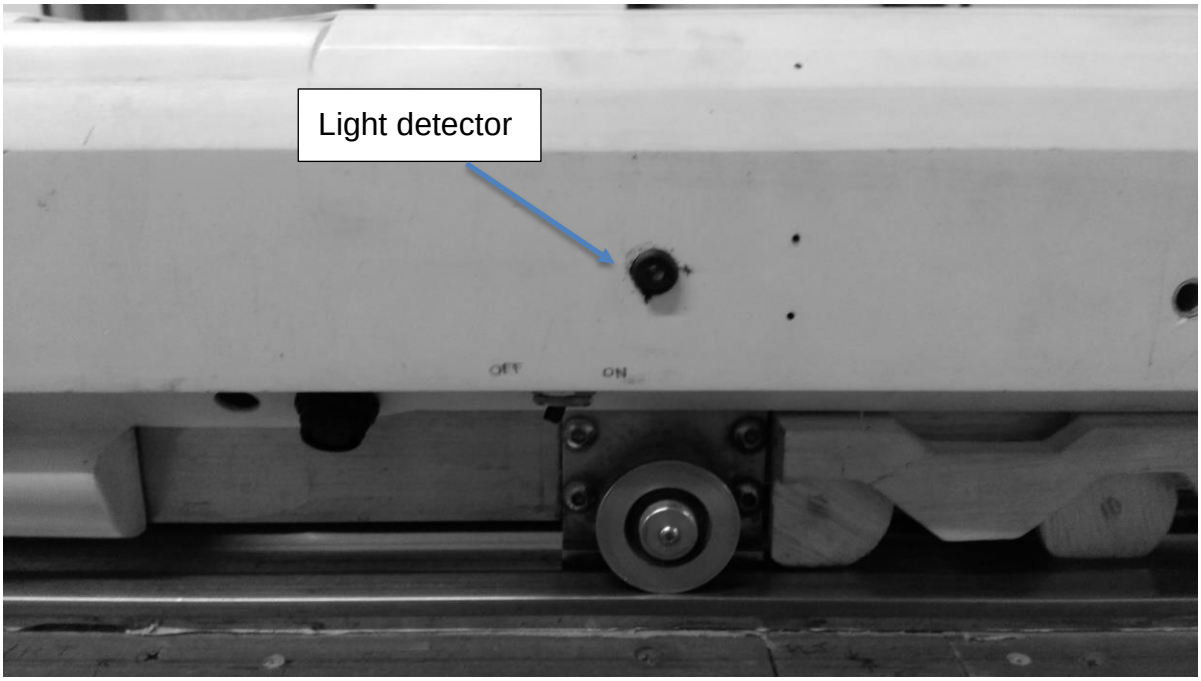

Figure 3.8: Light detector at the side of the train, connected to the onboard data logger.

3.2.6 **Tunnel**

The surface of the tunnel was drilled to accommodate the pressure taps. A metal tube was inserted into the hole leading directly to the pressure transducer. The transducer is connected to a reference pressure tube located underneath the tunnel and away from the area of influence, ensuring that the correct reference pressure is used.

The tunnel is composed of several sections connected together into the final assembly, which is 22.98 meters long. The connections are sealed using silicone and a pressure test is performed to ensure no leakage. During the leakage tests, the two ends of the tunnel are temporarily sealed and the tunnel is pressurised up to 2000kPa, which is higher than the pressures expected during the experiments. Pressure is monitored over time to ensure no drop.

3.2.7 **Data recording**

All signals (pressures, train position) are recorded using data loggers which are activated prior to performing the experiment. In addition to the data mentioned above, information about the room temperature, humidity and ambient pressure are recorded.

3.3 Measurement positions

3.3.1 Tunnel surface measurements

‘’The pressure taps are perpendicular to the flow direction, directly connected to the piezoresistive amplified differential low pressure sensors’’ (Iliadis et al., 2018, p. 3). The HCLA0025B sensors are manufactured by First-Sensor, generating analogue output signal and providing a corrected pressure value by running a cyclic program. More details about the sensors can be found in the technical datasheet (First-Sensor, 2013).They calculate the difference in pressure of two ports (high and low pressure), which are the monitoring pressure and the reference pressure respectively. The output signal of the device is 2.25±2V where 2.25V is the zero pressure offset. ‘’The voltage (V) output is zeroed with respect to the first 1000 samples and converted to Pascal (Pa) using equations calculated from a series of Betz anemometer calibrations’’ (Iliadis et al., 2018, p. 3). The operating pressure of the sensors is ±2500Pa, with a burst and proof pressure of 50×10^6 Pa and 75×10^6 Pa respectively. The typical non-linearity and hysteresis of this device is ±0.05 while the response delay according to the manufacturer is 0.5ms. The sensors have not been used before this experiment and they are provided calibrated and temperature compensated.

For monitoring pressure, a reference pressure is required, obtained through a two-meter plastic tube. During preliminary tests, this distance from the tunnel walls has been found to be adequate to ensure no influence from the train motion.

The twelve pressure measurements at the tunnel walls were obtained through the use of a sixteen-channel data logger where each sensor corresponds to a single channel number. They are connected to the power supply and the data logger through a ground channel and voltage output channel.

‘’Data are recorded with a frequency of 1000Hz. The measurements consist of four-measurement locations across the tunnel length (22.98m long) at 2, 4, 8 and 16 metres away from the entrance (see Figure 3.9). Three measurements points along the radius of the tunnel are monitored to confirm the continuity of the pressure waves in this direction (Figure 3.10). Previous studies have shown that the pressure waves are essentially planar (Ricco, Barron and Molteni, 2007). As the data presents consistency between subsequent runs, three runs are adequate for sampling’’ (Iliadis et al., 2018, p. 3).

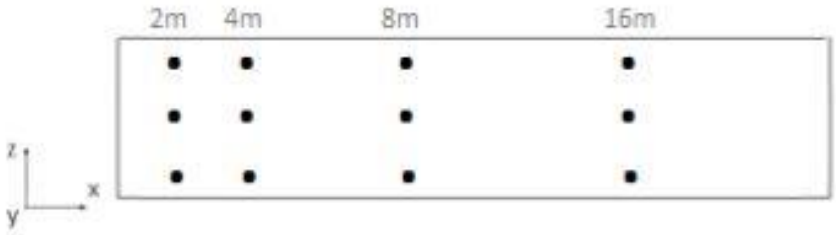

Figure 3.9: Location of the pressure taps at the tunnel walls and distance from the entrance

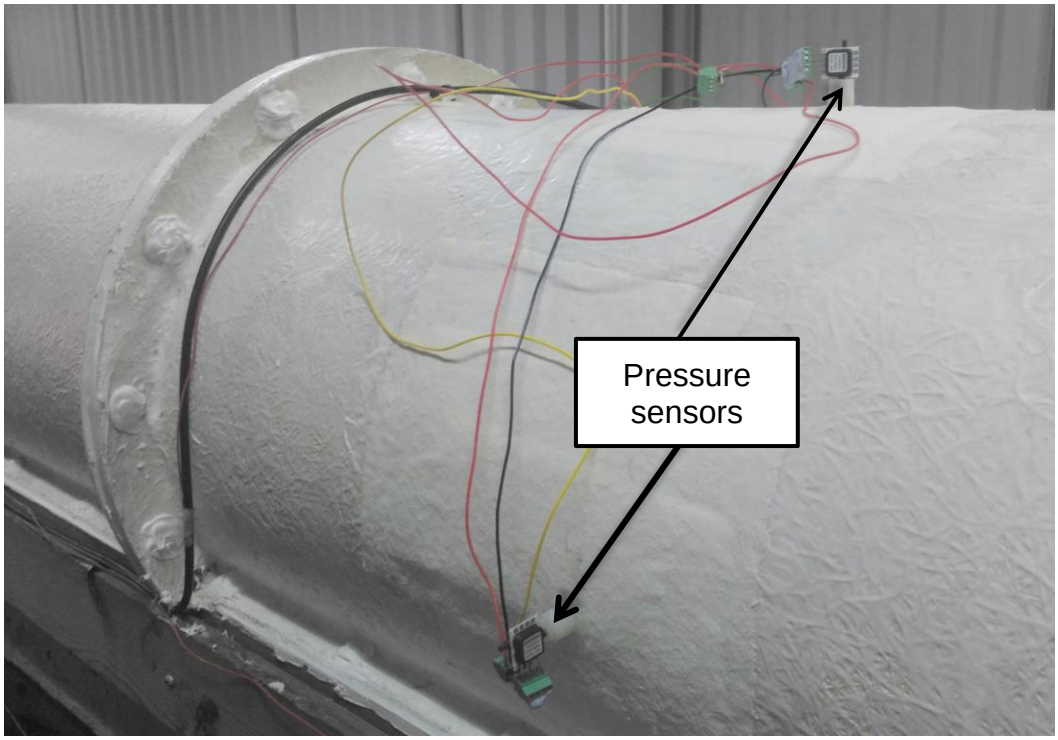

Figure 3.10: Pressure sensors along the diameter of the tunnel

3.3.2 **On-board measurements**

On-board measurements can unravel important information regarding the interaction of the separated flow around the locomotive with the pressure transients. The tests are divided into 2 sets (front and centre/rear pressure taps) due to the limited number of ports on the data logger. There are 30 measurement points in total, 9 at the front, 11 at the LHS and 10 at the RHS (see Figure 3.11). A sealed box connected to a manifold is used (see Figure 3.12) representing the reference (atmospheric) pressure of the sensors.

The surface of the locomotive was drilled, to accommodate the sensors using hollow metal adapters (see Figure 3.13). Similarly to the tunnel wall measurements, transducers with a range of ±2500Pa are used. The selection of this range is based on the expected values of pressure, drawn from similar previous studies of passenger trains in tunnels, including a safety margin. This type of sensors has been extensively used and proved in the TRAIN Rig facility and provided high quality data. Post testing, calibration of the pressure sensors showed negligible effects, proving that the pre-testing calibration was adequate.

‘’The sensors are connected to the metal adapters through a plastic tube. The tube has an inner diameter of 0.16mm and is 25cm long. A correction has been applied using the inverse tubing system transfer function to account for distortion effects. The correction method uses a speaker system to sweep through different frequency ranges to highlight any issues. The method is detailed in the paper of Irwin, Cooper and Girard (1979) and compares the distorted results to a reference measurement (without tube), to obtain a transfer function and correct the data. The on-board system is shown in Figure 3.12 and Figure 3.13. The in-house data logger records data with a frequency of 4000Hz while the results are ensemble averaged over a minimum sample of 15 runs due to the turbulent nature of the flow. 9 pressure taps are placed on the nose, and 20 pressure taps at the side and roof of the locomotive. Both sides of the train are tested, for capturing 3-Dimensional effects such as vortices. Moreover, a light detector is fitted on the locomotive, connected to the 16th channel of the logger. It detects the light sources at the entrance and exit boundaries of the tunnel for

recording the train location'' (Iliadis et al., 2018, p. 3). The figures below show the details of the onboard measuring system and its setup.

.

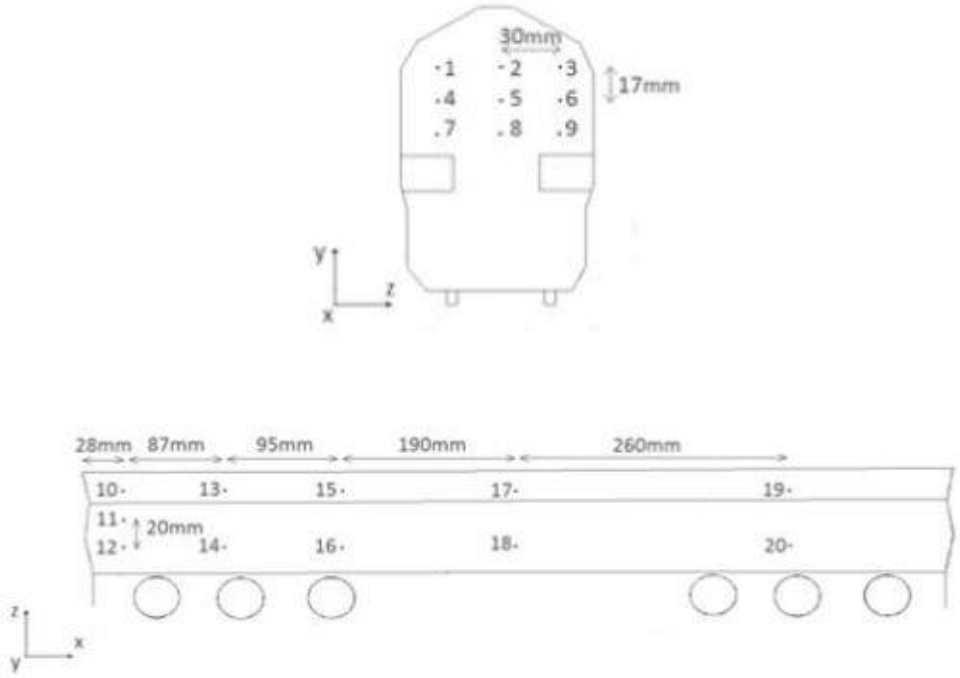

Figure 3.11: Position of measurement sensors on the surface of the locomotive

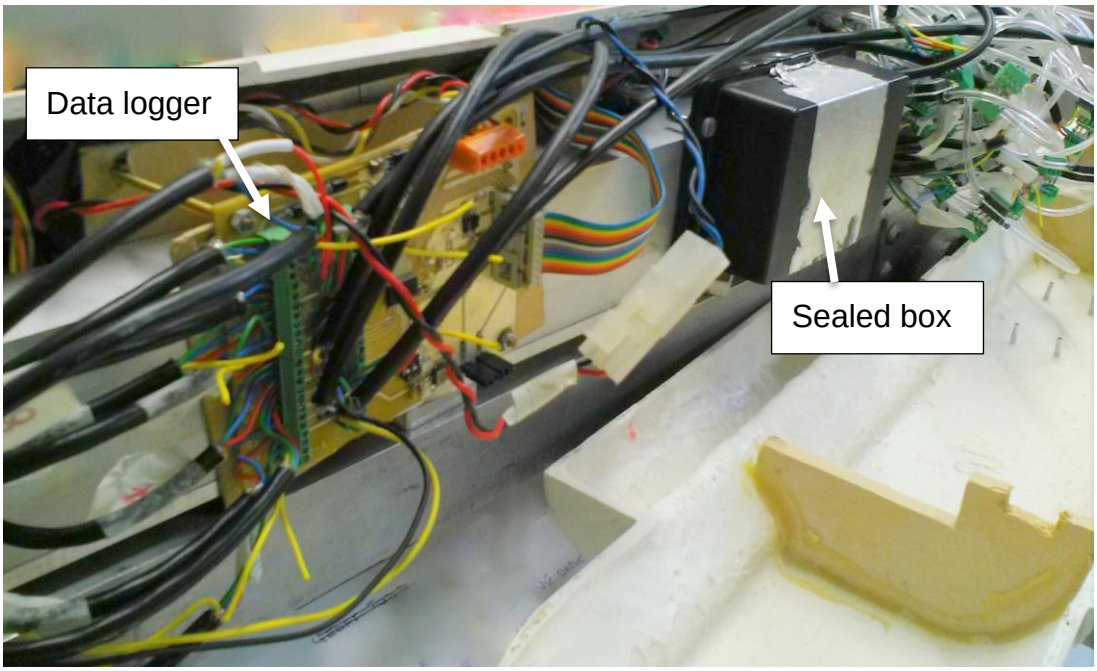

Figure 3.12: Onboard data logger and sealed box

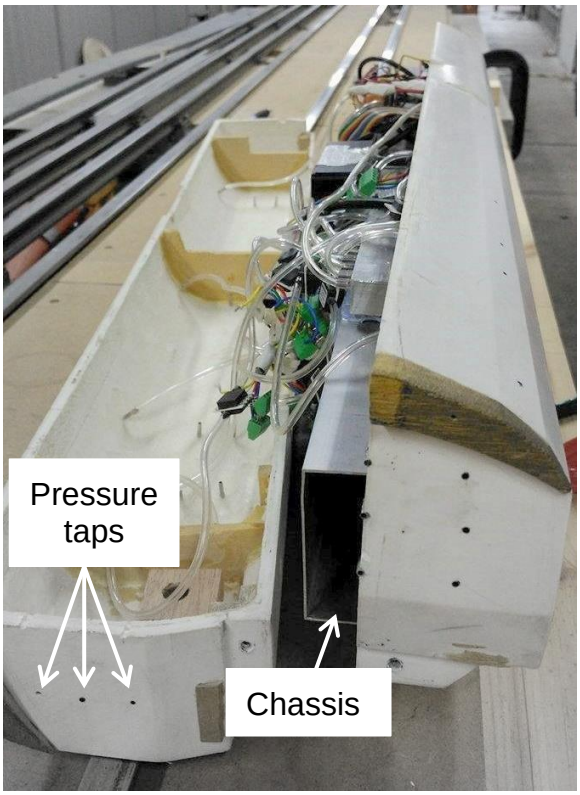

Figure 3.13: Onboard measurement system around the chassis

3.3.3 **Entrance wall measurements**

Since the effect of entrance portal shape affects the pressure transients, these measurements can demonstrate how the displaced air around the freight train affects the pressure histories at this location. The effect of loading configuration and train length is also explored. A total of 11 sensors are attached on the entrance wall, at various locations in the horizontal and vertical direction (see Figure 3.14 and Figure 3.15).

Pressure is expected to be significantly lower in this area compared to inside the tunnel, thus lower range sensors are used for better accuracy. The sensors have a range of ±1250Pa with proof and burst pressures of 25×10^6Pa and 50×10^6Pa respectively (First-Sensor, 2013). Data is recorded with a frequency of 1000Hz and averaged over a minimum of three runs.

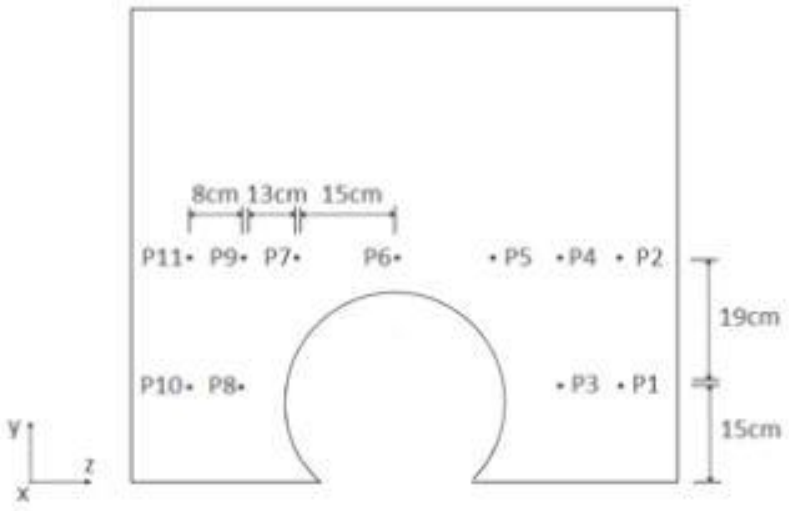

Figure 3.14: Schematic of the location of pressure taps at the entrance wall

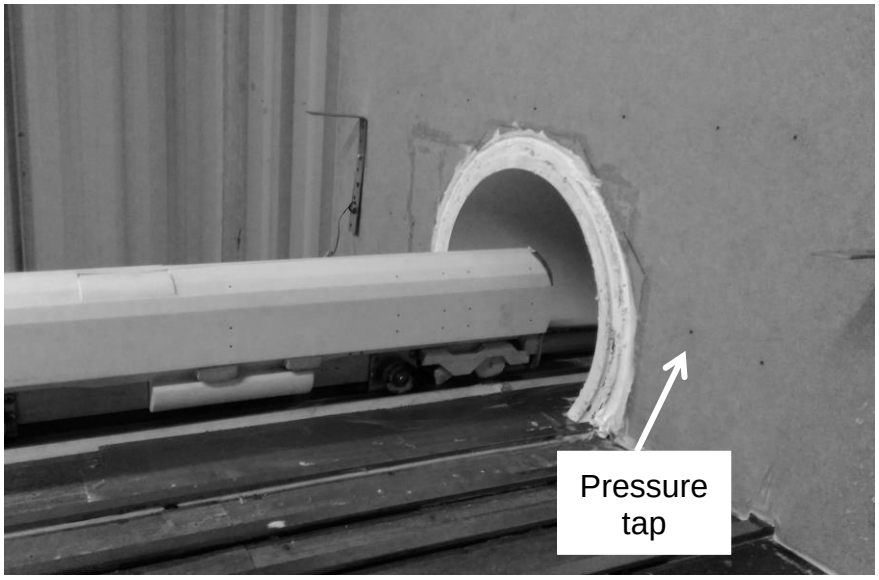

Figure 3.15: Location and size of the entrance wall in relation to the train

3.4 **Geometric and flow parameters (cases 1-3)**

Table 3.1: Parameters, adapted from (Iliadis et al., 2018, p. 4). All values are full-scale apart from the Reynolds number and characteristic length.

Locomotive	Class 66
Container wagons	FEA Type-B
Number of wagons	4 & 8
Total train length L	99.75 & 182m
Model-scale	$\frac{1}{25}$
Train cross sectional area	9.08m^2
Tunnel length	574.5m
Tunnel cross sectional area	45m^2
Train speed	33.5m/s
Re (Scaled model)	384,000
Characteristic length (Scaled model)	0.156m (locomotive height)
Blockage ratio	0.202

Chapter 4

CFD Methodology

The majority of sections 4.2, 4.3, 4.4.1, 4.5.2, 4.5.4, 4.5.5.1 and 4.9.1-4.9.4 has been published elsewhere, see Iliadis et al. (2019). The author of this thesis is the first author of the published journal article.

4.1 Introduction

The numerical methodology presented in this chapter describes the set up details for cases 4-8 in Figure 1.1. For all cases, the sliding mesh technique with unsteady RANS is used. The simulations for case 4 consist of a simplified Class 66 model connected to 8 fully loaded container wagons. As the geometric and flow parameters are the same to the experimental model described in Chapter 3, validation of the results is included in this chapter.

The remaining cases (5-8) have modified geometrical features such as nose shape and different loading configuration.

4.2 Geometry for Case 4: simplified Class 66 connected to 8 container wagons

A simplified 1/25th scale model Class 66 locomotive connected to 8 flatbed wagons with containers has been used, combined with a circular tunnel of constant radius. The locomotive has a maximum length, height and width of 0.85m, 0.156m and 0.106m respectively (scaled dimensions). The bottom surface of the locomotive and container wagons have been significantly simplified, represented by a fully filled box. It has been found that for the flow around a Class 66 locomotive, simplifications at the bogie of the train do not prevent from obtaining slipstream magnitudes which are comparable to the real full size train (Soper, 2014).

The focus of this study is on the upper part of the train, of which the shape is identical to the full-scale train. It has been ensured that the nose shape has been retained for a valid computation of the pressure transients. A visual comparison between the real Class 66 and the scaled experimental numerical model can be seen in Appendix A.

The simulation starts with the train nose located 8 meters away from the tunnel portal, replicating the experimental conditions. The orientation of the coordinate system can be seen in Figure 4.1. The origin of the vertical (y) and lateral (z) axis is at the ground and centre of the track respectively.

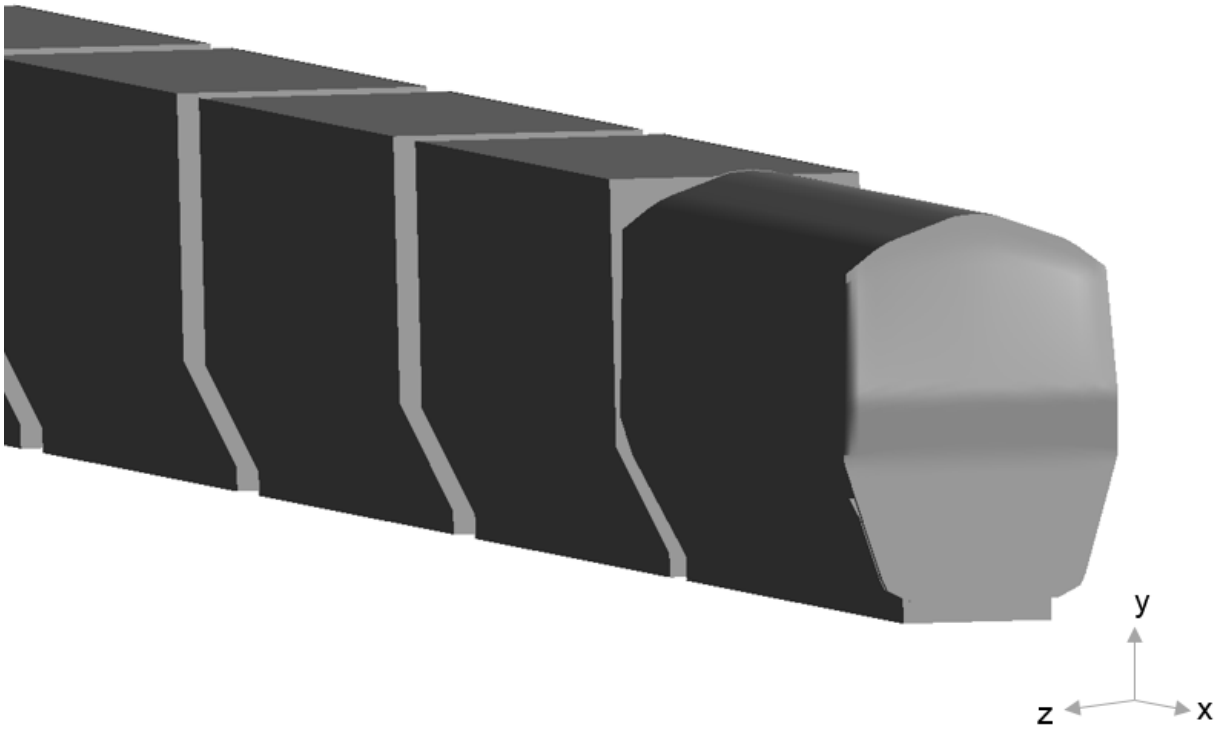

Figure 4.1: Simplified CAD model of the Class 66 locomotive connected to 8 wagons

4.3 Sliding mesh technique

The sliding mesh technique allows for the relative motion between the train, ground and tunnel. The moving domain slides along the stationary domain in the longitudinal direction with a speed of 33.5 m/s, where the location of the former is updated at each timestep. The two domains exchange information at a Generalized Grid Interface (GGI) (non-conformal interface) that connects them. More details about the GGI are given in the following sections.

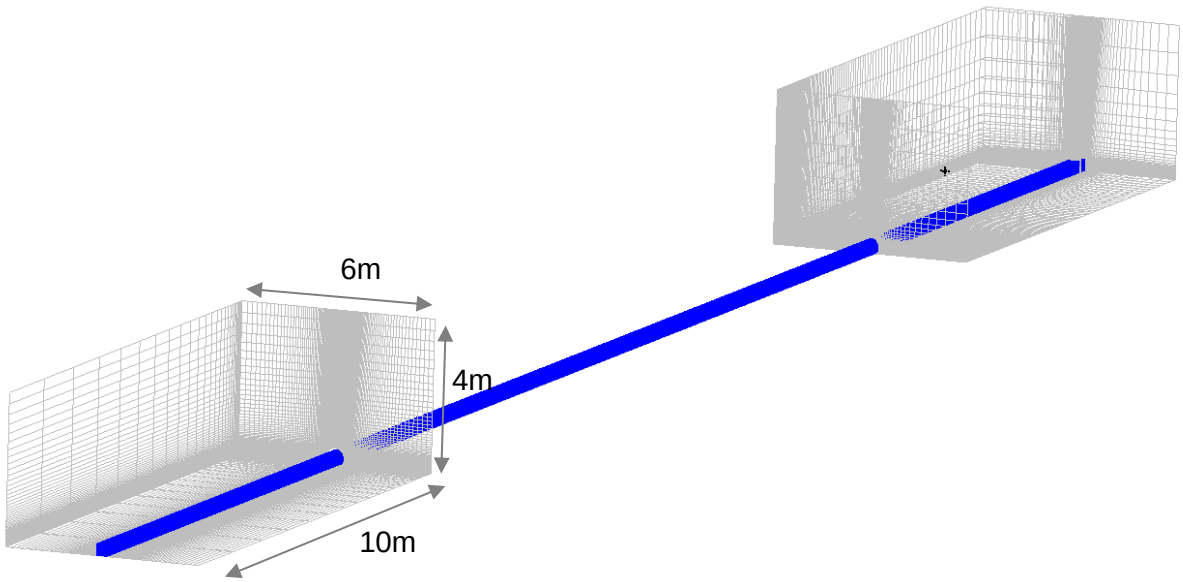

Figure 4.2: Stationary domain in grey and moving domain in blue

4.3.1 **Generalized Grid Interface (GGI)**

The use of GGI allows the transfer of data between faces of which their sizing does not match. This is necessary as the mesh density between the stationary and moving domain is different. At the same time, the GGI performs surface trimming of extended surfaces that cause mismatch and fixes gaps at the interface (subject to the size of the gap being ½ of the touching elements at the interface). At the interface, the fluxes are treated fully implicitly and there is conversation of mass, momentum, energy, scalars and other properties.

The fluid to fluid interface has been selected, as the interface is located at a small distance from the walls. Four interfaces have been created, surrounding the train from

the top, bottom and sides. Although the faces are non-conformal, identical size of the connecting faces and volumes has been achieved.

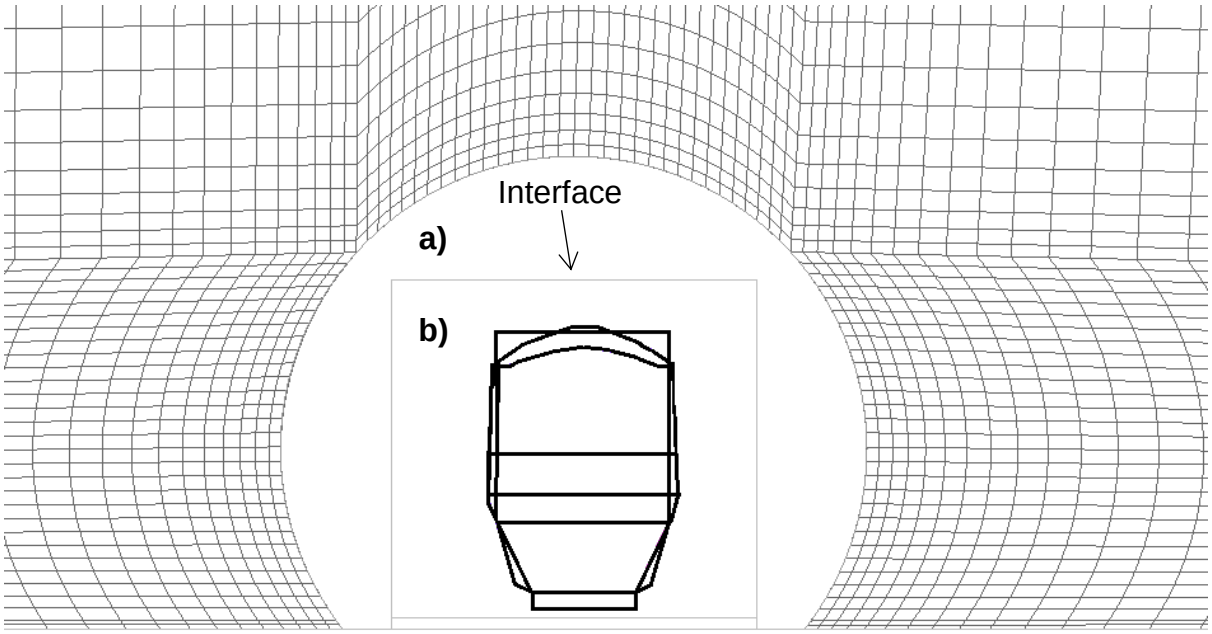

Figure 4.3: The stationary (a) and moving (b) domains exchange information at the interface.

4.3.2 **Speed definition**

The speed of the moving domain is defined through the CEL expression $t * 33.5[m]/[s]$, imposing a constant speed throughout the simulation. In general, CFX Expression Language (CEL) is used to declare values that cannot otherwise be defined in the solver.

4.4 Domain discretization

The mesh generation process aims to discretize the spatial domain using volume elements, where a set of governing equations are solved for each of them. Using ICEM CFD, a structured hexahedral mesh is generated with H-topology. This is a body fitted grid generated using a multi-block approach (see section 4.4.2). ‘’All edges use a node expansion ratio less than 1.2, which is constant along its length. The sizes of cells near the interfaces allow a smooth transition between the two domains. Three different mesh densities were used; 2.8×10^6, 3.2×10^6 and 4.2×10^6 elements. The moving mesh is finer near the train nose to capture the fine scales of the thin separated bubble region’’ (Iliadis et al., 2019, p. 4).

4.4.1 Structured mesh advantages

Structured mesh has been preferred over unstructured on the basis of generating a high quality and time efficient discretized domain. The treatment of boundary conditions together with the calculation of fluxes and gradients is easier for structured grids (Blazek, 2015). In addition, the number of elements required to fill the computational space is lower due to efficient space filling. From the solver’s perspective, structured mesh has the following advantages:

- Better alignment between the grid and flow
- Improved convergence
- Reduced CPU time

4.4.2 **Blocking strategy**

The mesh has been generated through the process of blocking where the domain is divided into a number of blocks. Blocks are virtual areas where mesh parameters such as sizing can be defined locally, based on the shape of the geometry. The moving domain is composed by 376 blocks while the stationary domain by 44. Based on the adopted blocking strategy, this is the number of blocks required to accurately define the geometry. Smaller size blocks are required in areas of high curvature and relatively small size geometry features. Appendix C contains a visual representation of the blocks in the moving and stationary domain.

The top down blocking strategy adopted starts from a single 3D block, dividing it into smaller parts. The edges and faces of the block have been associated to the curves and surfaces of the geometry respectively. Due to nature of the sliding mesh method, associating faces to surfaces is critical to ensure correct alignment of the interface surfaces. The underlying geometry acts as a guide for the mesh to define the geometry accurately.

4.4.3 **Sizing**

The size of the elements is smaller near the areas where small scale effects are expected to occur.

In the longitudinal direction, the size of elements is smaller near the train nose and the upper half of the train where the flow field analysis focuses. In the vertical and

lateral directions, mesh density increases with distance from the train surface and then reduces again near the tunnel walls. Finer mesh has been generated near the tunnel entrance and exit where reflection of the pressure waves and emission of micro-pressure waves take place. The largest elements are found near the outlet boundaries, away from the tunnel boundaries. Small scale effects are not expected to occur at these regions, and the flow is not affected by the pressure transients inside the tunnel.

The sizing of all edges is defined by the exponential mesh law below, provided in the theory guide of ICEM CFD (Ansys, 2015a).

$$S_i = Sp1 \cdot i \cdot e^{R(i-1)} \tag{7}$$

where

S_i is the distance from the starting end to node i

Sp1 is the spacing of the first cell in the edge

N is the total number of nodes in this edge

R is the growth ratio

$$R = \frac{-log\lfloor (N-1) \cdot Sp1 \rfloor}{N-2} \tag{8}$$

The spacing in the first cell and its expansion ratio vary for different edges. It has been ensured that R is less than 1.2 for all edges across the domain to ensure no

accuracy or convergence problems in the solver, by controlling the discretization error.

Figure 4.4 shows the surface mesh at the stationary and moving domains while Figure 4.5 represents the mesh distribution at the train surface.

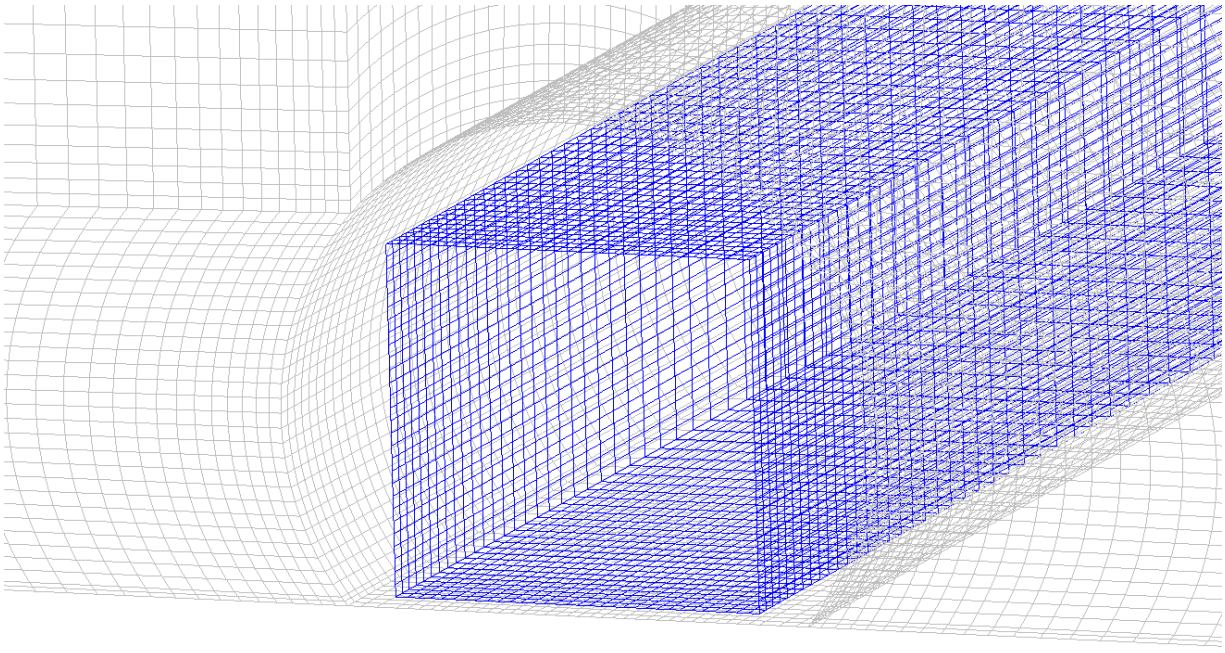

Figure 4.4: Mesh sizing at the moving and stationary faces. Stationary faces in grey and moving faces in blue.

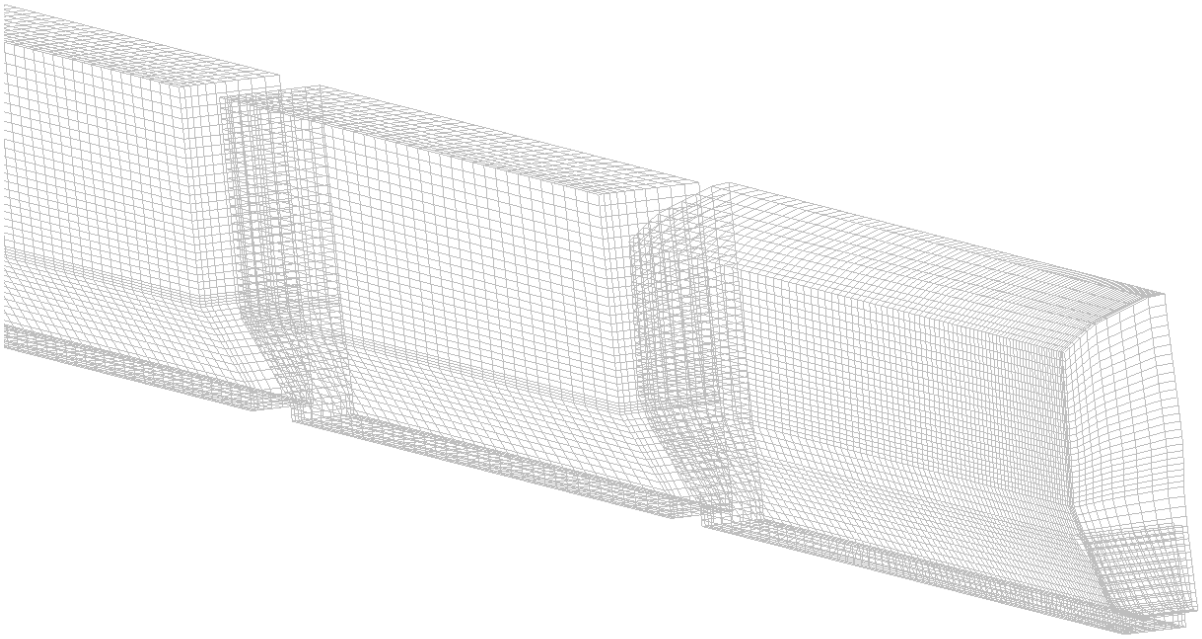

Figure 4.5: Mesh distribution at the train surface

4.4.4 **Mesh quality**

Prior to importing the mesh into the solver, it is ensured that there are no negative volume elements, duplicated nodes and overlapping elements. Then, specific mesh metrics are used, based on the acceptable ranges for CFX (Ansys, 2015a). It must be mentioned that non-compliance with the recommended acceptance metrics does not necessarily lead to solution problems.

4.4.4.1 Ansys CFX recommended mesh quality

The recommended/acceptable values for mesh quality are given in the modelling guide for CFX (Ansys, 2015a) and the user manual for ICEM CFD (Ansys, 2015b). The values are compared against the actual values of the fine mesh in Table 4.1.

Dihedral angle shows the angular deviation of two faces from their normal equivalent. Maximum dihedral angle is defined as the maximum angle between two faces which intersect. The acceptance range for CFX is 10-170 (Ansys, 2015a) and the values of the current mesh are between 90 and 161. Thus, the mesh is compliant with the recommended metrics for CFX.

This mesh expansion ratio is applicable to 3-D grids only because it is based on the node centred sector volume, which contains ¼ of each of the 4 cells surrounding the node. Then, this volume is compared to the volumes of the adjacent nodes, in order to detect the maximum expansion factor. According to Ansys (2015a), the maximum acceptable factor is 20. Table 4.1 shows that the obtained values in the mesh are within this limit as the maximum factor is 12.63. Thus, unwanted effects such as convergence and divergence problems due to poor mesh quality can be avoided.

The determinant estimates the deformation of the hexahedral, with acceptance values being higher than 0.3 (Ansys, 2015b). The lowest value in the fine mesh is 0.556, which meets this quality requirement.

Table 4.1: Mesh metrics against acceptable ranges for CFX (Ansys, 2015a) and ICEM CFD (Ansys, 2015b)

	Max dihedral Angle	Mesh expansion ratio	Determinant 3x3x3 (min.)
Acceptable values	10°-170°	<20	>0.3
Fine mesh	90°-161°	1-12.63	>0.556

4.5 Physics and solver setup

4.5.1 Reynolds-Averaged Navier-Stokes Equations (RANS)

Turbulence models solve the transport equations by using the averaged and fluctuating components. Using Reynolds decomposition, the following relation is derived (Ansys, 2015a):

$$U_i = \overline{U}_i + u_i \quad (9)$$

where

U_i *is velocity at node i*

$\overline{U}_i$ *is the average component of the above*

and u_i *is the time varying or fluctuating component*

The time-averaged component of velocity is given by the equation below:

$$\overline{U}_i = \frac{1}{\Delta t}\int_{t}^{t+\Delta t} U_i dt \tag{10}$$

Substituting the above equations into the transport equations gives the equations below:

$$\frac{\partial \bar{p}}{\partial t} + \frac{\partial}{\partial x_j}\left(\rho \overline{U}_j\right) = 0 \tag{11}$$

$$\frac{\partial \rho \overline{U}_i}{\partial t} + \frac{\partial}{\partial x_j}\left(\rho \overline{U}_i \overline{U}_j\right) = -\frac{\partial \bar{p}}{\partial x_i} + \frac{\partial}{\partial x_j}\left(\tau_{ij} - \rho\overline{u_\iota u_J}\right) \tag{12}$$

where

τ is the molecular stress tensor

$\rho\overline{u_\iota u_j}$ *is the Reynolds Stresses*

Similarly the Reynolds averaged energy equations are given below:

$$\frac{\partial \bar{p}\bar{h}_{tot}}{\partial t} - \frac{\partial \bar{p}}{\partial t} - \frac{\partial}{\partial x_j}\left(\rho \overline{U}_J \bar{h}_{tot}\right) \tag{13}$$

$$= \frac{\partial}{\partial x_j}\left(\lambda \frac{\partial \overline{T}}{\partial x_j} - \rho \overline{u}_j \bar{h}\right) + \frac{\partial}{\partial x_j}\left[\overline{U}_i\left(\tau_{ij} - \rho\overline{u_\iota u_J}\right)\right]$$

where

$\rho\overline{u}_j\bar{h}$ *is the turbulence flux term*

$\frac{\partial}{\partial x_j}\left[\overline{U}_i\left(\tau_{ij} - \rho\overline{u_i u_j}\right)\right]$ *is the viscous work term, which has been enabled in the modelling* (14)

The following equations show how the mean total enthalpy is calculated:

$$\bar{h}_{tot} = \bar{h} + \frac{1}{2}\overline{U}_i\overline{U}_i + k \tag{15}$$

where k is the turbulent kinetic energy:

$$k = \frac{1}{2}\bar{u}_i^2 \tag{16}$$

4.5.2 **k-ω SST model**

The two-equation model k-ω SST has been implemented because of its capability to predict separated flow under adverse pressure gradients (Bardina, Huang and Coakley, 1997). It provides accuracy and robustness on near wall treatment and switches to k-ε in the freestream regions, showing lower levels of sensitivity to inlet boundary conditions. k-ω SST is insensitive to y+ values (non-dimensional wall distance) as it uses automatic wall treatment (although specific acceptance ranges are provided for heat transfer simulations that require higher accuracy near the wall) (Ansys, 2015a).

Considering the separation around the train head, SST is an effective choice as the automatic near wall treatment of the commercial code used (Ansys CFX) ensures the

smooth transition from k-ω (near wall) to k-ε (free-stream). It models the transport of turbulent shear stresses through a modified turbulent viscosity formulation.

4.5.3 **Compressible flow**

This is a compressible flow simulation where density is calculated through the ideal gas law. The variation in density is given by the equations below:

$$\rho = \frac{wp_{abs}}{R_0 T} \tag{17}$$

$$dh = C_p dT + \frac{dp}{\rho} \tag{18}$$

$$c_{PR} = c_{PR}\,(T) \tag{19}$$

where

w *is the molecular weight*

p_{abs} *is the absolute pressure*

R_0 *is the universal gas constant*

c_{PR} *is the specific heat capacity at constant pressure*

4.5.4 **Time discretization**

The compressible flow simulation is unsteady over a total time of 1.3s (the time required for the train to pass through the tunnel) with a constant time step of 0.0001s. More details about time discretization are given in the following sections.

4.5.4.1 Advection scheme

The governing equations need to be discretized temporally as the solution is time dependent. The choice of advection scheme plays a critical role on the accuracy and robustness of results. In general, 2nd order schemes have higher accuracy due to reduced discretization error (truncation error tends to be lower at higher order schemes). However, they are less robust (in terms of numerical stability), presenting more unphysical oscillations. On the other side, 1st order schemes are more bounded but less accurate because of larger discretization/diffusion errors (Norris, 2000). The order of the scheme represents the exponent of the leading discretization term $(\Delta x)^2$.

For the current simulations, the high-resolution scheme has been chosen. By default, the high-resolution scheme uses a 2nd order Backward Euler to ensure accuracy but if required, it converts to 1st order Backward Euler to maintain a bounded solution (more stable). They are both implicit schemes which means that they solve the equations by including both the current n and the next state n^{+1}. Implicit schemes however can be more computationally demanding compared to explicit schemes.

The high-resolution scheme has a variable blend factor which changes for each volume element. The value of this factor illustrates at what extend a 1st or 2nd order

discretization scheme is used. For example, a value of 1 shows that 2nd order is used only, and a factor of 0 represents a 1st order scheme. Flow regions with low gradients have a factor near to 1 for accuracy. On the other side, regions where significant changes occur have a factor near to 0 to ensure robustness.

4.5.4.2 Transient scheme

For time-dependent simulations, a transient scheme or discretization algorithm must be defined to solve the transient terms of the equations. The implicit 2nd order Backward Euler scheme has been used due to its accuracy and precision. This is the default Ansys CFX scheme and it is recommended for most transient simulations. Although this is a 2nd order accurate scheme, the turbulence equations are set to 1st order and the fractions equations to a bounded 2nd order scheme, to ensure that they remain bounded.

4.5.5 Boundary conditions

Boundary conditions are used to specify the flow properties at the boundaries of the domain. It is an essential part of mathematical modelling of fluid problems representing the known quantities in the matrix and the starting point of solving the sets of equations. They remain unchanged throughout the simulation, differing from initial conditions which are only used to initialize the domain and to create a stable solution. However, if required, it is possible to set boundary conditions which change with time. The selection of boundary conditions is critical to ensure accuracy,

robustness and convergence of the numerical scheme. Incorrect boundary conditions can result in inaccurate modelling of the flow. The definition of boundary conditions has been based on information known from experiments.

4.5.5.1 Outlets

The faces of the domain which have been set as outlets are shown in Figure 4.6. No inflow is expected at these regions as they are located far from recirculation areas, to realistically simulate the experiments. The flow at these boundaries is subsonic with a normal direction to the boundary and a turbulence intensity of 5%. The relative pressure at the boundary is 0 Pa, representing the absence of effects from the pressure changes inside the tunnel. The temperature is constant at 288 K.

The surface mesh on Figure 4.6 shows the dimensions and boundary conditions applied to the pre-entrance domain. Identical dimensions and conditions have been applied at the post-exit domain.

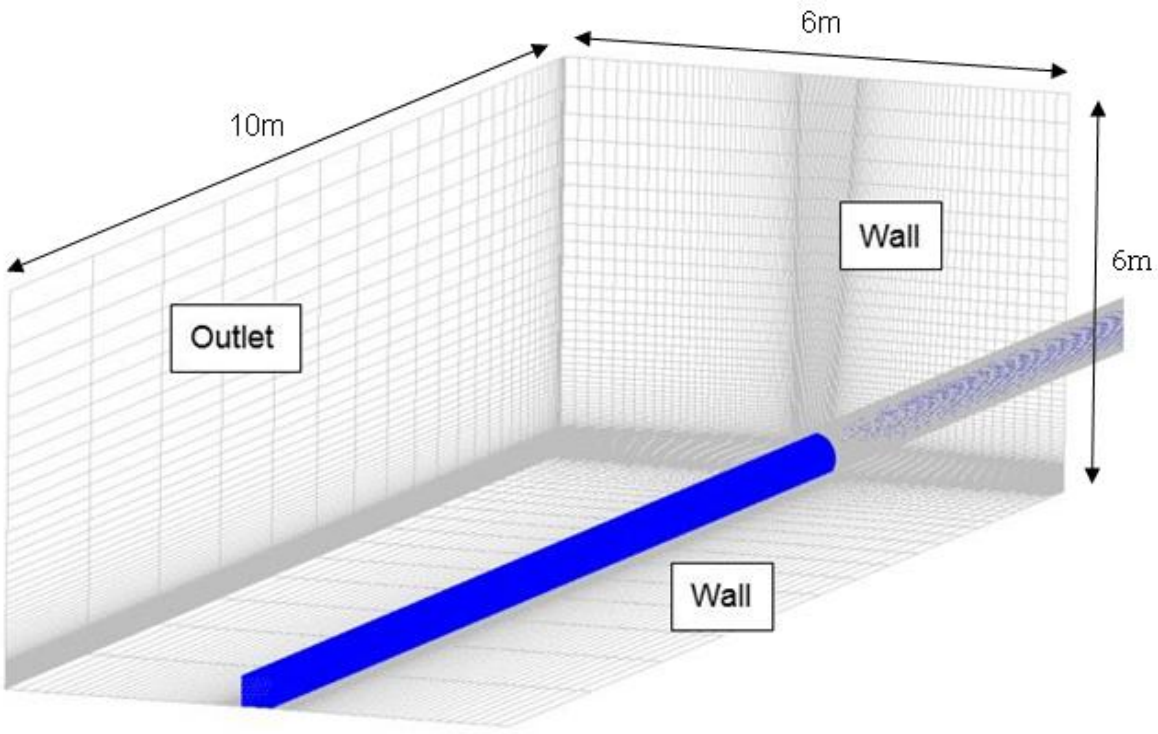

Figure 4.6: Boundary conditions outside of the tunnel. The blue region represents the moving domain. The remaining outlet faces which surround the pre-entrance domain are hidden.

4.5.5.2 Walls

Walls are used to separate fluid from solid regions. The mesh elements defined as walls are the train and tunnel surfaces, ground and tunnel entrance and exit walls (see Figure 4.6). All of them are stationary boundaries apart from the train surfaces which travel towards the longitudinal direction. The no slip condition is enabled and the wall roughness is defined as smooth. The no slip condition imposes that the

velocity of the fluid relative to the wall is 0 and there is no need to solve the momentum equations at the wall.

$$U_{wall} = 0 \tag{20}$$

Adiabatic walls are used, resulting in no heat transfer across the boundary. In mathematical terms, this is expressed as:

$$q_{wall} = 0 \tag{21}$$

4.5.6 **Initial conditions**

Initial conditions give temporary values to the volume elements and act as a starting point for computing the flow field. Then, the solver uses an iterative method to predict the final solution. They are applied to all volume elements except for the ones that boundary conditions have been set. Choosing physical and realistic values is critical because:

- The closer the initialization of the flow field to the final converged solution, the less time it will take for the model to converge and predict the final flow field.
- Unrealistic initial conditions can lead in misbehaviour of the model and divergence.

Post the simulation, it was shown that the initial conditions in Table 4.2 caused no divergence and didn't delay convergence, proving their suitability for this simulation.

Table 4.2: Initial conditions

Parameter	Initial condition
Cartesian Velocity Component U	0 m/s
Cartesian Velocity Component V	0 m/s
Cartesian Velocity Component W	0 m/s
Pressure	0 Pa
Temperature	15°C
Turbulence Intensity	5%

4.5.7 **Convergence**

Convergence is the state that the iterative process has reached a point that the solution does not change with subsequent iterations. It is an essential part of the simulation, and a sign that the solution is trustable, but it cannot be used as a criterion to prove that the solution is true.

In a numerical scheme, the solution starts with the initial values (initialization) and then uses an iterative method to reach a final prediction. During this process, the numerical error reduces. When this error reaches the convergence limit set by the user, convergence is obtained, giving the final solution. For the current simulation, the numerical error is represented by the value of the residual in the equations. Assessing convergence through residuals is common practice in CFD due to its ability to show the local imbalance in the discrete equations of the conserved variable. The Root Mean Square (RMS) of the residual is computed and monitored for convergence.

Ansys CFX uses normalized residuals to provide more consistent criteria. The default RMS residual criterion of 1e-4 has been used. Post the analysis, the results showed very good agreement with experiments, confirming the suitability of this convergence criterion.

For transient simulations, such as the ones presented in this study, convergence needs to be obtained at each timestep. The maximum number of coefficient loops is 20 for each timestep. However, during the simulations it became apparent that approximately 2-3 iterations were adequate to obtain convergence at most timesteps.

4.6 Geometric and flow parameters (case 4)

Table 4.3: Parameters – All values are full scale apart from the Reynolds number, characteristic length and domain size. Adapted from (Iliadis et al., 2018, p. 4).

Locomotive	Class 66
Container wagons	FEA Type-B
Number of wagons	8
Total train length L	182m
Model-scale	$\frac{1}{25}$
Train cross sectional area	9.08m^2
Tunnel length	574.5m
Tunnel cross sectional area	45m^2
Train speed	33.5m/s
Re (scaled)	384,000
Characteristic length (scaled)	0.156m (height of the scaled train)
Blockage ratio	0.202
Size of pre-entrance computational domain (scaled)	x-axis 10m y axis 6m z-axis 6m

4.7 Modifications for cases 5-7: effect of nose shape

The Class 66 head has been modified, resulting in 3 additional nose shapes, representing the transition between the blunt nose of Class 66 and more rounded shapes.

Figure 4.7 shows the 3 shapes built as extensions to the original nose, which means that the overall locomotive length is slightly longer. Nose roundness and length increase simultaneously. The front part of all noses comes from the Class 66 locomotive, but at scaled size. Noses 1-3 do not represent real trains. As a result, in many cases the analysis is qualitative.

These modifications required adjustment of the structured mesh. Figure 4.8 shows the surface mesh at the locomotive front. For all nose shapes (including the original nose), a common blocking strategy, topology and sizing has been used.

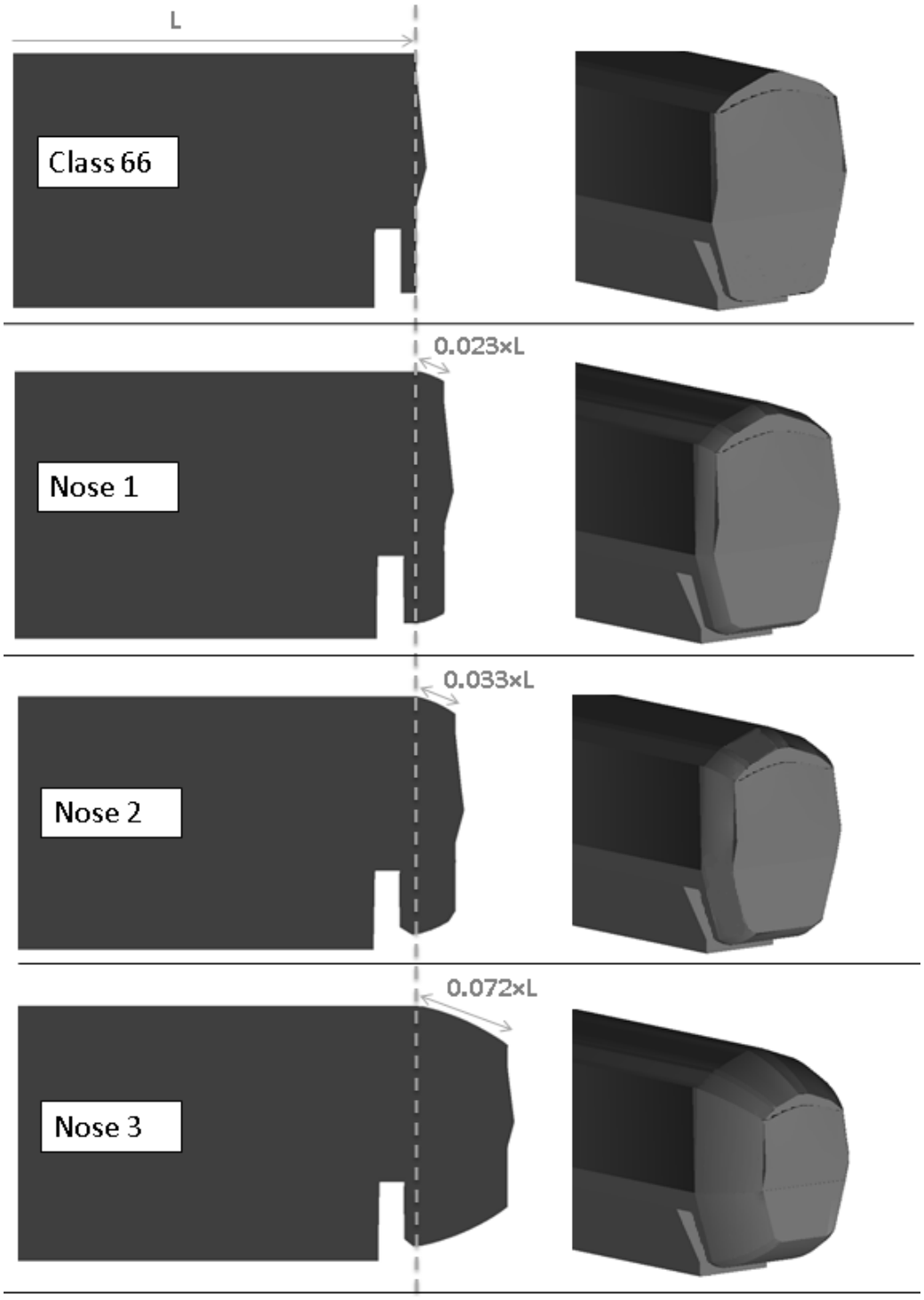

Figure 4.7: Shape transition from freight train to passenger train. L is the length of the Class 66 locomotive. For noses 1, 2 and 3, an extension has been added to the Class 66 locomotive.

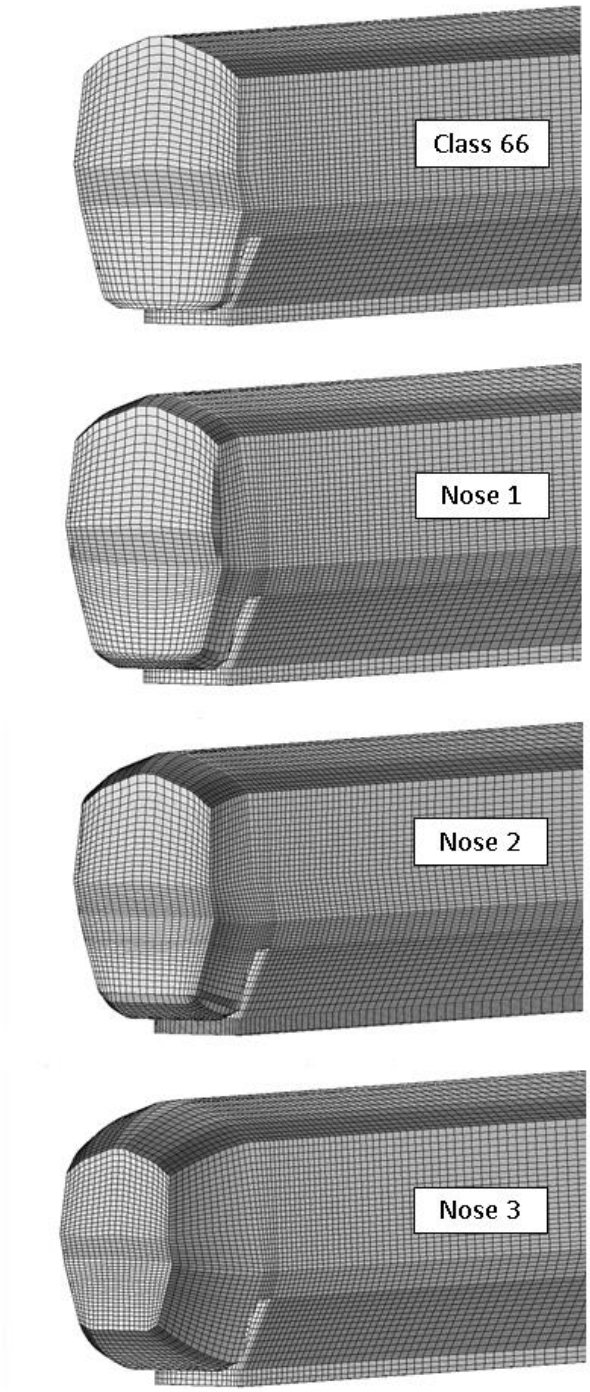

Figure 4.8: Surface mesh at the locomotive nose.

4.8 Modifications for case 8: effect of loading configuration

The modifications presented here are performed to investigate the effect of loading configuration in more detail, using an additional test case. To that end, the containers from wagon 1 were removed, while all other wagons were fully loaded (see Figure 4.9). This loading configuration is different to the experimental model presented in section 3.2.3. Figure 4.10 shows the surface mesh of the partially loaded train which retains the same mesh characteristics as the fully loaded model.

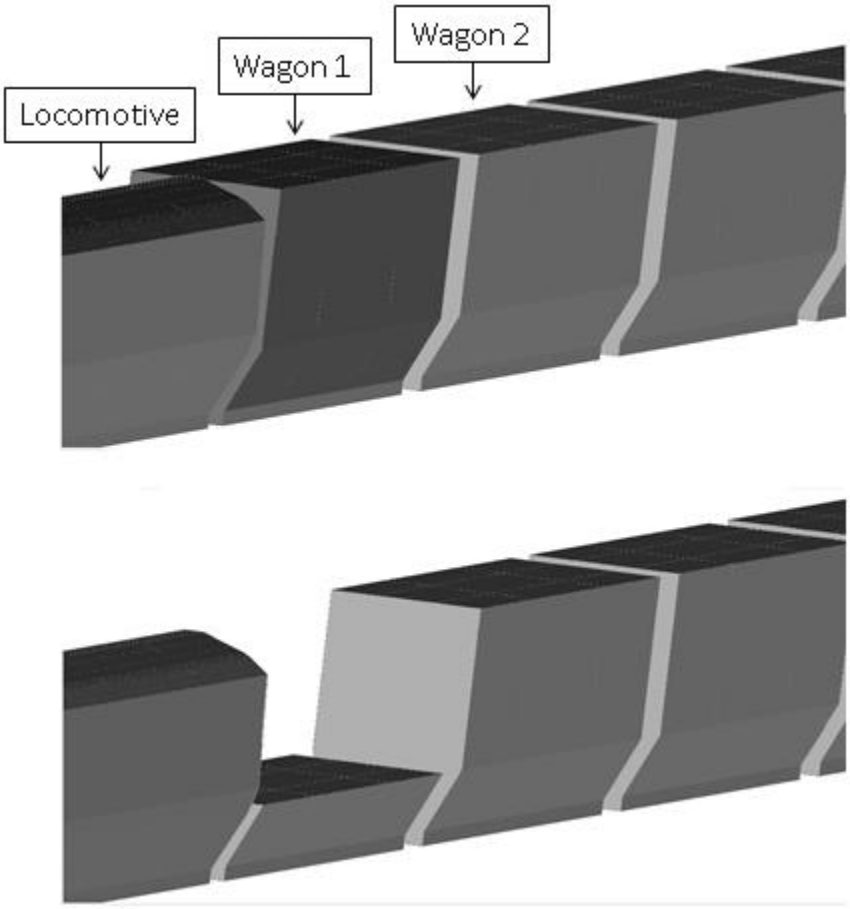

Figure 4.9: Top: Fully loaded train; Bottom: Partially loaded train used in computational simulations. Wagon 1 is unloaded

.

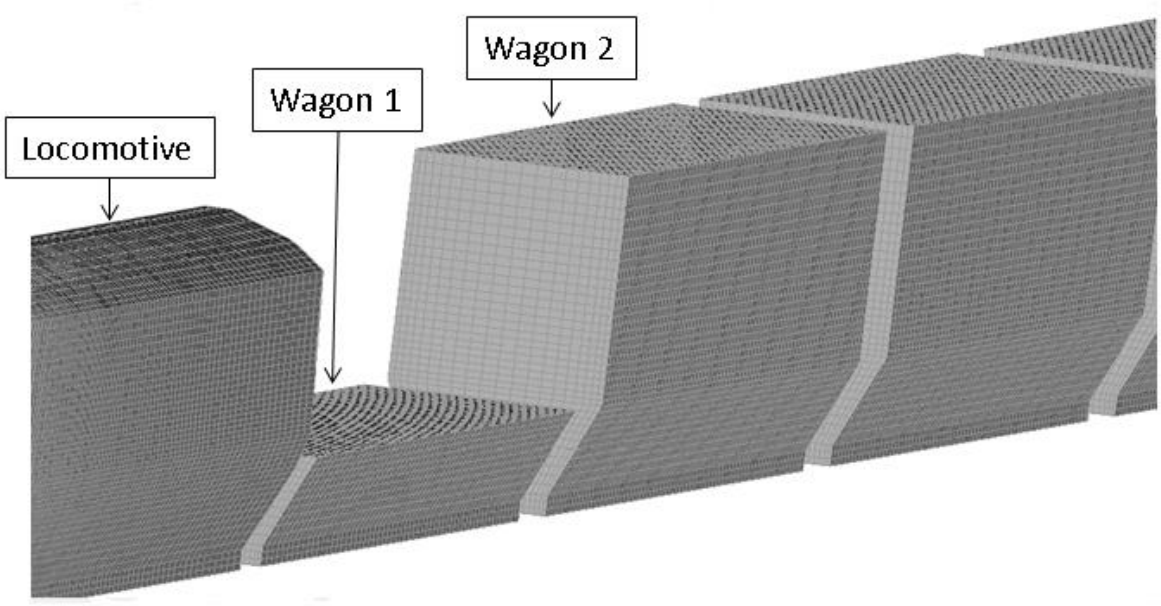

Figure 4.10: Surface mesh for the partially loaded train used in the numerical simulations

4.9 **Model validation**

The numerical model is validated using results from case 4 as follows:

- Mesh and time step independence study.
- Comparison to experiments: The pressure histories at the tunnel walls are compared to the data obtained from case 2 in Chapter 5.
- Comparison to experiments: The open air velocities around the train are validated with the experimental study of Soper (2014), who used the same physical model with the current study.

- Comparison with k-ε: The pressure histories and slipstream velocities are compared to results obtained using k-ε, to validate and confirm that k-ω SST is the most suitable model among potential alternatives.

4.9.1 **Timestep and mesh independence**

For this timestep and mesh independence study, the pressure histories at the tunnel walls have been used. Figure 5.3 shows pressure monitored at two meters from the entrance (see vertical axis) against time, which has been kept in its scaled form (see horizontal axis). Figure 5.3a confirms that the there is no effect on the initial compression wave when increasing the time step. Identical results were found for other measurement points along the tunnel length. Therefore, t=0.0001s has been used to keep the computational time to a minimum. Similarly, grid independence was obtained using three different densities; 2.8×10^6, 3.2×10^6 and 4.2×10^6 elements named as coarse, medium and fine mesh respectively (see Figure 5.3). These grids were generated with the same topology but different sizing to ensure consistency. The differences in the sizing of the three meshes are around the train and inside the tunnel. A mesh independent modelling of the pressure waves is important before validating pressure histories with experimental data. Figure 5.3b confirms that the solution does not change when increasing the mesh density (from medium to fine), as shown by the pressure histories at the tunnel walls. Therefore, the results presented from section 4.9.2 onwards have been obtained using the medium.

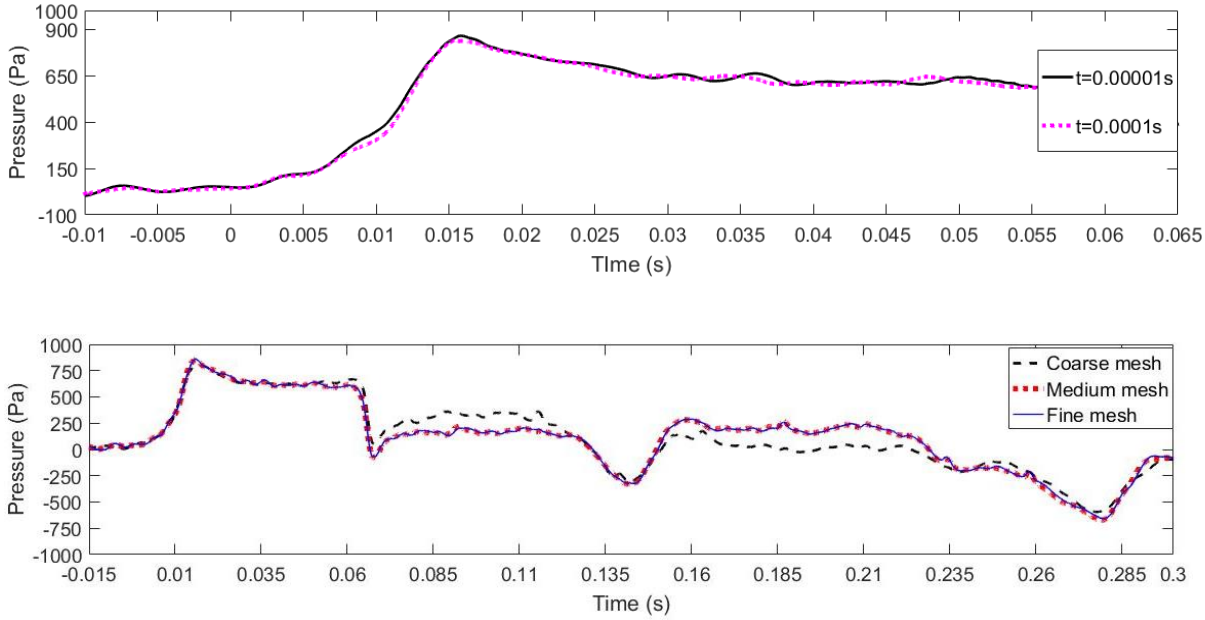

Figure 4.11: Timestep and grid independence for pressure-time histories recorded at 2 meters from the entrance.

4.9.2 **Pressure histories validation**

This section uses results from the physical tests in Chapter 5 to validate the numerical pressure histories. Figure 4.12 consists of three plots which represent the different monitored locations. For all three subplots, the time-base in the horizontal axis has been retained in its scaled form.

Tunnel walls

This part of model validation aims to show the accurate modelling of the pressure waves. This allows for an investigation of the pressure transients effects on the separation levels or velocity field inside the tunnel. Figure 4.12a shows the pressure

histories monitored at a fixed location, two meters from the entrance. Pressure starts increasing when the train approaches the tunnel and enters the tunnel (at t=0s). The first significant increase is observed by the compression wave generated by the nose entry, which travels towards the tunnel exit with the speed of sound. This is the highest amplitude among all pressure changes. The gradient of this initial compression wave is captured with 100% accuracy. The initial pressure wave amplitude is under predicted by 10% justified by dissimilarities in the train speed and potential differences in the blockage ratio. Regarding the former, due to the nature of the experiments, the results are ensemble averaged over 15 samples/runs with a maximum speed deflection of 1%. The latter can be explained by differences between the simplified underbodies of the two models which can affect the train cross-sectional area. The first significant pressure drop is caused by the train nose passing by the measurement point at approximately t=0.06s. The air is suctioned as the train approaches the measurement point and displaces the air. The negative peak is captured successfully indicating accurate modelling of the air suction.

For $t \geq 0.5s$, the pressure changes occur earlier in the numerical simulation. This inconsistency is explained by the speed difference between the two approaches, which influences the timing of the pressure waves. A speed reduction during this period could delay the tail entrance and the generation of the second pattern of pressure waves.

The pressure amplitudes reduce with time as the sound waves energy is dissipated by frictional effects. The numerical model confirms that the waves continue to reflect

at the two portals until the energy is dissipated, even after the train tail has exited the tunnel. This is caused by friction effects and emission of micro-pressure waves.

In summary, the numerical method adopted shows satisfactory agreement with experimental results for the pressure waves inside the tunnel. Therefore, this methodology can be successfully implemented to model the pressure transients inside the tunnel. In addition, compliance against current requirements for trains in tunnels can be checked, although this is not the focus of the current study. The TSI requirements are specified in terms of the maximum gradient and amplitude of the initial compression wave (TSI, 2014).

Nose, roof and side

Figure 4.12b and Figure 4.12c show the pressure histories at the locomotive surface, in open air and inside the tunnel. Pressure was monitored at P1, P2 and P3, which are located at the nose, roof and side of the locomotive surface respectively (see Figure 6.2 for an illustration of their location). P1 is located at the nose (middle height and centre of the track), while P2 is located at the highest point of the locomotive roof (on L7) and 3.4% of its length. The location of P3 is at the middle height of the locomotive (on L1) and at 14% of its length.

At P1, the positive pressure in open air is attributed to air stagnation (see t=-0.05 to t=0s in Figure 4.12b). At t=0s, the confined space of the tunnel and compression wave generated ahead of the nose cause the sudden pressure change. Pressure increases to approximately 1500Pa, which is captured with 97% accuracy by the

numerical model. In general, excellent agreement between experiments and CFD is found for this measurement point.

For P2 and P3, the open air pressure is negative at the roof and side of the locomotive, attributed to flow separation (see Figure 4.12b and Figure 4.12c). These two measurement points are located within the separated flow zone, between the separation and reattachment point. When the nose enters the confined space of the tunnel, P2 and P3 increase towards zero because of the instant interaction with the tunnel portal. This increase is recorded between t=0s to t=0.02s on the horizontal axis of the same figures. The most remarkable differences between experiments and CFD are observed for this time period. A potential explanation for this difference is geometrical differences at the tunnel portal. After this relatively instant phenomenon, pressure stabilises between t=0.02s and t=0.12s, where the separation length establishes. The pressures for this period are higher than the open air pressures which is explained by the change in the location of the reattachment point. More specific, across the separation length, pressure is almost minimum at the separation point and then increases as it approaches the reattachment point (Moussaed et al., 2014). Inside the tunnel, the separation bubble is shrunk and therefore P2 and P3 are closer to the reattachment point. This is translated to higher pressures at these monitored locations. As shown in Figure 4.12b and Figure 4.12c, the numerical model captures with satisfactory agreement the values of both P2 and P3 during this time period ($0.02s<t<0.012s$).

The disagreement between experiments and CFD is higher for P3 compared to P2, explained by the fact that P3 is closer to the underbody of the locomotive where

dissimilarities in the underbody of the two models exist. The speed difference can potentially explain part of this disagreement.

For all three measurement points, the results confirm previous findings that pressure is constant in open air but varies inside the tunnel (Vardy, 1996a). This has also been confirmed in Chapter 5 which showed that the pressure variations on the train surface are caused by the pressure waves. Although an in-depth analysis of the pressure field is out the scope of this study, the validation of pressures within the separation zone presented here, shows accurate modelling of the boundary layer phenomena. The agreement between the numerical model and experiments in Figure 4.12 validates the adopted method for this numerical study.

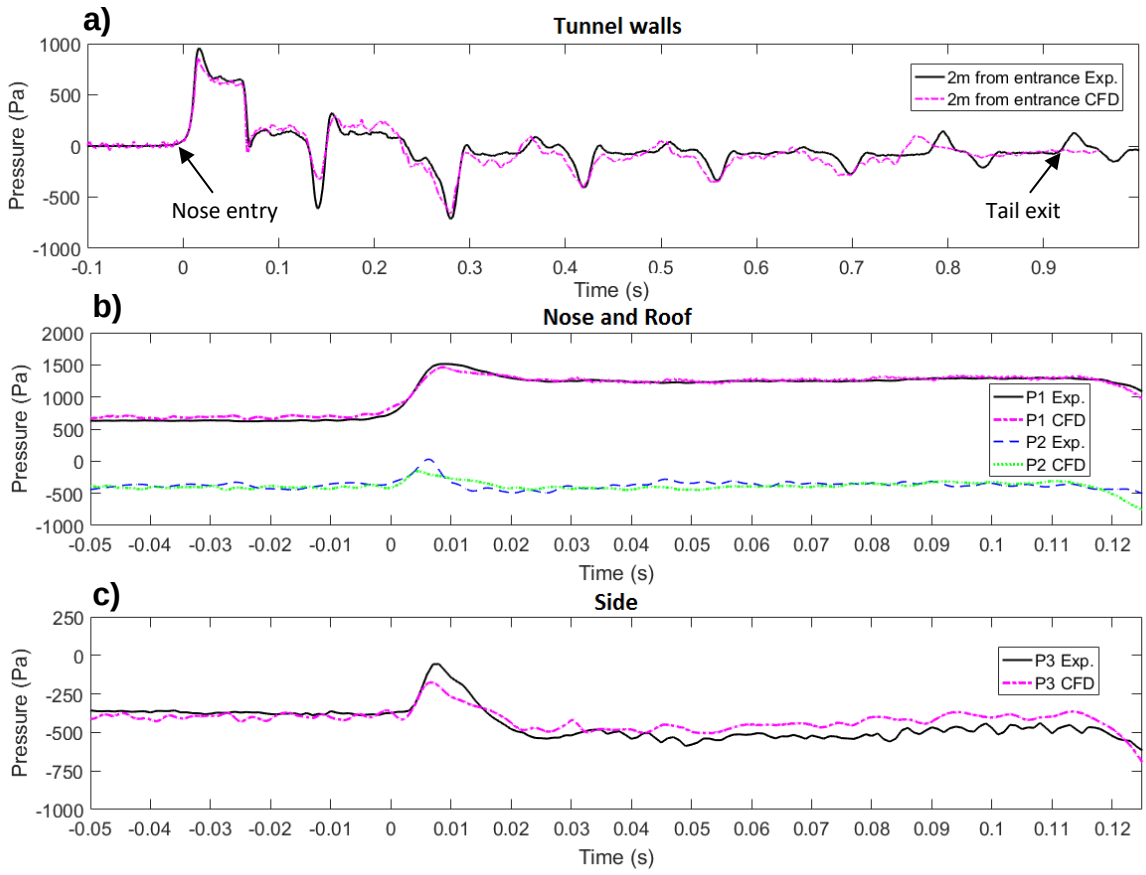

Figure 4.12: Validation of numerical model with experimental results. The nose enters the tunnel at t=0s; a) Tunnel walls - 2 meters from the entrance; b) Nose and roof of the locomotive; c) Side of the locomotive.

4.9.3 **Velocities around the train nose**

Figure 4.13 shows the validation of the numerical model with scaled experiments, taken from the slipstream study of Soper (2014). The instantaneous velocity was recorded at 0.09m and 0.07m (2.25m and 1.75m in full scale) from the ground and centre of the track respectively. In the numerical results, due to the size of the pre-entrance domain, the nose is located 3 meters away from the tunnel portal. On the other side, in the experimental measurements there is no tunnel ahead of the nose. This is the only difference between the measurement positions of the two methods. The longitudinal axis represents the distance from the train nose, which is positive towards the tail of the train, while the vertical axis shows the normalized velocity U_x/V. U_x is the longitudinal component of velocity and V is the train speed. Using U_x is common practice for slipstream studies(Temple and Johnson, 2008). The train model and facilities used for the experimental validation were given in Chapter 3 of this thesis.

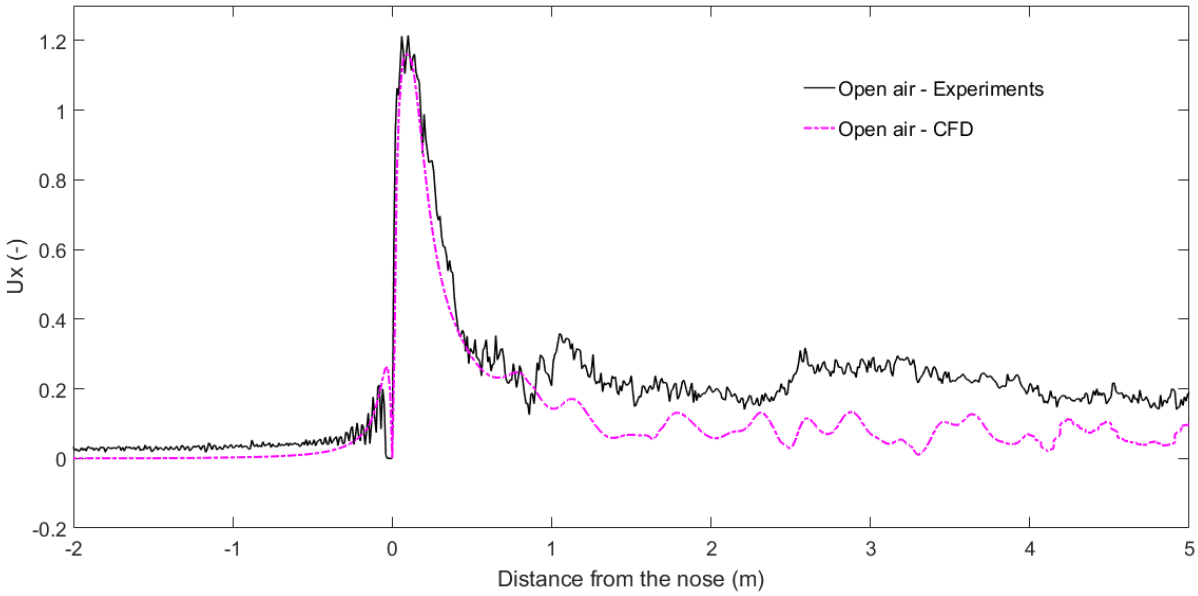

Figure 4.13: Comparison with experimental results (Soper, 2014). Normalized longitudinal velocity across different distances from the train nose. The negative horizontal axis is aligned with the direction of travel.

As mentioned in the literature review, the flow around the train is divided into the upstream, nose and boundary layer regions, taken from a previous open air analysis of Baker et al. (2001) (the near wake and far wake regions are not analysed in this section). In the upstream region (-ve side of the horizontal axis in Figure 4.13), the flow velocity is slightly higher than zero due to the displaced air ahead of the train and any differences between the two methods can be explained by the presence of tunnel entrance wall in the CFD model. In the experimental measurements, air is free to be move without facing any opposition from the presence of a tunnel portal. Potentially, this explains the fact that the first small peak ahead of the nose is under predicted by the numerical scheme. In the nose region, the peak magnitude is predicted accurately

by the CFD model with a difference of 4.5% while its gradient and length are captured with 100% accuracy. When moving further backwards, the level of agreement reduces near the boundary layer region. This can be potentially linked to differences between the two models in the underbody of the train, due to geometry simplification. Similar differences in this region were found in other CFD studies when comparing to experimental data (Flynn et al., 2014). The focus of this study is around the nose where the results are not affected by these simplifications. The prediction of the velocity peak at the nose is satisfactory to analyse the flow separation in this region and as such make this CFD model suitable for this study.

4.9.4 **Comparison to k-ε and DDES**

To validate the selection of the k-ω SST model, a comparison to k-ε and DDES is performed and then all together are compared to the experimental results from case 1. The comparison is conducted at three flow regions:

i. At the sides of the train, 0.09m and 0.07m from the ground and centre of the track respectively (2.25m and 1.75m in full scale), using the longitudinal component of velocity (see Figure 4.14)
ii. At the centroid of the train nose using the pressure-time histories from a moving measurement point (see Figure 4.15)
iii. At the tunnel walls, using the pressure-time histories from a stationary point 2 meters from the entrance (see Figure 4.16)

The DDES results have been taken from the study of Flynn et al. (2014) who simulated a Class 66 locomotive connected to fully-loaded container wagons, identical to the model used in this thesis. This study focused on analysing the open air slipstream, therefore DDES data are only available for flow region i. (see Figure 4.14). In this flow region, the most distinguishable characteristic of the slipstream is the nose peak, which is calculated with 98%, 95% and 63.2 accuracy by k-ω SST, DDES and k-ε respectively. The comparison shows clearly that k-ω SST is the most suitable model for predicting slipstream. This is linked to its ability to predict separated flow, which affects the velocity magnitudes around the train nose. The most distinguishable characteristic of the slipstream is the nose peak, where k-ω SST calculates it with 98% accuracy while k-ε with 63.2%.

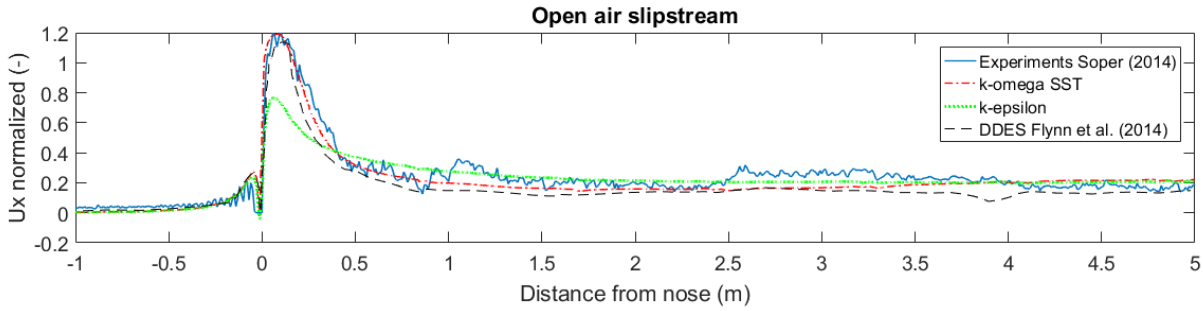

Figure 4.14: Normalised velocity in open air, recorded at 0.09m and 0.07m from the ground and centre of the track respectively. Comparison between k-ω SST, k-ε, DDES and experiments

Figure 4.15 presents the pressure-time histories at flow region ii (point P1). P1 is located at the front part of the nose, which is a region of air stagnation and enters the tunnel at time 0s, which is when the highest pressure change is triggered. This

pressure rise is captured with 97% accuracy by the k-ω SST model and 85.2% accuracy by the k-ε model, compared to experiments. Thus, this proves that k-ω SST is a better choice not only for areas of unsteady flow separation but also for this steady flow region.

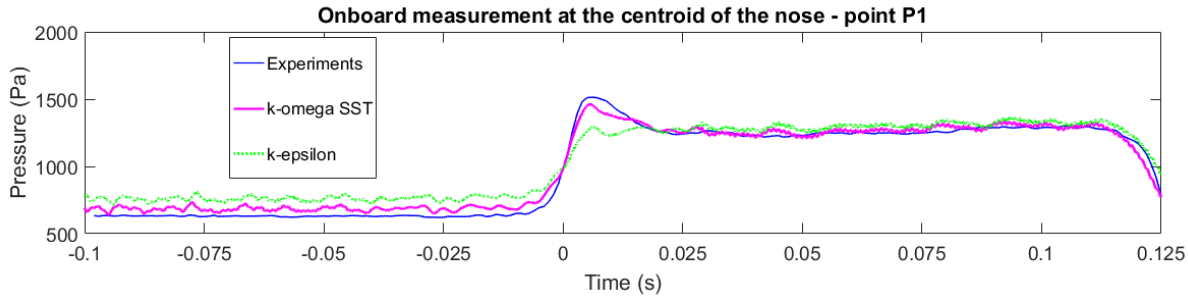

Figure 4.15: Pressure-time histories at the moving point P1, located at the centroid of the locomotive nose. Comparison between k-ω SST, k-ε and experiments

Figure 4.16 presents the pressure histories for flow region iii. At t=0s, the train enters the tunnel and generates a compression wave. When it passes by the measurement point, it causes the initial pressure increase. k-ω SST captures the one-part gradient pressure gradient found in the experiments, but k-ε estimates a gradient which approaches that of passenger trains (divided into two parts). This is attributed to the inability of the k-ε to predict the correct size of separation bubble around the nose. In terms of the wave amplitude, k-ω SST predicts the maximum pressure rise with 90% accuracy, while k-ε with only 70%. This confirms the selection of k-ω SST for all

numerical cases. All results presented in the remaining of this thesis have been obtained using k-ω SST.

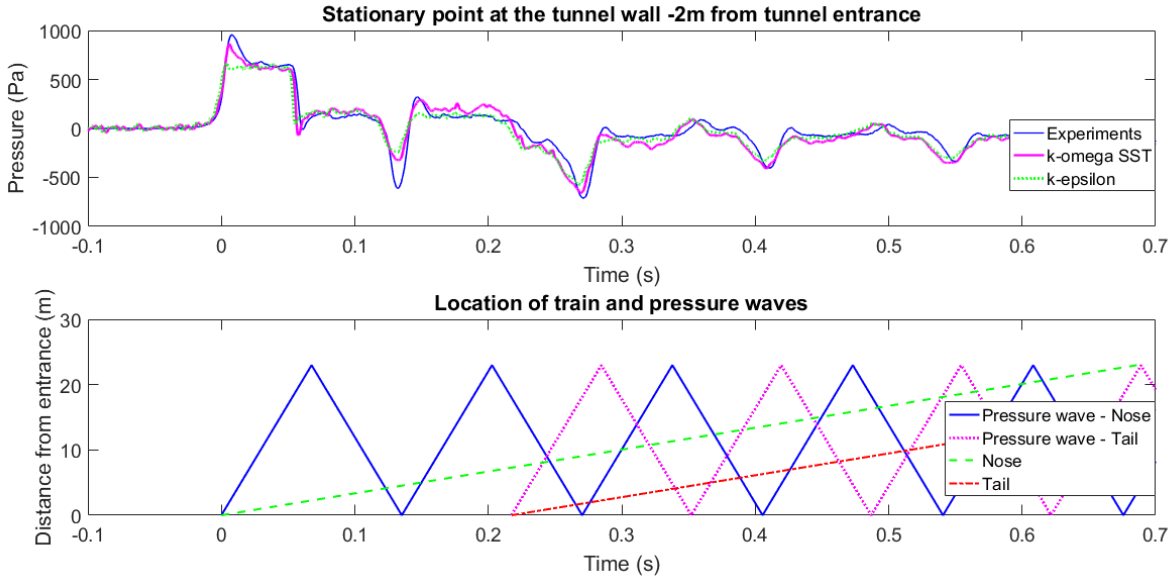

Figure 4.16: Comparison between k-ω SST, k-ε and experiments; Top: Pressure histories at the tunnel walls, 2 meters from the tunnel entrance; Bottom: Location of train nose and tail and pressure waves triggered by their entry into the tunnel.

Chapter 5

Model-scale experimental results and discussion

The majority of sections 5.1, 5.3.1, 5.3.2, 5.4.1, 5.4.3, 5.4.4, 5.5.2 and 5.5.3 has been published elsewhere, see Iliadis et al. (2018). The author of this thesis is the first author of the published article.

5.1 Introduction

This chapter presents a detailed discussion of the experimental investigation of pressure time histories on the tunnel walls, entrance portal and locomotive surface using moving model tests (see Chapter 3 for setup details). The effects of train length and loading configuration are presented, as well as the compliance of the current

train-tunnel case with regulations. The results from cases 1-3 below are presented in this chapter:

1. A Class 66 locomotive connected to 4 fully loaded container wagons where pressure is recorded at the tunnels walls, train surface, at the entrance wall. The data aims to illustrate the maximum pressure changes occurring at the tunnel walls, and the exact pressure forces experienced by the train. Additional measurements at the entrance of the tunnel show important information for tunnel and train design, as well as investigating the compliance of freight trains operation with current regulations for tunnels.
2. The effect of train length on the tunnel pressure histories is investigated using an 8-wagon train. The length is believed to influence a number of flow effects such as the interaction between the pressure waves with each other, the emission of micro-pressure waves (and thus the attenuation of the sound waves) and the flow at the tunnel portal.
3. The extreme case of 33% loading is tested. A previous study by Soper, Baker and Sterling (2014) has shown that the flow around the train in open air conditions (slipstream) is significantly influenced by different loading configurations.

A detailed analysis of the above is presented in the following sections. The time-pressure histories are presented in terms of the train location in the tunnel. The nose enters the tunnel at time 0s with a speed of 33.5m/s followed by a speed reduction due to drag and friction. The speed is measured at the boundaries of the entrance and exit of the tunnel, thus a linear speed decrease is assumed between the two

locations. All data presented in this chapter, is in scaled time-base, unless stated otherwise for comparison purposes. Multiplying the time-base of the presented results by 25 gives the full-scale values.

5.2 Ensemble average

Averaging of the results is performed because of the turbulent nature of the flow. For the tunnel and entrance walls, 3 runs are required to obtain stable results. For the on-board pressure measurements, a minimum of 15 runs is needed, as suggested in the study of Dorigatti (2013).

Appendix D presents a complete analysis on the repeatability of results, justifying the number of runs required for ensemble average.

5.3 On-board measurements

5.3.1 Nose of the train

The data on the nose of locomotive presents no significant variation between different pressure taps over this area. Thus, only two of the nose measurements points are presented in this set of data. The flow at this region is steady and inviscid, which is evident from the lack of pressure fluctuations (see Figure 5.1). This is in contrast with the roof and side data where fluctuations are large due to turbulence and separated flow. The pre-tunnel pressure at the front of the train (nose) is positive due to the flow

stagnation. Pressure increases as the air is brought at rest at the wall. The air particles escape to the sides, roof and bottom of the train. During entry, the nose pushes the air inside the tunnel and generates the compression wave where the nose experiences pressures as high as 1500Pa. Decreased pressure values occur in this area only when in contact with the expansive waves. The waves become weaker after every reflection and consequently the highest pressure drop occurs with E1. In contrast to the tunnel wall data, the on-board pressure returns back to its pre-tunnel value exactly after exiting the tunnel. The pressure waves inside the tunnel do not stop until they attenuate to rest. The highest pressure amplitudes are found at the nose of the train, remaining in the positive axis. The most important parameters influencing the flow on the locomotive surface are the propagation of pressure waves inside the tunnel, their interaction with the train, and the interaction of the train with the entrance and exit portals. These phenomena can be effectively identified on Figure 5.1 by plotting the location of the train and the pressure waves. The diagram illustrates the location of the nose and tail in relation to the tunnel length. The first pressure waves reach the tunnel exit faster than the train, as they travel with the speed of sound. The first pressure wave is compressive and changes sign (from compressive to expansive and vice versa) after every reflection. Similarly, the expansive wave, due to tail entry, also changes its sign after every reflection.

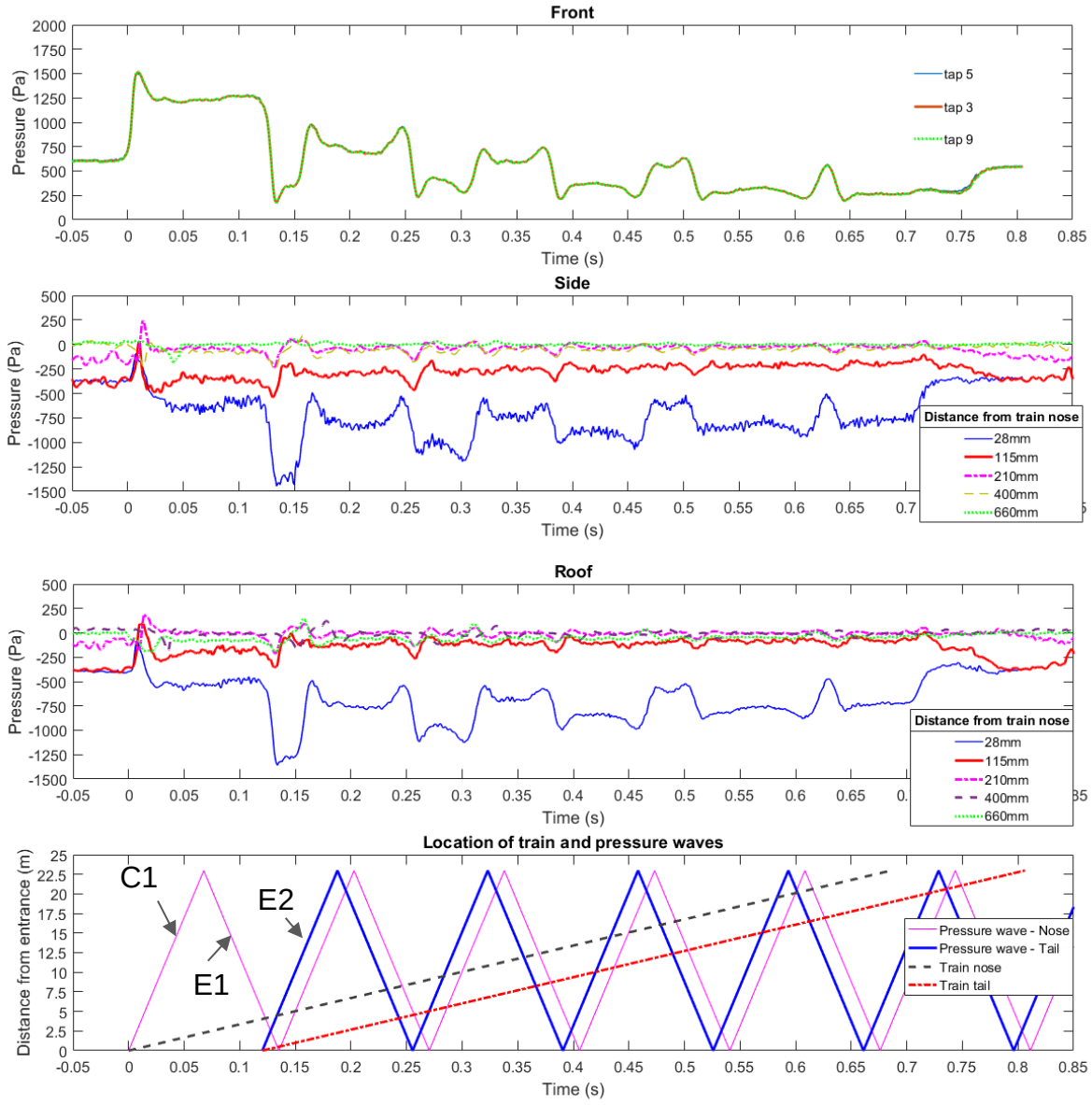

Figure 5.1: Pressure data on the moving surface of the locomotive connected to 4 wagons in relation to the location of the train nose, train tail and the pressure waves generated as a result of the nose and tail entry. The nose enters the tunnel at time 0s.

5.3.2 **Roof and sides of the train**

In contrast to the nose of the train, the pre-tunnel pressure over the roof is negative because of the reversed flow in the region (see Figure 5.1). When the flow is diverted at the train nose, an adverse pressure gradient leads to flow separation. The slow air particles near the wall do not have enough inertia to overcome this opposing pressure gradient while the fast-moving particles away from the wall are more resistant. The near wall particles move backwards (reverse flow), creating a shear between the inner and outer layers. The shear rolls to form a vortex, leading to flow separation followed by a stagnant air region. Then, the particles curve back to the surface to form a reverse flow region. This region is called the separation bubble, and is represented by the plotted data at the nearest points to the nose (28 mm). As we move further away from the nose, the reattachment negative values show the reattached flow. No significant effects of the flow separation are found in the last two taps (400 & 660mm). Moving on now to consider the flow in the confined space, the first observations arise when the nose passes the portal. The near-nose area experiences an increase in pressure followed by a sudden drop, which could be linked to a change in the nature of the separation bubble. There is experimental evidence that the bubble increases the effective blockage area and the train entry affects the length and height of the bubble. It is also believed that the jet towards the tunnel portal affects the flow at the roof and sides. As highlighted in the literature, the air near the nose is displaced during entry and travels towards the tunnel portal, experiencing friction effects both from the train and the tunnel. The amount of the displaced air depends on the

blockage ratio and another set of parameters such as speed and nose shape. Auvity and Bellenoue (1998) have shown that the shear layers of this exiting jet form a vortex which stops only when the tail is inside the tunnel.

Figure 5.1 illustrates that the meeting of the train with E2 causes a pressure drop. This drop is sharp for the near nose points but smoother for the rest of the taps. Then all taps experience rises and drops when in contact with the compression and expansion waves respectively. As mentioned earlier, these effects become weaker due to the attenuation of the pressure waves. In general, the highest pressure changes are observed for the measurement points near the nose. For the majority of the data, the pressure around the locomotive is negative, indicating separated flow. When comparing the roof to the sides of the train, the pressure histories are identical. The most noticeable differences are found at 115mm from the train nose, where the flow over the roof is affected to a greater extent when it enters the tunnel.

5.4 Stationary points along the tunnel wall

5.4.1 Pressure histories

The tunnel wall data can be used for accessing the train's compliance with current regulations. As shown in Figure 5.2, pressure starts increasing slightly before the train's entry. When the nose enters, the air particles ahead of the train are pushed and a compressive wave forms. As the wave front passes from each measurement

point, pressure increases. The amplitude of C1 is the same for all measurement points along the length of the tunnel. The maximum amplitude is approximately 1000Pa which is below the 3000Pa maximum limit for trains operating below 69.4m/s (TSI, 2014). For the fully loaded cases, C1 produces the highest pressure increase in the tunnel. As a general observation, an increase is observed whenever a compression wave (high pressure) or the tail of the train passes from a measurement point. Attention must be paid when these two occur at the same time, as it can result in large pressure changes. When the tail of the train passes from the measurement point the cross-section area at the measurement position increases and velocity reduces. On the other side, a pressure drop is observed when an expansion wave or the nose of the train passes from a measurement point. As the nose approaches, the flow in front of the train pushes the air away from the measurement point and pressure drops due to suction. At 2m away from the entrance, the initial pressure increase from C1 is followed by a small drop as the wave travels towards the exit. Then a further drop occurs when then train nose passes from the measurement point, followed by a third drop when the reflected pressure wave returns back as an expansion wave. The tail entering the tunnel generates an expansion wave which passes from the measurement point, decreasing the pressure even further. At 4m, the latter 2 drops take place at the same time as the nose and the tail expansion waves meet each other, resulting in the highest pressure drop of approximately 1000Pa. There would therefore seem to be a definite need to pay attention to combined pressure changes occurring the same time, affected by the train and tunnel length, as well as the train speed. The pressure waves meet each other at several occasions

inside the tunnel. When having the same sign, constructive interference occurs where the pulses overlap and create a higher instantaneous amplitude of pressure, continuing in their direction of travel. When having opposite signs, they cancel each other and then recede. In both cases, some energy can be lost during this process. This lost energy contributes to the attenuation of the pressure waves, where their amplitudes reduce. Other factors include the thermal consumption of energy due to viscosity, which reduces the acoustic energy and the radiation of the micro-pressure waves which transmit part of the pressure waves' energy out of the tunnel.

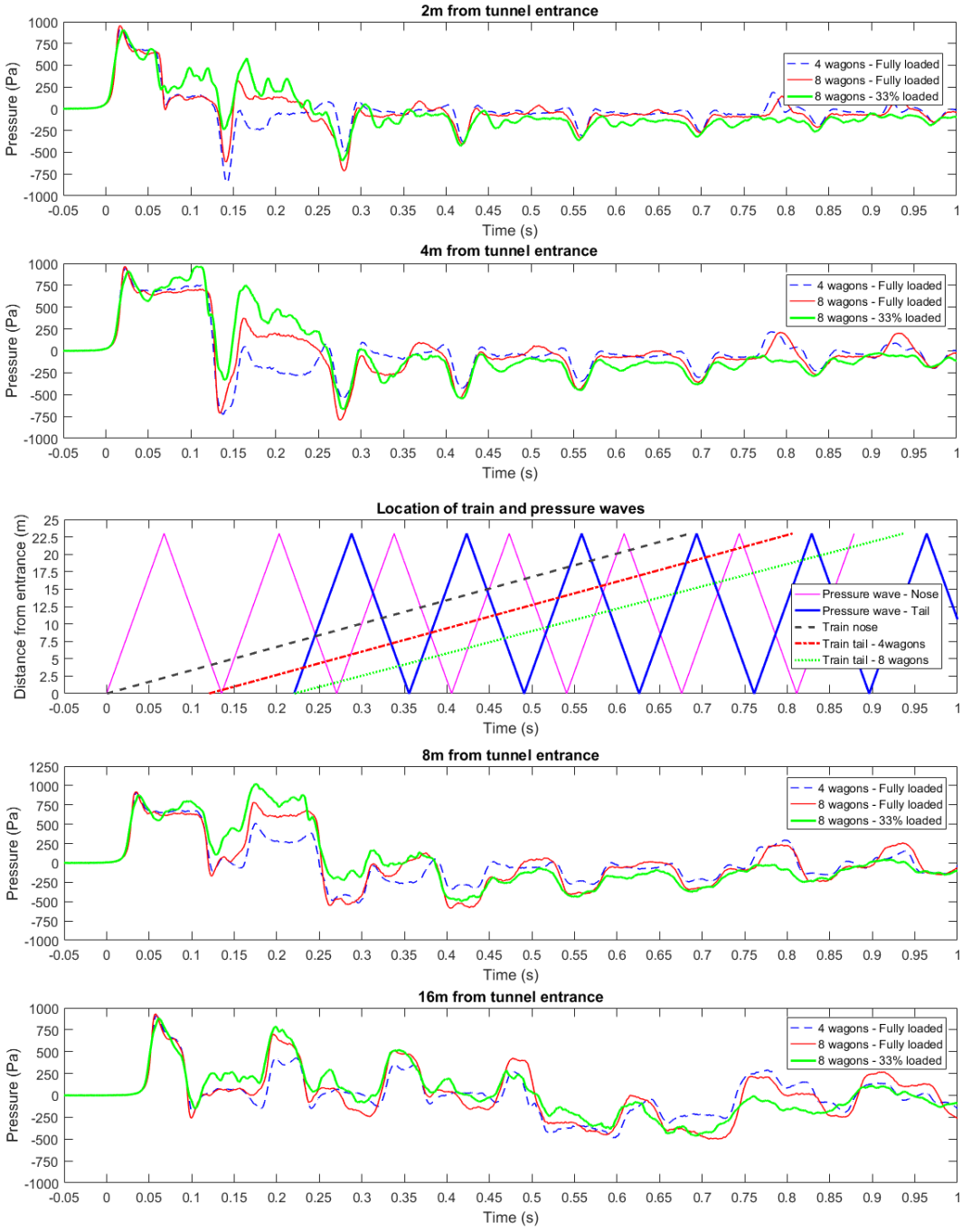

Figure 5.2: Pressure data along the tunnel surface (Stationary points). 4 fully loaded, 8 fully loaded and 8 partially loaded wagons are presented. The nose enters the tunnel at time 0s.

These attenuations are expected to be more significant at full-scale scale due to higher viscous stresses at the walls of the tunnel (Woods and Pope, 1981). The reflection of the pressure waves continue even after the train tail exits the tunnel and the time period of this phenomenon depends on the train speed, blockage ratio, nose shape and train and tunnel length which influence the amplitude of C1.

On Figure 5.2, when comparing measurement points 2m and 16m from the entrance, it can be concluded that the closer to the entrance the higher its amplitude of the initial wave. This is potentially explained by the skin friction experienced by the wave as it travels towards the exit. Similar reductions in amplitude have been observed by the experimental study of Vardy (1996a) (see Figure 5.3) which shows that the highest pressure occurs near the train nose.

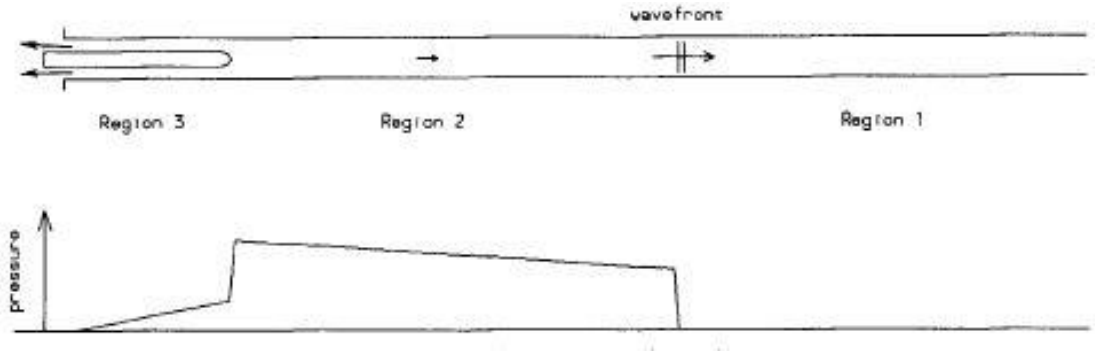

Figure 5.3: Pressure distribution inside the tunnel, showing the development of the initial compression wave (Vardy, 1996a)

5.4.2 **Effect of train length on the tunnel walls**

Figure 5.2 compares pressure histories at the tunnel walls for different train lengths. No effects are observed on the development of the initial compression wave C1. Its amplitude and gradient remain unchanged, as the train nose entry is independent of the total length. This justifies the fact that analytical models for the prediction of C1 do not account for the train length.

Post the development of C1 the first differences are observed when the tail of the 4 wagon train enters and triggers the tail expansion wave E2. Near the tunnel entrance, E1 interferes with E2. The interference affects more the neighbouring measurement points (2m from entrance) at approximately t=0.145s. For both train lengths, this is the lowest pressure inside the tunnel, although it is significantly lower for the 4 wagon train. This phenomenon proves that the lowest pressure inside the tunnel depends on the train length, as the timing of the pressure waves changes and can cause interference of waves.

The time and location of waves' interference is shown in the middle plot of Figure 5.2 and can be predicted in advance.

5.4.3 **Effect of loading on the tunnel walls**

The gaps in the partially loaded wagons cause separation. This is in contrast with the fully loaded case where the flow follows the surface of the wagons (although there are small gaps between cars) and the blocked cross-sectional area is almost constant. As

shown in Figure 5.2, for the 33% loaded case, intense pressure changes are monitored at stationary points in the time period between the rear part of the locomotive and train tail passage. Fluctuations are recorded, due to the complex flow pattern. These fluctuations can generate a pressure amplitude which is slightly higher than the pressure increase from C1. More specific, at 4m and 8m away from the entrance, a second peak is observed, having higher amplitude of C1. This is contradictory to all results from previous research conducted on fully loaded trains, which suggest that the highest pressure amplitude occurs at C1. This peak occurs before the nose passes from the measurement point (see Figure 5.2). For the same time period, the fully loaded case presents constant pressure and a smoother backward transition of the flow to the rear cars. As the main focus of analytical models is to predict the highest amplitude in the tunnel by modelling C1, this study suggests that analytical models are not used for partially loaded trains.

5.4.4 **Comparison to passenger trains**

The passenger train results presented in this chapter have been taken from the paper of Rety and Gregoire (2002) and adapted for a dimensionless comparison. The TGV-R train has a streamlined nose which is a good representative of passenger trains. The comparison focuses on the initial compression wave because the train nose affects its shape. The occurrence of the remaining pressure waves depend on the train length, which is not same for the two cases. For comparison purposes, both sets of data were normalized in terms of the train speed, distance from the portal and

model-scale. The pressure coefficient has been calculated using equation (22) based on the train speed. The time base of the scaled model has been converted to full scale. Then both sets of data were normalized using equation (23). Therefore, the results below are blockage ratio dependent.

$$C_p = \frac{P}{\frac{1}{2}\,\rho\, V^2} \tag{22}$$

$$t^* = \frac{t}{l.\mathrm{a}} \tag{23}$$

As shown in Figure 5.4, the two trains cause an identical pressure increase inside the tunnel prior to entry. When the passenger train enters the tunnel, the front part of the nose causes the formation of initial compression wave with a certain pressure gradient. Then, the remaining of the nose length enters the tunnel and the gradual change in the geometry smooths the gradient of the wave. Pressure rises with a certain gradient, and then reduces due to friction effects when the main body enters the tunnel. As found in the study of Choi and Kim (2014), by changing the nose shape from blunt to streamlined, the nose length increases and the train's front cross sectional area reduces as well as the blockage ratio. As a result, pressure drag is lower, in contrast with viscous drag which remained the same. The blunt nose of the Class 66 locomotive causes a pressure rise with constant gradient which is significantly steeper. The geometry changes by almost 90° which is similar to a square cube. The absence of the second gradient can be explained by the nose shape which is not elongated (to act as a smooth transition zone).

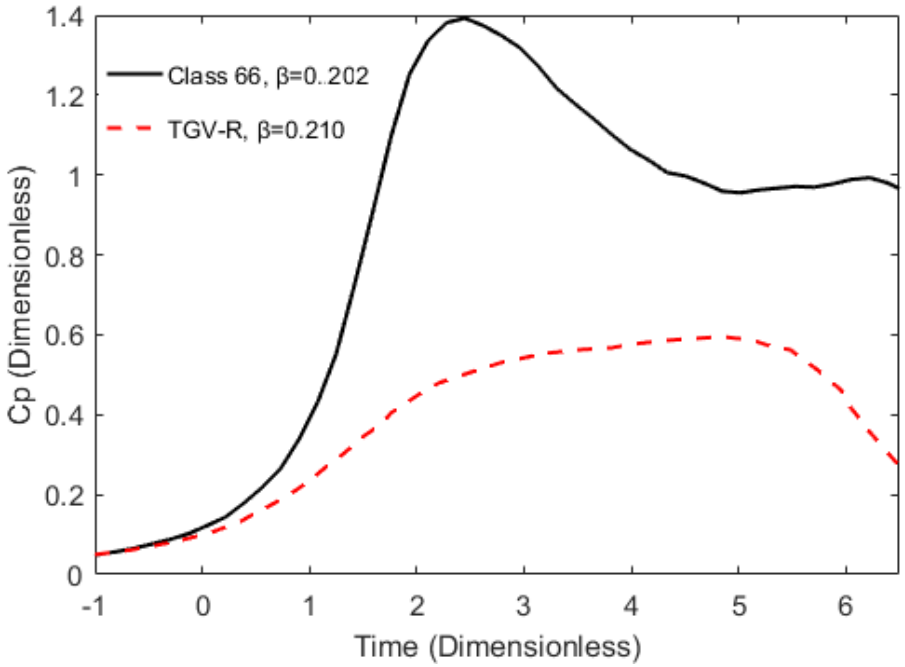

Figure 5.4: Initial compression wave compared to full-scale experimental data from (Rety and Gregoire, 2002) of a TGV-R into the Villejust tunnel.

The freight train causes a larger pressure rise, which is attributed to the nose shape. According to Vardy and Reinke (1999), stagnation losses at the train nose and tail are primary sources of drag for trains in tunnels, and a relationship between the nose coefficient k_N and blockage ratio β was hypothesized. The same study showed that the value of k_N for a freight train can be as high as 0.01 while for a passenger train it can be as low as 0.003. The difference in the two amplitudes is approximately 80%, which indicates strong effects of the blunt nose. The blockage ratio of TGV-R is slightly larger and the difference would be expected to be even higher if the two trains had the same ratio.

5.4.5 **Attenuation of pressure waves**

As mentioned before, the waves' amplitude reduces with time and distance travelled. This phenomenon is known as acoustic attenuation, attributed to two main sources; scattering and absorption (NDT, nd). Scattering is related to the energy lost during the reflection of the sound wave. This occurs at the tunnel boundaries, affected by the intensity of the micro-pressure waves. Absorption is related to the energy converted to other forms because of thermal consumption of energy caused by viscosity effects. Viscosity effects are believed to be lower for scaled trains due to smaller surfaces, causing less intense attenuations.

In general, acoustic attenuation can be modelled, accounting for the losses as a rate of amplitude reduction per distance travelled by the sound wave. For example, Stoke's law of acoustic attenuation calculates this reduction rate which is a consequence of viscosity effects for plane waves. However, such an analysis would require the amplitude of the pressure waves after exit to be known. Although such calculations provide useful information, such an investigation is outside of the scope of this study.

Figure 5.5 below shows the pressure histories at the tunnel walls, 4 meters from the entrance. The timescale in the horizontal axis is in its original form (scaled). Unlike the previously presented figures, this graph includes the pressure histories after the tail exit. The lower part of the graph shows the location of the pressure waves inside the tunnel.

It is evident that even when the train is outside of the tunnel, the sound waves continue to reflect. This phenomenon can be of interest if two trains pass through a tunnel in the same direction, with a small time difference. It is unknown what the impact of the pressure waves caused by the first train would be on the second.

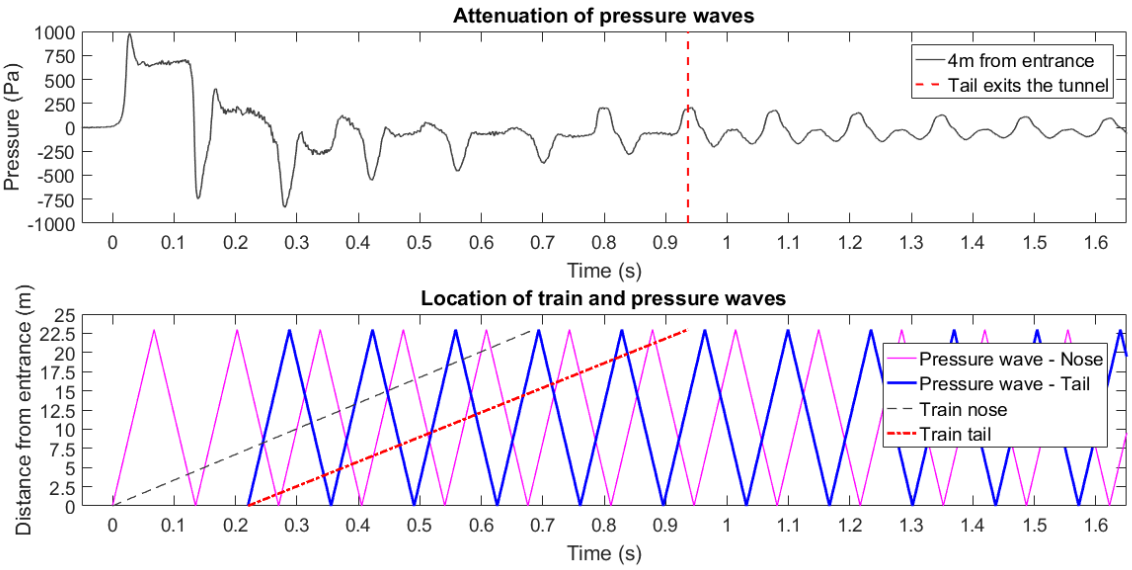

Figure 5.5: Pressure measurement before and after the train exits the tunnel, showing the attenuation of the pressure waves

5.4.6 **Variation of pressure in the radial direction**

Figure 5.6 shows pressures for 3 taps along the radial direction, separated by 90° from each other. There are no remarkable variations in pressure, which confirms that the pressure waves are planar. The compression wave has the same gradient and amplitude for the three locations. Negligible differences are found between the

instants that the train nose and tail pass by the measurement point. This is explained by the axisymmetric shape of the train which results in uneven distances from the tunnel walls, between the sides and roof.

The overall conclusion drawn from this analysis is that the radial position of the taps does not affect the results and sensors can be placed at the most convenient locations. When multiple sensors are fitted in the radial direction, averaging of pressures is recommended. For the purposes of this study, the 3 readings along the measurement ring have been averaged.

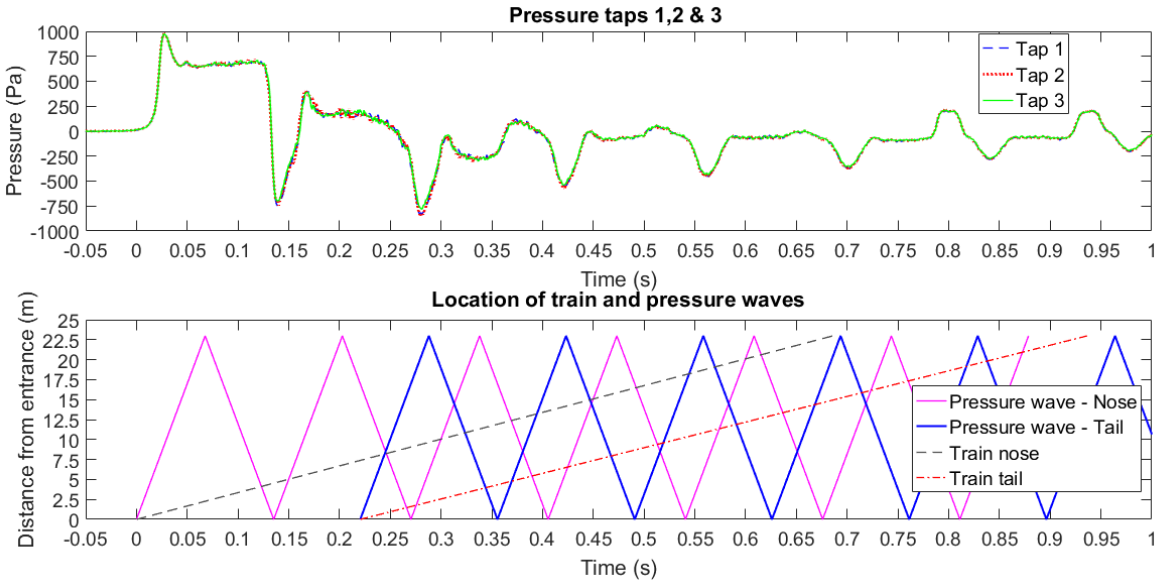

Figure 5.6: Variation of pressure in the radial direction (at the tunnel walls). All 3 pressure taps are located 4 meters from the entrance

5.5 Entrance wall

5.5.1 3D effects on the entrance wall

Measuring pressures at both sides of the track at the tunnel portal wall can detect the presence of any 3D effects. Each pressure tap is compared to its equivalent point at the other side, at equal distance from the centre of the track. The measuring positions are divided into the lower and upper points. The position of the pressure taps is illustrated in Figure 3.14 and the pressure results in Figure 5.7. All results have been obtained using the 4 wagon fully loaded model. On Figure 5.7, the train head enters the tunnel and passes by the measurement points at t=0s. Positive pressure changes are detected at the wall prior to entry as air is pushed by the train head causing stagnation at the wall. This is the maximum positive pressure change in the plot, as the remaining pressure histories are on the negative axis.

When comparing the two sides of the track, for the lower measurement points, the most significant differences between them are observed between t=0s and t=0.225s, when the nose and tail enter respectively. The maximum pressure changes and most remarkable 3D effects occur during this time period. Due to the fact that the lower measurement points are located near the underbody of the train, the pressure changes are believed to be related to the air displaced by this part of the train.

For the upper measurement points P2, P4, P9 and P11 longer duration of 3D effects is observed, linked to the upper half of the train. P4 and P9 have the most remarkable

difference between them. This is justified by the 3D vortex around the train which exits from the upper part of the tunnel.

When the whole train is inside the tunnel, the most remarkable pressure changes arise from the arrival of the waves at the portal during reflection, but these do not show three-dimensionality.

The above observations suggest that when investigating maximum pressure changes at the entrance wall, both sides need to be studied. However, the differences between the two sides do not change the interpretation of results. For the remaining of the analysis, only the right-hand side of the wall is analysed.

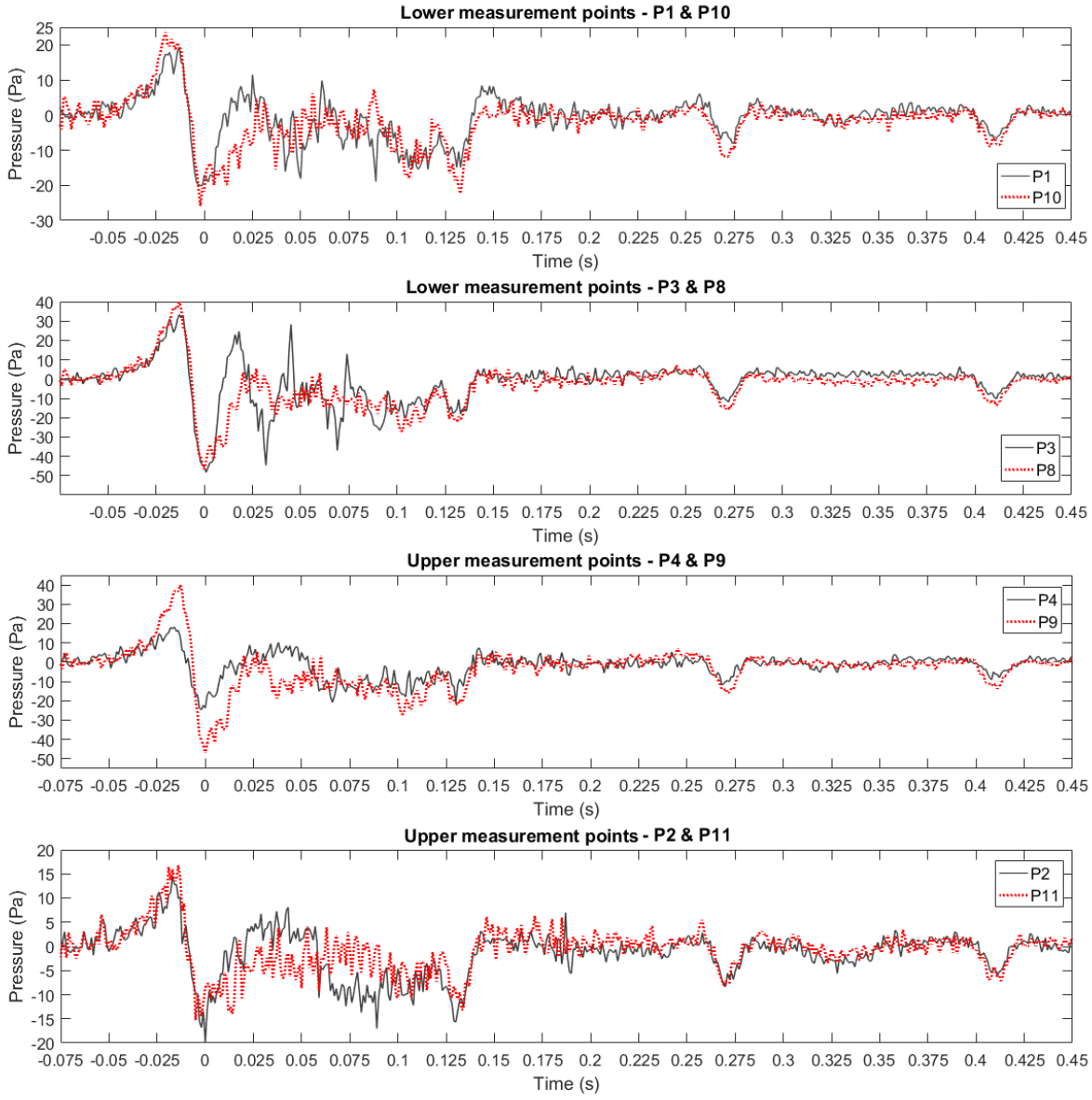

Figure 5.7: Comparison between the two sides of the entrance wall

5.5.2 **Pressure at the entrance wall**

Figure 5.8 presents the time-pressure histories at the entrance wall. The most significant effects are observed in the time period -0.025s < t < 0.225s, when the nose approaches the entrance wall and until the tail enters the tunnel. Apart from this period of time, the only important effect observed is the pressure changes due to the arrival of the compressive and expansive waves at the entrance, increasing and decreasing the monitored pressure respectively. In this section, only the fully loaded and partially loaded cases with 8 wagons are presented (see Figure 5.8).

As the train approaches the tunnel, the air ahead of the nose is displaced and the pressure at the tunnel entrance wall increases. The air travels towards the tunnel interior and the entrance wall. At the wall, it is brought at rest and a stagnation area forms. The highest pressure increase is observed at P6, which is located above the centre of the track, followed by the pressure increase at P3, which are the closest points to the sides. The lowest changes are found at the upper measurement points P2 and P4, where the maximum pressure increase is approximately 20Pa. When the train is near the portal, it starts displacing the air inside the tunnel. In contrast to the open air, the air cannot move freely to the atmosphere and therefore escapes from the portal in the form of a vortex. The vortex surrounds the entrance wall and the reversed flow in this region causes a reduction in pressure. This phenomenon becomes more intense as the nose approaches the entrance. The passing of the nose from the portal increases the pressure values at the entrance wall. The points nearer to the centre of the track P6 and P3 have a stronger pressure rise compared to

the rest of the points due to the displaced air around the roof and side of the train which diverts the exiting vortex from the tunnel.

When the tail passes from the tunnel entrance and the train is wholly inside the tunnel, the effects start to attenuate and the large fluctuations stop. Figure 5.8 illustrates that when the expansion waves arrive at the tunnel entrance, the pressure at the portal reduces. This process continues until the pressure waves in the tunnel are brought to rest. In the case that two pressure waves with the same sign (compressive or expansive) arrive at the tunnel entrance with a small time difference, pressure changes due to the first pressure wave and then remains unchanged at the arrival of the second wave.

The fluctuations between the nose and tail entry are more intense for the points on the side of the tunnel (P1, P2, P3, P4) and less significant for P5 and P6. P2 and P4 are the points which are furthest from the train surface, and therefore the effect of air displacement is less intense. Therefore, the exiting vortex is not significantly affected in this region, keeping pressure values on the negative axis. Apart from the distance from the centre of the track, other parameters which are believed to influence the pressure amplitude and gradient are the train speed, train cross-sectional area and the presence of any obstacles near the entrance (Zhang et al., 2017).

5.5.3 **Effect of loading on the entrance wall**

The pressure histories of the fully and partially loaded trains are presented in Figure 5.8. For the fully loaded case, the most important effects are observed during the

nose entry, but tend to stabilise afterwards, because of the continuous cross section area of the main body of the train. However, for the 33% loaded case, the geometry of the train varies between the nose and the tail, as some of the wagons do not have containers. As a result, significant pressure changes are observed until the tail enters the tunnel. Whenever, a loaded wagon passes from the entrance boundary, pressure increases due to the displaced air around the train diverting the vortex at the measurement points. On the other hand, whenever an empty wagon passes, less air is displaced.

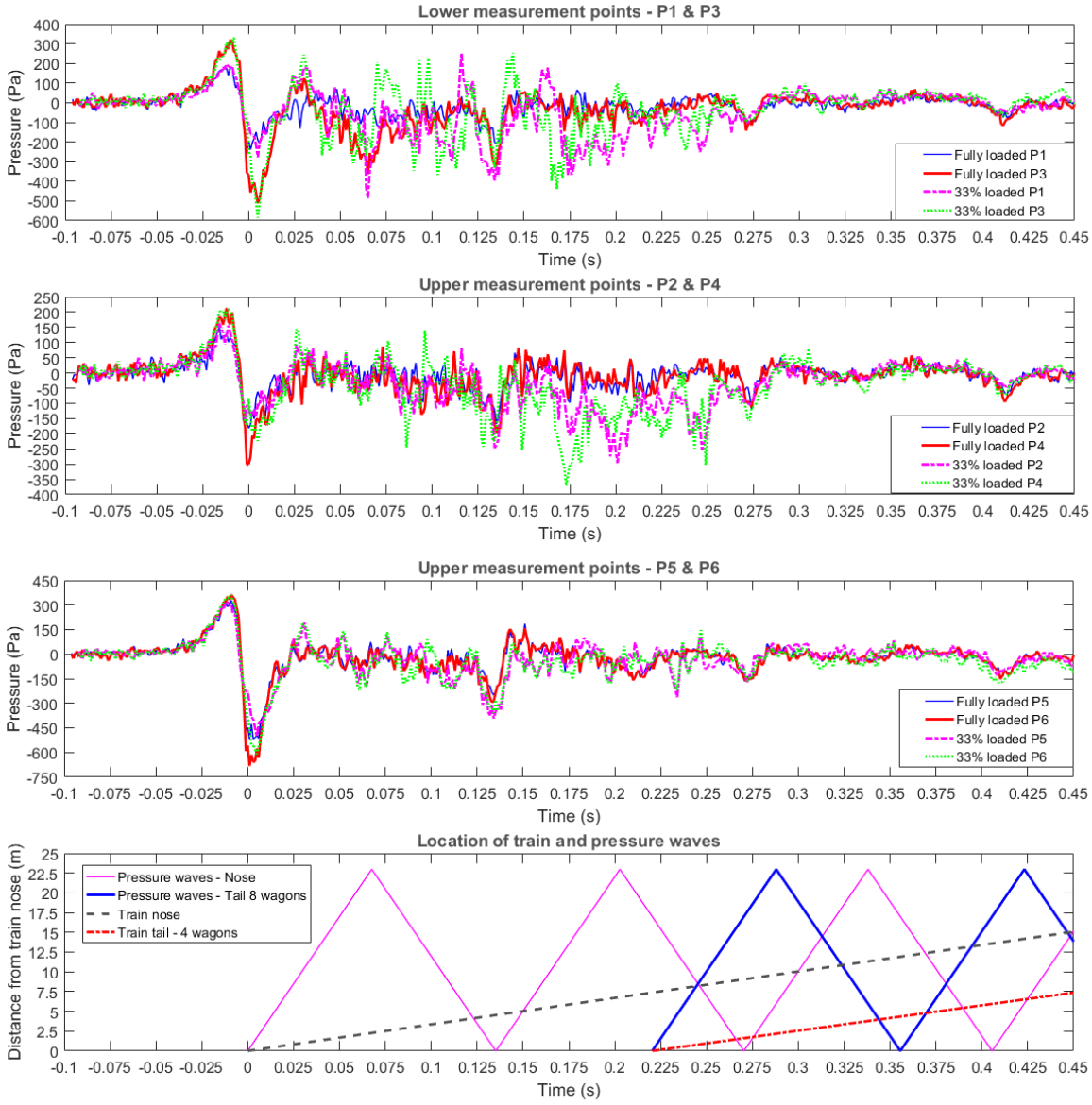

Figure 5.8: Pressure data at the portal wall. The locomotive is connected to 8 wagons (either fully loaded or partially loaded). The nose enters the tunnel at time 0s.

5.5.4 **Effect of train length on the entrance wall**

Figure 5.6 shows the pressure histories at the entrance walls with the fully loaded 4 and 8 wagon trains, referred to as short and long trains respectively. The most remarkable effects are observed for the lower measurement points P1 and P3, between the tail entry of the short and long trains. During this period, the short train pressure histories are more stable compared to the long train. This is justified by the fact that the short train is completely inside the tunnel, while part of the long train is still outside, displacing the air towards the entrance wall. Negligible effects are found for the upper measurement points. For both train lengths, after the tail entry pressure at the portal stabilizes near to zero and changes whenever a wave arrives.

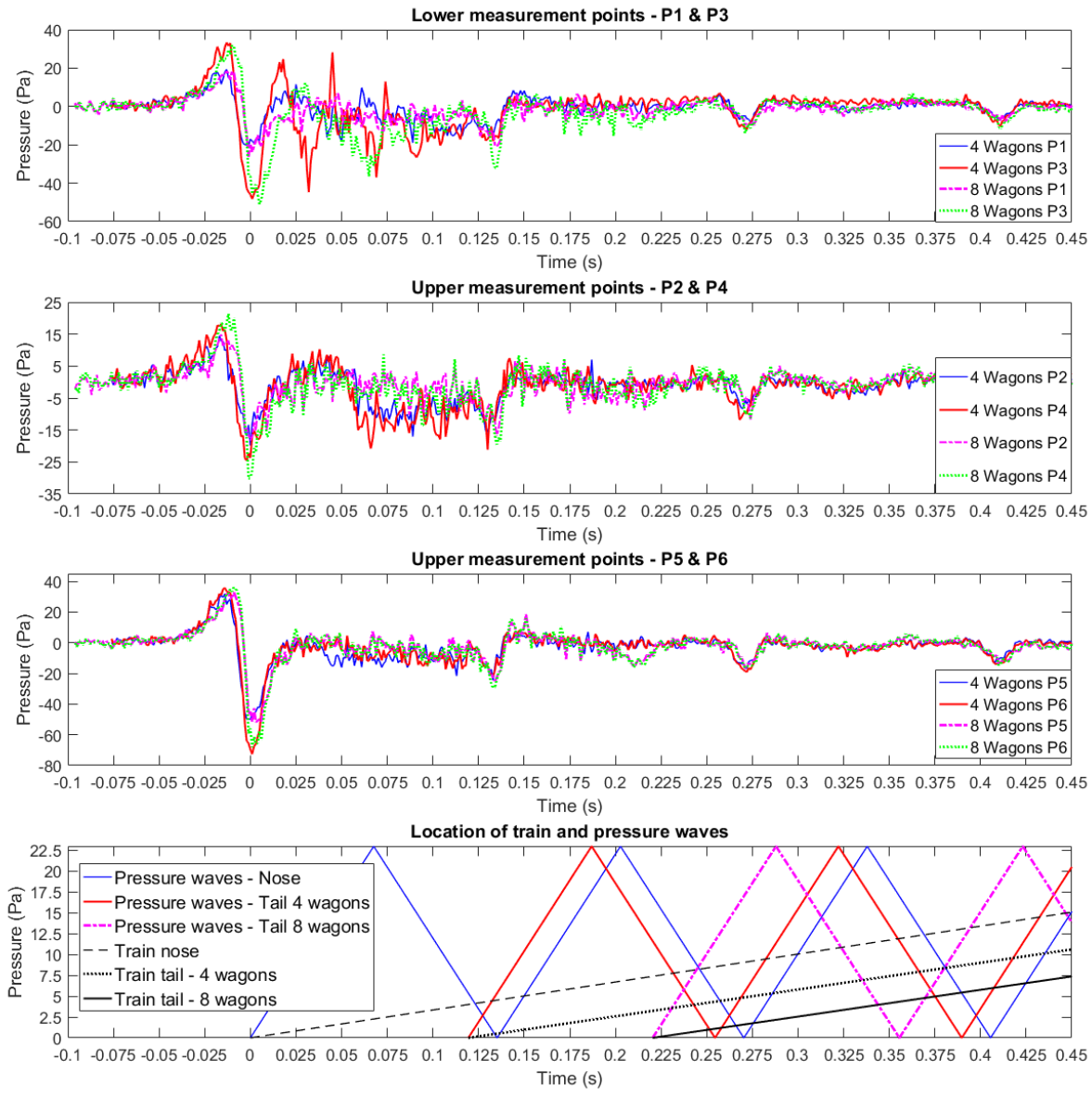

Figure 5.9: Effect of the train length on the pressures recorded at the tunnel entrance wall.

5.6 Methodological contributions

a) When measuring pressures at the tunnel walls, 3 runs are adequate for obtaining repeatability. At the surface of the train, the turbulent nature of the air around it makes it necessary to average over at least 15 runs.
b) To find the maximum pressures on the surface of the Class 66 locomotive, the pressure sensors should be placed at its front face.
c) The pressure waves are planar and a single pressure sensor at each longitudinal position in the tunnel is adequate.
d) For entrance wall measurements, the range of the sensors should be significantly lower than the tunnel wall sensors. The highest measurement range sensors should be placed on the front face of the locomotive, followed by the tunnel walls and entrance walls.
e) The on-board pressure measurements can be conducted for only ‘’one side of the locomotive, as negligible differences have been found between the left and right sides of the tunnel’’ (Iliadis et al., 2019, p. 9).

It must be noted that c) and e) are valid for axisymmetric cases only (single-track circular tunnel) of constant cross section area. In multiple track tunnels or tunnels with variable cross section areas, variations of the pressure wave amplitude and gradient would be expected along the vertical and lateral directions.

Chapter 6

Numerical results and discussion

The majority of sections 6.3.1 – 6.3.4, 6.4.2, 6.4.5 and 6.4.6 has been published elsewhere, see Iliadis et al. (2019). The author of this thesis is the first author of the published journal article.

6.1 Introduction

This chapter presents the results of cases 4-8 (see Figure 1.1) which investigate the pressure wave development and flow field around the train using CFD. The methodology for the current analysis is presented in Chapter 4.

The need for these simulations was derived from the experimental results (cases 1-3) which highlighted areas that require additional investigation and CFD was chosen as the most efficient method to achieve that. The bluff nature of the train and the need to

accurately capture the flow separation was the reason that it was chosen over 1-D analysis. CFD has the ability to produce full resolution results in areas not accessible through physical tests, provide detailed data inside the separation zones and implement geometric modifications.

The 3 main subsections in this chapter investigate 1) the pressure transients inside the tunnel, focusing on the effect of a number of parameters and providing additional data to the experimental cases; 2) the separation levels at the train head; 3) and the velocity field around the train.

6.2 Pressure transients

6.2.1 Compliance with current regulations

This section compares the pressure time histories at the tunnel walls for two train speeds, drawn from case 4 and its modified version with increased speed. Table 2.1 shows that the current regulation for the initial pressure rise is 1750Pa for the reference case, and both the 33.5m/s and 38.5m/s cases comply with this limit. This can be seen in Figure 6.1, which shows a maximum pressure increase of approximately 1100Pa, caused by the initial compression wave C1. After C1, the remaining of the graph is governed by the timing and location of the waves and train, which vary with train speed.

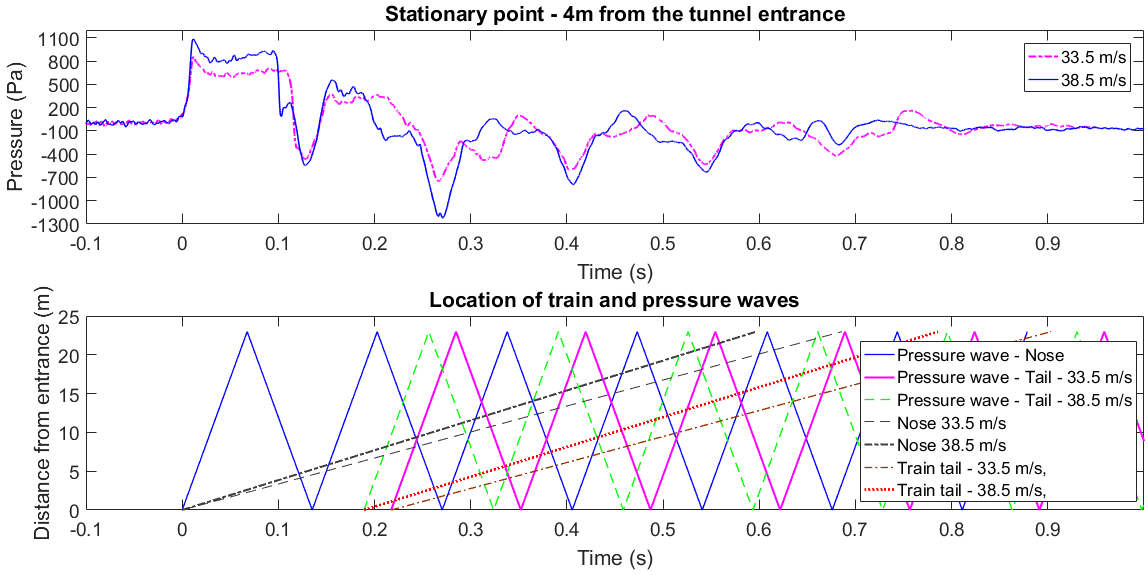

Figure 6.1: Effect of train speed; Top: Pressure histories recorded at stationary locations at the tunnel wall; Bottom: Location of train nose and tail as well as the pressure waves caused by their entry into the tunnel at t=0s

Figure 6.1 confirms that a potential increase of 5m/s for case 4 complies with regulations. All sections onwards use results from case 4 obtained at 33.5m/s and examine the development of pressure waves in detail, unravelling the causing mechanisms behind it.

6.2.2 **Effect of nose shape on pressure wave development**

The results from the Class 66 locomotive are compared to the 3 nose shapes shown in section 4.7 and Figure 4.7. Analysis of the results is conducted in three key flow regions:

i. Moving measurement point P1, located at the centroid of the nose (see section 6.2.2.1)

ii. Stationary measurement point at the tunnel walls, located 2 meters away from the tunnel entrance (see section 6.2.2.2)

6.2.2.1 Moving measurement point P1

The location of P1 can be seen in Figure 6.2. Figure 6.3 plots the pressure-time histories starting from open air, for the Class 66 nose and nose 1 and 2. Results from nose 3 were not available for this analysis. The train front enters the tunnel at t=0s and exits before 0.7s. In open air (-0.1s < t < 0s), no remarkable differences are shown for the three nose shapes plotted. However, after entry into the tunnel (see point A in Figure 6.3), the initial compression wave development is influenced significantly by the nose shape.

The transition between blunt and more rounded noses is captured. Blunt noses present a steep constant gradient until the peak is reached (see point B in Figure 6.3) followed by a sudden drop which stabilises pressure to an almost constant value (see point C in Figure 6.3). The less blunt noses 1 and 2 have lower peaks at point B and no sudden drop between points A and C. The transition between A and C is a continuous pressure increase, consisting of two gradients. This represents the typical pressure rise associated with passenger trains, as described in CEN (2003).

After point C, all three nose shapes tend to move towards identical pressure values. This part is believed to be associated with the entrance of the train's main body, which is common for all three cases.

At point D, the train is brought in contact with an expansion wave, and pressure reduces significantly, depending on the nose shape. The blunter the nose shape, the more extreme this pressure change is. This pattern continues to occur in the remaining of the graph, whenever the nose meets a pressure wave.

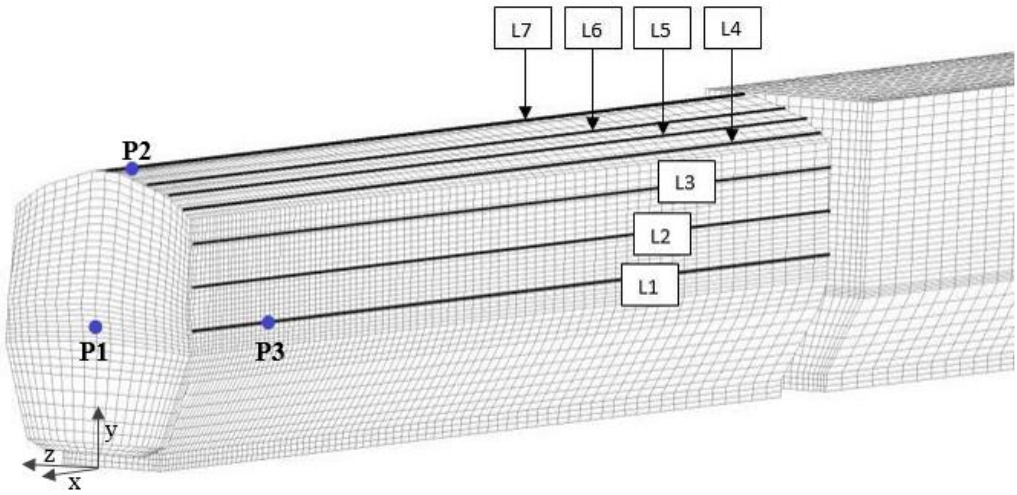

Figure 6.2: Class 66 locomotive - Location of measurement points on the train surface.

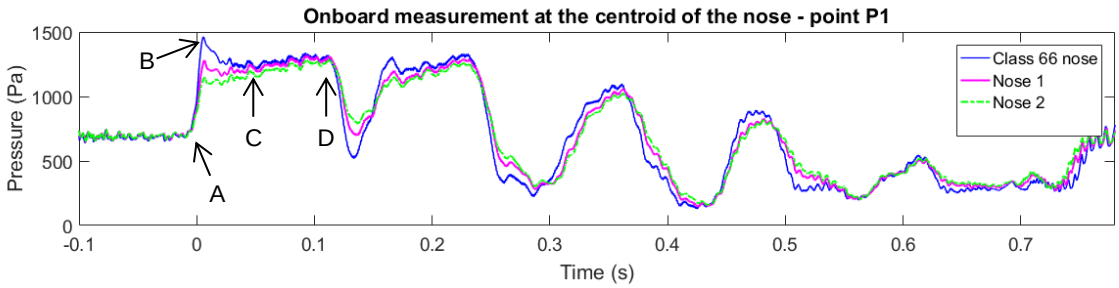

Figure 6.3: Effect of nose shape - Pressure measurements at moving point P1

The nose effect observed for the transition between points A to C is associated with the large separation bubble behind blunt noses. The separation levels for each nose are discussed in section 6.3, showing that nose roundness reduces the separation bubble size.

The constant gradient of blunt noses is caused by the nose entry and the separation bubble entry where the latter increases the blockage area causing a second rise of identical gradient. Rounded noses are not linked to large separation zones, and therefore do not create the second rise. Instead, after the nose entry, the main body enters, producing a less steep gradient. The link between separation, initial pressure rise and form of the gradient is fully unravelled in Chapter 7, where a synthesis of CFD results with 1D analysis is presented.

6.2.2.2 Stationary points at the tunnel wall

Figure 6.4 shows the pressure histories at 2 meters from the entrance. The location of the measurement point along the tunnel length was found not to affect the shape of the initial compression wave. The gradient for all nose shapes is identical to the ones

observed in the previous section for P1; one-part gradient for blunt noses which converts to two-part gradient as nose roundness increases. For noses 2 and 3 which represent the typical two-part gradient of passenger trains, the initial pressure is interrupted when the expansion wave passes by the measurement point. Therefore, it is unknown what the maximum pressure would be in a longer tunnel, as the arrival of the expansion wave would be delayed.

In general, Class 66 produces the highest amplitudes in Figure 6.4, which tend to reduce as the nose shape becomes more rounded. This is justified by the separation bubble size which increases the blockage ratio. A similar effect has been observed in the study of Ricco et al. (2007) who showed that the separation bubble size can affect the effective blockage ratio.

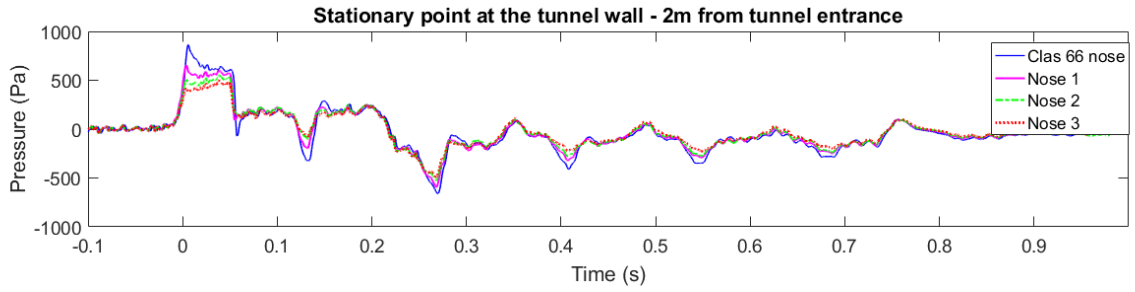

Figure 6.4: Effect of nose shape – Pressure histories at stationary point at the tunnel walls, located 2 meters away from the tunnel entrance

6.2.3 **Development of pressure waves with partially loaded trains**

This section investigates the effect of loading configuration to identify patterns and draw conclusions, through 2 comparisons:

i. Comparison 1 is presented in subsection 6.2.3.1 and includes two CFD cases, fully and partially loaded. The partially loaded train is described in section 4.8 and it consists of an empty wagon (wagon 1). All other wagons are loaded with containers.

ii. Comparison 2 in subsection 6.2.3.2 consists of the partially loaded CFD case mentioned above, and the partially loaded case from experiments, described in section 3.2.3.

6.2.3.1 Comparison 1: fully loaded versus partially loaded

The two computational models are shown in Figure 6.5, along with the measurement positions above wagon 1, moving points W1 and W2.

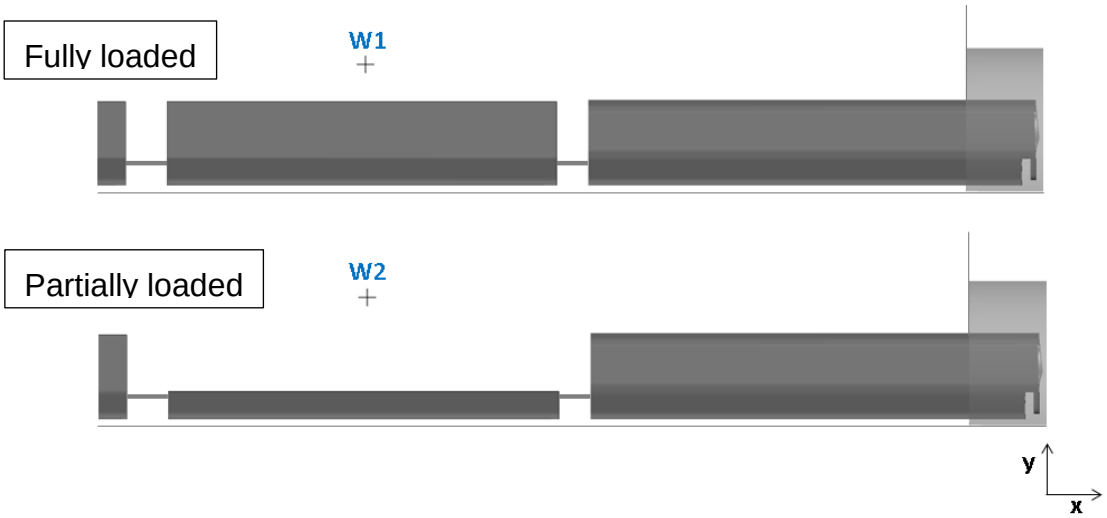

Figure 6.5: CFD models; Top: Fully loaded train; Bottom: Partially loaded train with empty wagon 1 - the remaining 7 wagons behind it are fully loaded; W1 and W2 are measurement points which move together with the train.

The analysis starts with stationary point measurements, which record pressure over time, plotted in Figure 6.6. After the train entry at t=0s, the development of the initial compression wave is identical for the two cases, as wagon 1 has not entered the tunnel yet. The first effects are found at point 1 when wagon 1 passes by the entrance. Its entry causes a second pressure reduction, explained by the generation of low energy expansion waves. The entry of the fully loaded wagon does not trigger such a pressure change.

At point 2, another pressure rise is detected, associated with the entry of the front face of wagon 2. This reduces again the blockage area inside the tunnel and causes the generation of another compression wave.

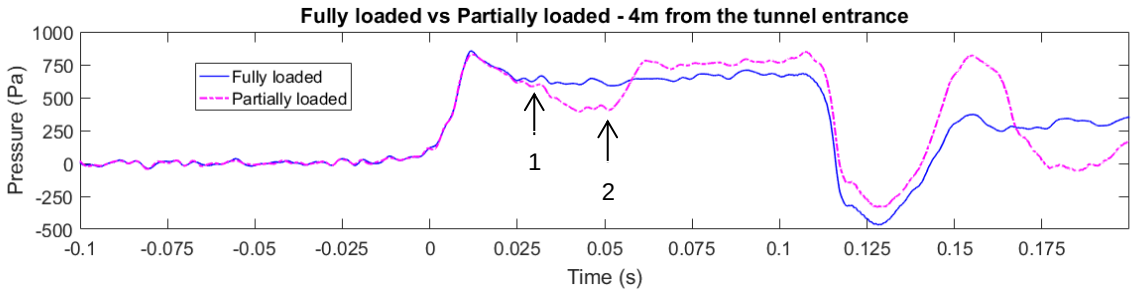

Figure 6.6: Pressure histories at the tunnel walls

To confirm the above finding for point 2, pressure was recorded at moving points W1 and W2, corresponding to the fully loaded and partially loaded cases respectively. Figure 6.7 represents the pressure histories at the aforementioned points, showing the nose and W1/W2 entry. Shortly after the entry of W1 and W2, the front face of wagon 2 enters and pressure increases. This increase only occurs for the partially loaded cases, confirming that the gaps between wagons generate low energy waves.

Figure 6.7: Pressure histories at W1 and W2, which are moving measurement points above the first wagon of the train.

The following paragraphs illustrate how these waves transfer their energy towards the train direction and affect pressure. Focusing on the partially loaded CFD case only, Figure 6.8 illustrates the location of two moving measurement points P1 and W2 and a stationary point at the tunnel walls, 1m from entrance.

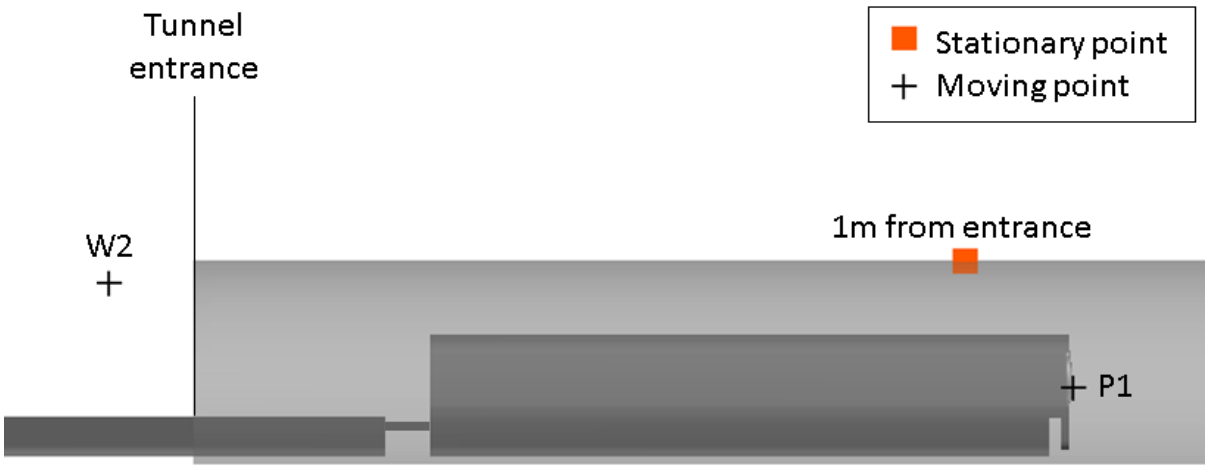

Figure 6.8: Instantaneous picture showing the location of the stationary and moving points plotted in Figure 6.9

In Figure 6.9, the pressure rise at point 1 represents the formation of the low energy compression wave above wagon 1. Then, the wave travels towards the train direction and passes by the stationary measurement point (1m from the entrance), causing the pressure increase at point 2. Following this, it arrives at the train nose, which is shown as point 3 in Figure 6.9.

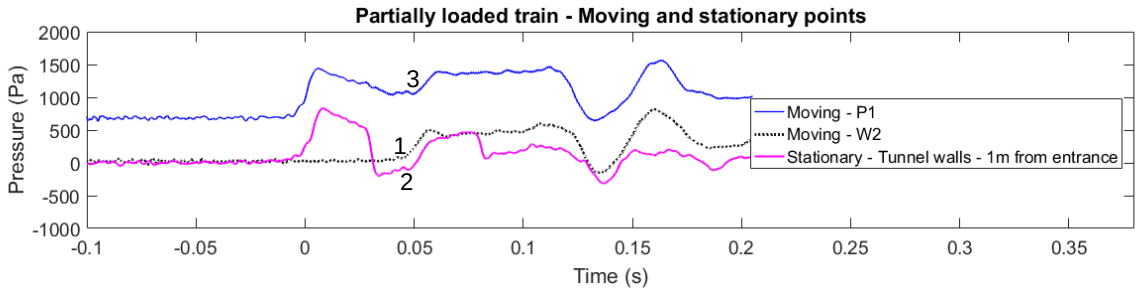

Figure 6.9: This graph shows how the pressure increase at W2 causes a pressure increase ahead of the train and inside the tunnel. P1 is a moving measurement point located at the centroid of the train nose

6.2.3.2 Comparison with experiments

To validate the findings from the CFD study presented in section 6.2.3.1, a comparison between the partially loaded CFD and experimental case is conducted. Figure 6.10 includes 2D sketches of the CFD and experimental model, referred as case 8 and 3 respectively.

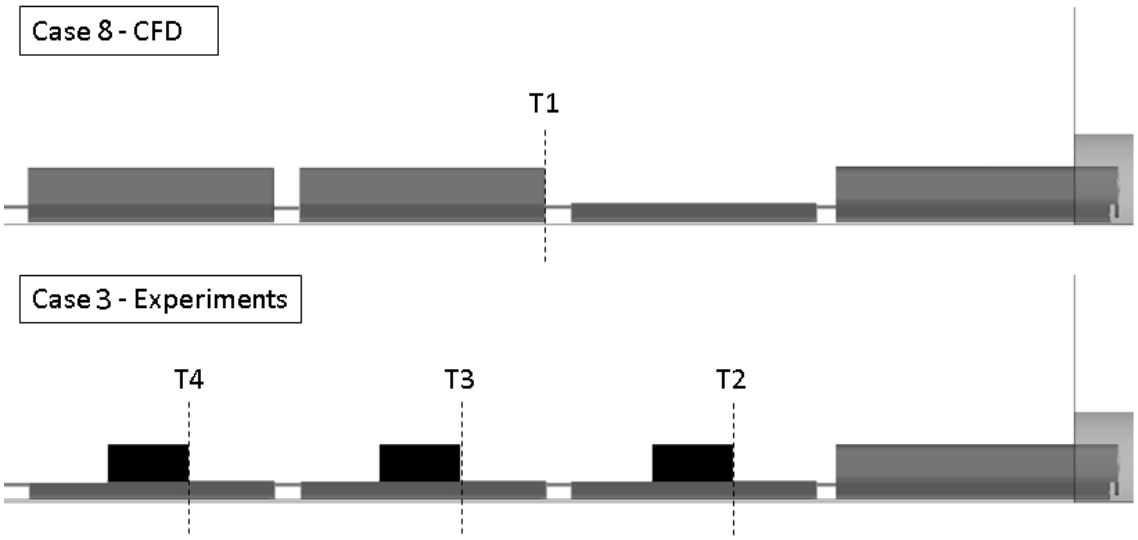

Figure 6.10: T1, T2, T3 and T4 are reference planes used for explanation of the results. For Case 8, only wagon 1 is empty while Case 3 is 33% loaded, with containers evenly spaced.

The pressure histories from both cases in Figure 6.11 validate that the entry of reference planes T1-4 triggers the formation of low energy compression waves. The front face of the container compresses the air particles as it enters the confined space of the tunnel. The following parameters can affect the formation of the waves:

i. The separation bubble size around the container.
ii. The gaps between containers; large gaps can increase the time difference between the formation of each wave.
iii. The length of containers; longer containers can result in higher peaks.

These findings are important as they are reported for the first time. Analytical methods which determine the maximum pressure inside the tunnel, by calculating the initial

compression wave C1 cannot be applied to partially loaded trains. As shown here, the maximum pressure can occur somewhere later than C1.

Figure 6.11 illustrates that for partially loaded case 3, the subsequent pressure rises are terminated after the entry of the third container. This is because of the expansion wave arriving at the measurement point (4 meters from the entrance). It is not known whether this pattern of repeated pressure rises would continue and up to what amplitudes, if a longer tunnel had been used (delayed arrival of the expansive wave to the measurement point).

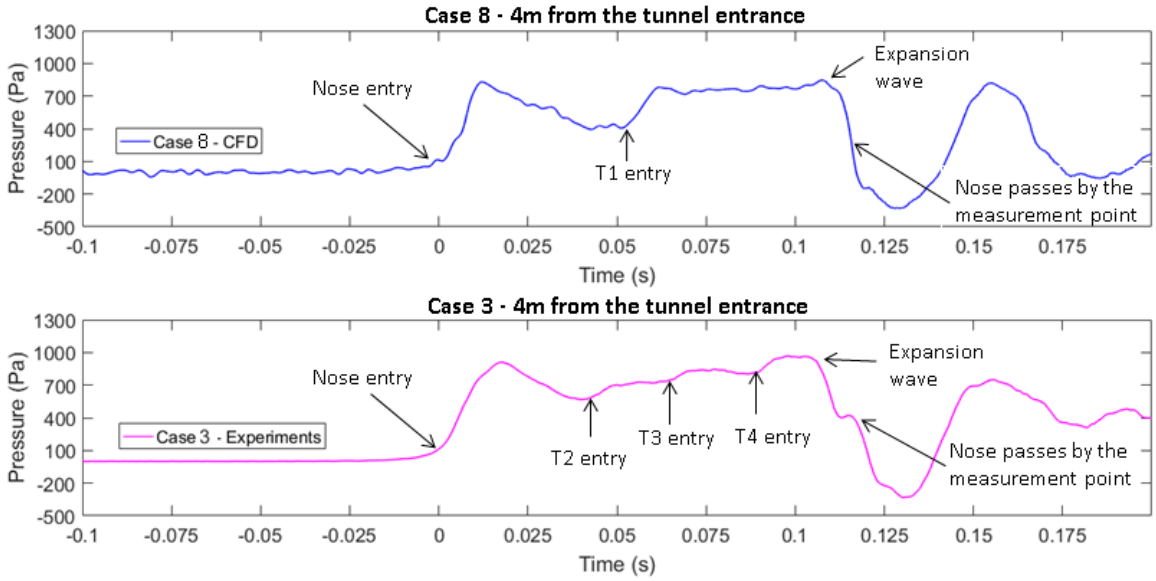

Figure 6.11: Pressure histories at the surface of the tunnel walls (stationary point)

6.3 Separation over the roof and at the sides of the train

6.3.1 Introduction

In this section, the separation levels around the locomotive are analysed. Sections 6.3.2-6.3.4 use results from case 4 (see Figure 1.1), while section 6.3.5 analyses the findings from cases 5-7.

For the purposes of this study, the reattachment point and height of the separation bubble around the train head will be studied to assess changes in displacement thickness, increased pressure drag, energy losses, noise and lateral vibration phenomena (Suzuki, 1996).

The analysis focuses on the separated flow at the sides and roof of the locomotive. To that end, the separation and reattachment points can be computed using the longitudinal component of wall shear stress τ_w (Sturm et al., 2012), which is in this case is parallel to the inlet flow and train roof. τ_w is the force per unit area applied to the fluid by the wall, defined as:

$$\tau_w = \mu \left(\frac{\partial u}{\partial y}\right)_{y=0} \tag{24}$$

At the point of separation and reattachment, it is commonly known that $\left(\frac{\partial u}{\partial y}\right) = 0$, derived from Navier-Stokes equations (Sturm et al., 2012). Calculating the nominal magnitude of τ_w would give positive values only, therefore its longitudinal component is used in this study, plotted along the length of the locomotive (L). The sign of τ_w depends on the coordinate axis, which in this case is opposite to the flow, producing

positive values within the separated flow area. As noted before, the separation bubble length is defined as the distance between the point of separation and point of reattachment. Table **6.1** below shows the reattachment point recorded at various heights h of the locomotive and expressed in terms of its position along the locomotive length L (see Figure 6.12 and Table 6.1 for the location of each line). The unsteady RANS simulations showed that the reattachment points shown in Table 6.1are time-independent as the separation length remains unchanged over time (both in open air and inside the tunnel). The analysis presented in this study focuses only on one side of the locomotive, as negligible differences were found between the left and right sides of the tunnel.

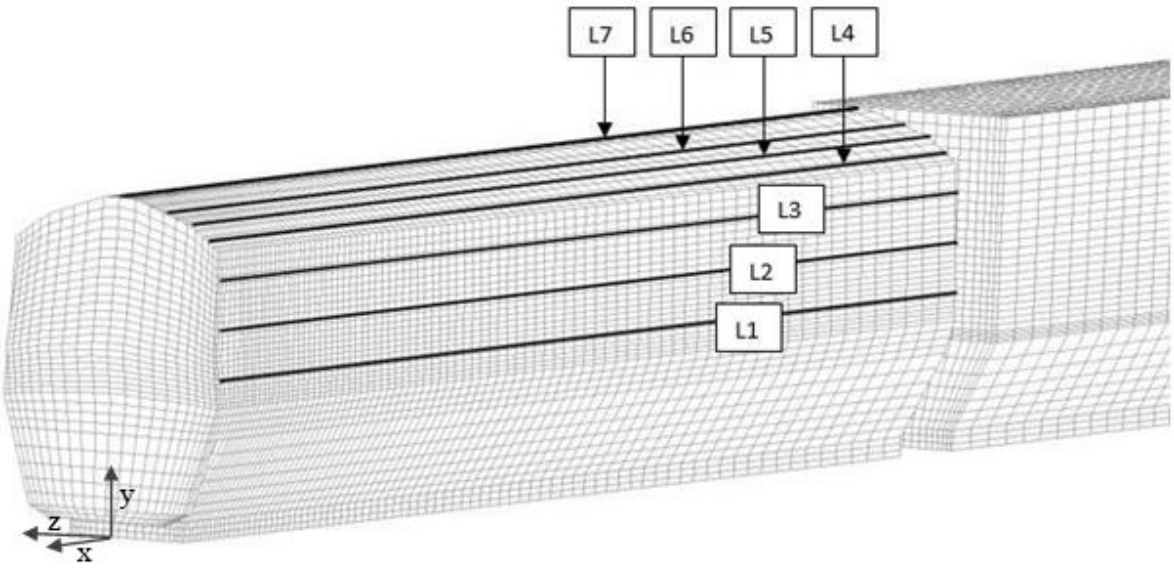

Figure 6.12: Position of measurement lines at the locomotive surface

Table 6.1: Reattachment point – Open air and Tunnel (0.124s)

	Line	Line position (% of h)	Reattachment point (% of L) Open air	Reattachment point (% of L) Tunnel	Change (%)
ROOF	L7	100	25.1	17.0	32.0
	L6	96.62476801	23.0	17.0	26.0
	L5	93.9269429	20.5	15.2	26.0
SIDES	L4	89.83657749	19.0	14.0	26.0
	L3	79.3253104	19	14	26
	L2	65.79018854	23.8	16.5	31
	L1	52.17358912	26.1	19	27

6.3.2 **Separation over the roof**

Inside the tunnel, the flow deflection angle changes due to the presence of the tunnel walls which redirect the flow towards the train surface. Figure 6.13 shows the values of τ_w along the non-dimensional locomotive length. The flow separates at the corners of the train head (origin of the horizontal axis), where wall shear stress is zero. After separation, τ_w becomes positive because the flow has the same direction as the train, in alignment with the positive longitudinal axis of the coordinate system. Air flows towards the front of the train, indicating backflow at the core vortex. Behind this point, the reattachment of the separation bubble to the train surface occurs when the wall shear stress is zero again. When the train enters the tunnel, the separation point remains unchanged while the reattachment point moves towards the front (compared

to open air). Consequently, the separation bubble length is reduced by up to 32% inside the tunnel. In the lateral direction, the most intense reduction in separation bubble length is found at the centre of the track, attributed to the extended corners of the train at this region. It can be observed that the higher the distance from the centre of the track, the shorter the separation length. This can be confirmed from Figure 6.16 which shows the levels of wall shear stress at the locomotive surface.

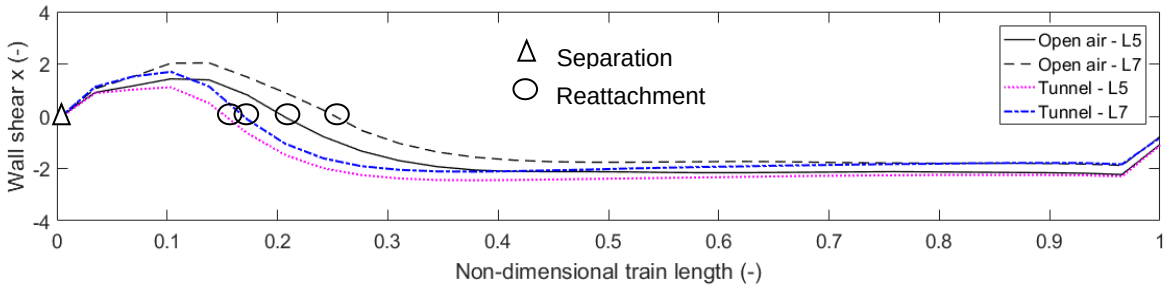

Figure 6.13: Separation at the roof of the locomotive; Nose at 0 and tail at 1.

After reattachment, within the recovery region, the values of τ_w continue to drop. This is the region where a turbulent boundary layer starts building up gradually both in the longitudinal and vertical directions. Previous studies have highlighted that due to the nature of turbulence, mixing occurs at this area and turbulence intensity is high, but decreases with distance from the reattachment point (Jovic, 1996). As the distance from the separated flow increases, the boundary layer is not influenced by the upstream mixing flow and stabilises.

Post-recovery, τ_w stabilises to constant values which indicates a turbulent boundary layer is formed, between 52 and 97% of the locomotive length at the sides and

between 39 and 97% over the roof. The size of the boundary layer in the vertical direction is believed to be constant within this region and significantly smaller than the height of the separation bubble (Chang, 1961). Moving towards the rear, at 97% of the locomotive length, the flow separates again due to the sudden gap between the locomotive. Similarly to the train head, this is a geometry induced separation and its location is not affected by the tunnel walls and remains unchanged after the train entry.

Figure 6.14 shows the velocity profile across L8, which is a vertical line at the maximum height of the separation vortex), at the centre of the track (z=0). In open air, this occurs at 70% of the separation vortex length, and inside the tunnel at 63%. The longitudinal component of velocity is normalised with train velocity V and plotted against the distance from the highest point of the roof (y minus h). The velocity sign has been adopted in the direction of the coordinate system for illustration purposes. The negative curved profile shows an adverse pressure gradient within the separated flow. The height ‘H’ of the separation bubble is defined as the distance from the inflection point to the wall, which is within the boundary layer. H is slightly lower inside the tunnel, compared to open air. Outside this region (between 0.028m and 0.075m on the vertical axis of Figure 6.14), the freestream velocity is higher in the tunnel, due to the reduced cross-sectional area causing flow acceleration. The negative velocities within the vortex indicate backflow of significant strength, which remains unchanged during train entry.

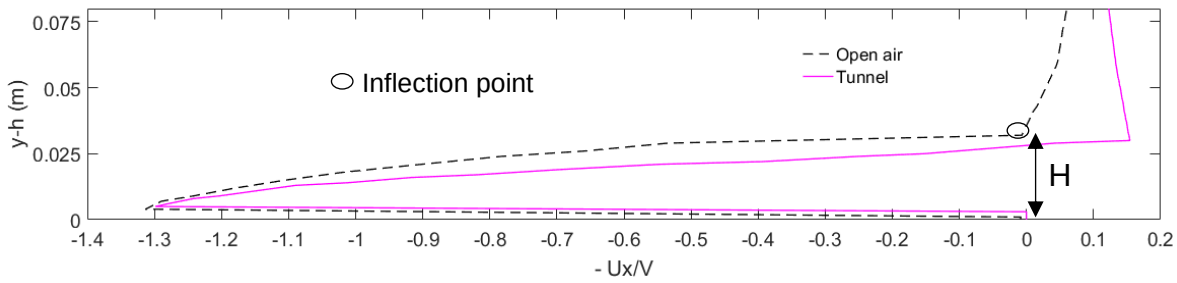

Figure 6.14: Instantaneous normalized velocity profile along L8 (see Figure 6.16); z=0m

As a general observation, the flow separation length reduces inside the tunnel (see Table 6.1). Therefore, separation induced drag and vibration are believed to be lower around the head of the locomotive. The study of Chang (1961) states that pressure drag is the largest percentage of total drag arising from flow separation. However, the current study investigates a train-tunnel scenario, where additional pressure drag arises from the presence of the tunnel walls and pressure waves.

6.3.3 **Separation at the sides**

Figure 6.15 presents the variation of separation length at the sides of the train, by comparing measurement lines L1 and L3 in open air and inside the tunnel. As shown, the maximum separation length is found at 52% (L1) of the train height (both in open air and inside the tunnel). This reduces when moving towards the roof of the train as the locomotive width reduces gradually above the middle height. This indicates that the wider shape of the train head, the longer the separation bubble. This is identical to the separation over the roof, where the extended edge of the train head in the vertical

direction produces the maximum separation. The edges affect the gap between the locomotive and tunnel walls, changing the deflection angle at separation. Therefore, it is believed that the above observations depend highly on the tunnel shape as a square tunnel could cause different effects. Another critical parameter is believed to be the blockage ratio as it defines the gap between the train and tunnel. However, the most significant variations are expected with different nose shapes, as they define the angle of deflection α. As discussed in section 2.1, angle α defines the separation length.

The findings discussed above can be confirmed from Figure 6.16 which shows the contours of τ_w along the locomotive surface. The maximum separation levels at the sides and roof of the train are identical; with slightly longer separation levels on the latter (see Table 6.1). Although the separation length at the bottom of the train is significant, this is believed to be because of the fully filled underbody of the train, used for the purposes of this study.

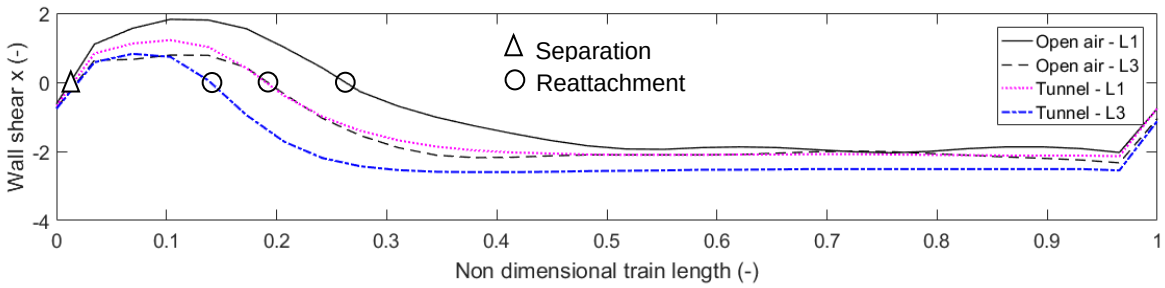

Figure 6.15: Separation at the sides of the locomotive; Nose at 0 and tail at 1

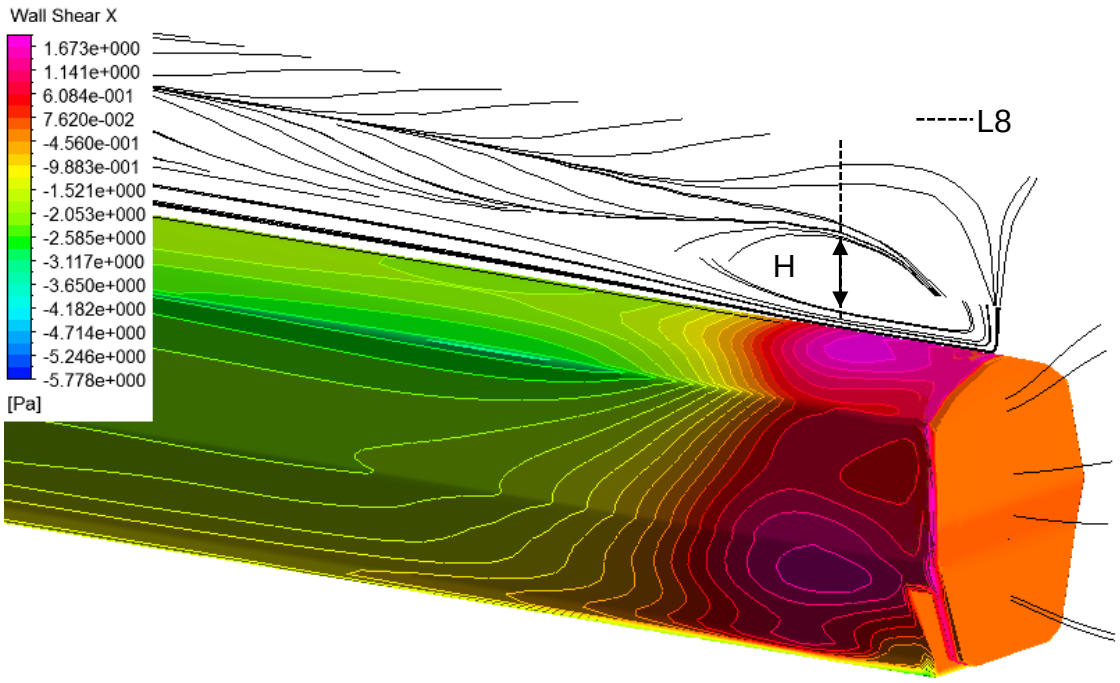

Figure 6.16: Wall shear stress contour and surface streamlines inside the tunnel, showing the height of the separation bubble and the vertical velocity profile (see Figure 6.14)

6.3.4 **Time-dependence of separation**

The unsteadiness of the flow around the train can be related to the nature of separating and reattaching flows which exhibit low-frequency unsteady behaviour (Driver, Seegmiller and Marvin, 1987) and to the effects of the transient pressure waves. In practical terms, unsteadiness in the flow is related to generating vibration and noise (Neumann, 2003). This has led to the need of monitoring or controlling flow separation, especially for applications of higher speeds and therefore increased drag (i.e. aerospace applications).

Figure 6.17 compares the wall shear stress values (longitudinal component) between two locations on the locomotive surface, at different instants. It indicates that the points of separation and reattachment (when τ_w=0) remain unchanged across different instants. However, the velocity field is different at the two instants, due to the turbulent nature of the flow (evident from the values of wall shear stress before and after reattachment). Mixing occurs, affecting the circulating flow. This is translated to changes within the core vortex and the dead air region behind it. After the reattachment point, moving further backwards, the fully developed turbulent boundary layer downstream of the reattachment point experiences different velocity gradients. However, the separation point at the rear of the locomotive remains unchanged.

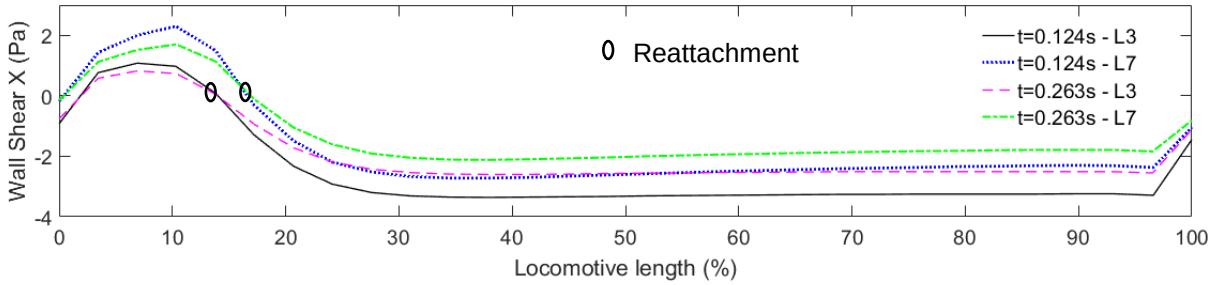

Figure 6.17: Wall shear stress at different instants inside the tunnel

6.3.5 **Effect of nose shape on separation**

This section examines the effect of nose shape on the separation levels around it. Due to the shape of noses 1-3 not representing real trains, the analysis here is qualitative.

Figure 6.18 illustrates the streamlines around all nose shapes, showing the clear reduction in separation bubble size with nose roundness. For the flow over the roof, this is translated to earlier reattachment and lower height of the bubble. The reduction can be explained by the smaller flow deflection angle at the separation point due to smoother transition between the front face of the train and the roof/sides. However, for all cases the point of separation remains unchanged, despite the extensions introduced for noses 1-3.

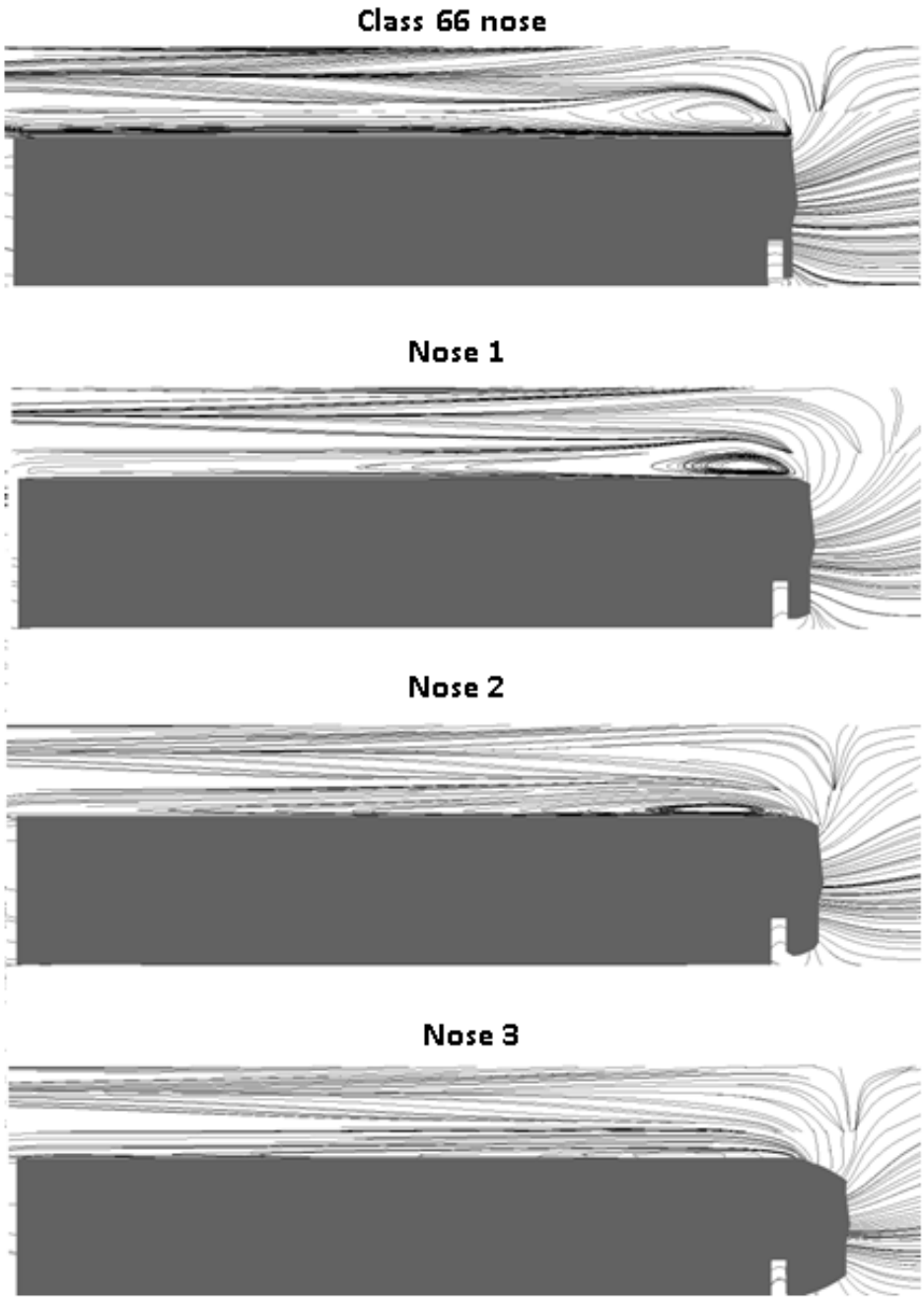

Figure 6.18: Streamlines showing the separation bubble size inside the tunnel. For Nose 3 the separation bubble reduces to an extend that it not visually detectable

Although a quantitative comparison is not the aim of this section, the above observations need to be confirmed using numeric criteria. Wall shear stress along the locomotive surface is plotted in Figure 6.19, comparing the Class 66 nose to Nose 1. On the horizontal axis, 0 and 100 represent the locomotive nose and tail.

Figure 6.19 shows that the separation point does not change at the front face of the nose (0% of locomotive length). This can be also be confirmed from the streamlines in Figure 6.18. When moving further away from the nose, the reattachment point occurs earlier for Nose 1, due to the smaller flow deflection angle at the separation point.

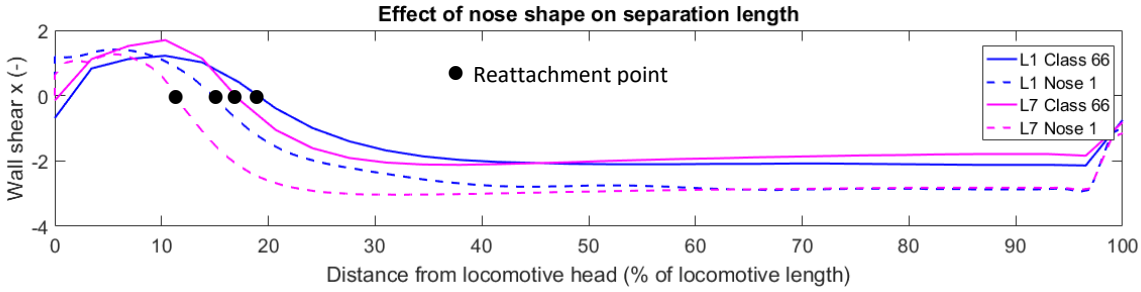

Figure 6.19: Wall shear stress along the length of the locomotive inside the tunnel

6.4 Velocity field around the train

This section investigates the velocity field around the train using the longitudinal component of velocity. The results and analysis in sections 6.4.2, 6.4.5 and 6.4.6 have been published elsewhere, see Iliadis et al. (2019). The author of this thesis is the first author of the published article.

The analysis is divided into the following subsections:

1. Confirmation that the velocity field around the train is not changing with higher speeds (see measurement line L9 in Figure 6.20 below).
2. Comparison between open air and tunnel velocities (see measurement line L9 in Figure 6.20 below).
3. Velocity variation along the lateral direction (see measurement lines L10-L12 in Figure 6.20 below).
4. Velocity variation along the vertical direction (see measurement lines L13-L18 in Figure 6.20 below).
5. Velocity dependence on the pressure waves and variation along the train length.
6. Time-dependence of velocities.
7. Effect of nose shape on the velocity field.

Subsection 1 is a confirmation study which uses the settings of case 4 (see Figure 1.1) with an increased train speed (38.5m/s). Results for subsections 2-6 above have been obtained from case 4 (at 33.5m/s), while 7 represents cases 5-7 (modified nose shapes). All results presented in this section are instantaneous. Table 6.2, Table 6.3 and Figure 6.20 show the exact location of the measurement lines and planes.

‘’As shown in the previous sections the separation length between the roof and the sides of the train vary. Similar differences have been observed for the velocity field by Soper et al. (2014) who found that the longitudinal component of velocity U_x is higher at the sides than at the roof. Based on the above, the analysis of the velocity field in the study focuses on the sides of the train only’’ (Iliadis et al., 2019, p. 12).

Table 6.2: Location of measurement lines

Line	Distance from the centre of the track (m)	Distance from ground (m)
L9	0.07	0.09
L10	0.09	0.09
L11	0.11	0.09
L12	0.13	0.09
L13	0.07	0.11
L14	0.07	0.13
L15	0.07	0.15
L16	0.07	0.17
L17	0.07	0.19
L18	0.07	0.21

Table 6.3: Location of measurement planes (in scaled dimensions)

Plane	Distance from the centre of the track (m)	Distance from ground (m)
Plane 1	-	0.09
Plane 2	-	0.11
Plane 3	-	0.13
Plane 4	-	0.15
Plane 5	-	0.17
Plane 6	-	0.19
Plane 7	0	-
Plane 8	0.07	-
Plane 9	0.09	-

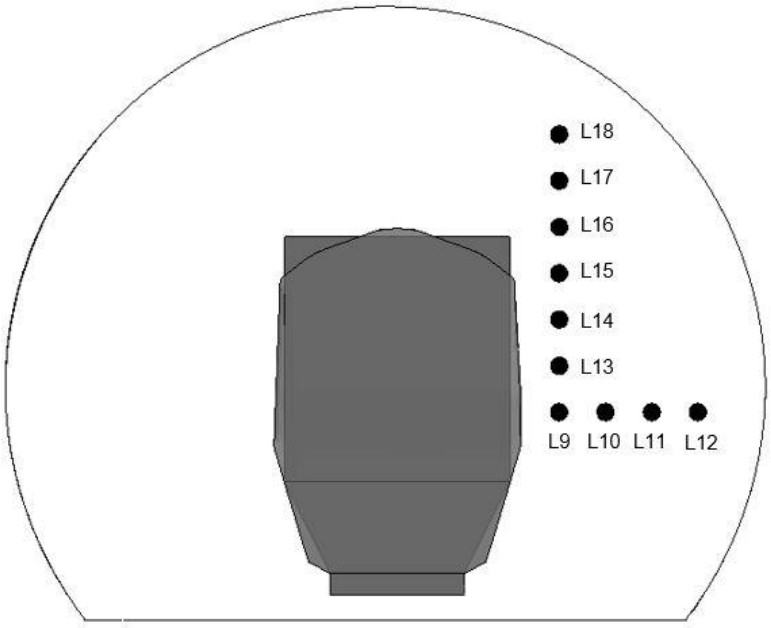

Figure 6.20: Schematic of the measurement lines' location in relation to the train

6.4.1 **Confirmation of train speed effect**

This simulation is identical to Case 4 with a modified speed (increased to 38.5m/s) and analyses slipstream results in open air and inside the tunnel. Figure 6.21 shows the normalized longitudinal component of velocity in open air, recorded at L9 (see Table 6.2 and Figure 6.20 for exact location). It is clearly shown that increasing the train speed does not affect the flow field when normalized. The upstream region (-2 < Distance from nose < 0), the nose region (0 < Distance from nose < 0.5) and the flow region behind it are not affected. A complete discussion and analysis of the flow phenomena at these regions is given in section 6.4.

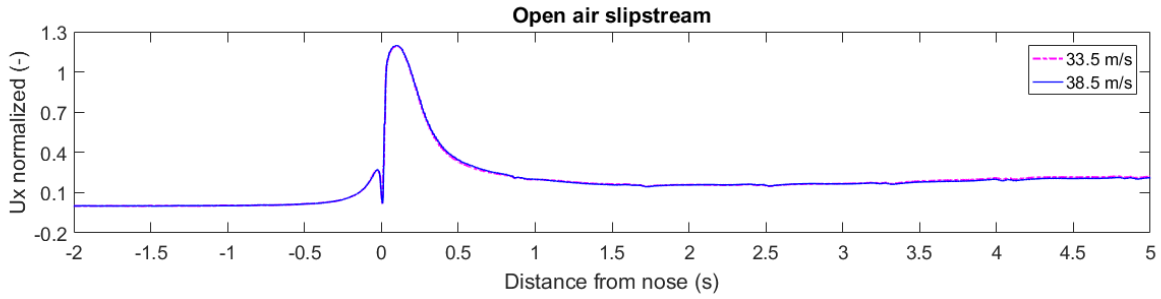

Figure 6.21: Open air: Normalized velocity at L9

6.4.2 **Comparison between open air and tunnel velocities**

This section shows how the velocity field changes when the train enters the confined space of the tunnel, by extracting results from L9.

The vertical axis in Figure 6.22 shows the longitudinal component of velocity at L9, normalised with the train speed. On the horizontal axis is the distance from the train. In the upstream region (negative axis), velocity is slightly increased because of the displaced air ahead of the nose. When the train nose is in the middle of the tunnel length, the upstream velocity is significantly higher than in open air due to the restricted space inside the tunnel and the presence of pressure waves. The upstream velocity is 25% of the velocity peak at the nose.

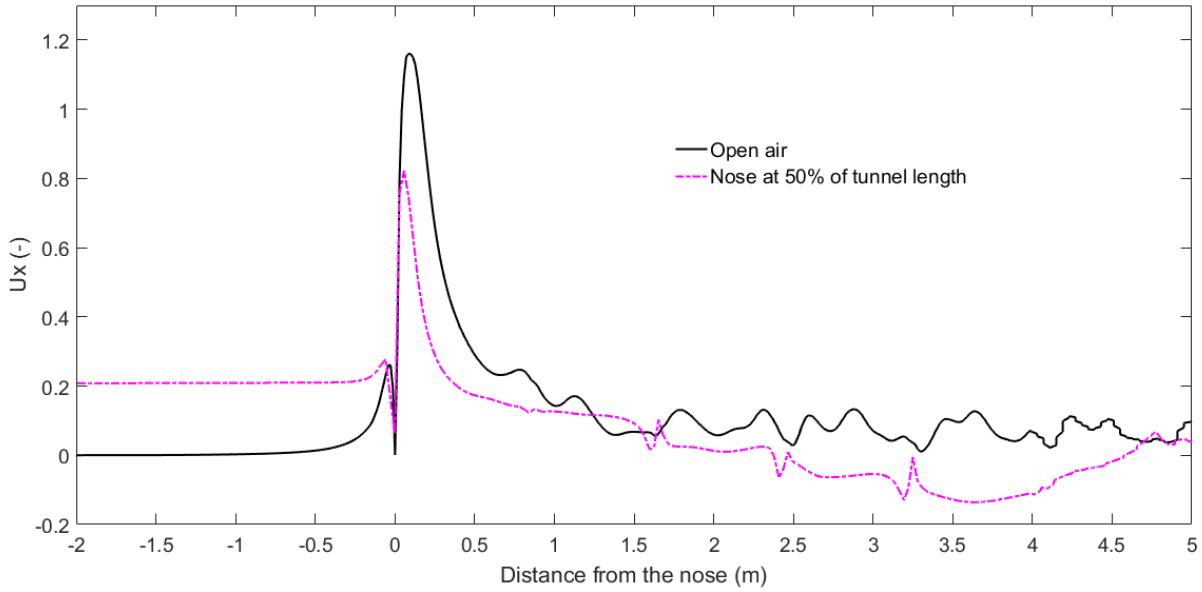

Figure 6.22: Normalised longitudinal component of velocity U_x at measurement line L9. The horizontal axis represents the scaled distance from the train nose, which is positive towards the tail and negative towards the train direction.

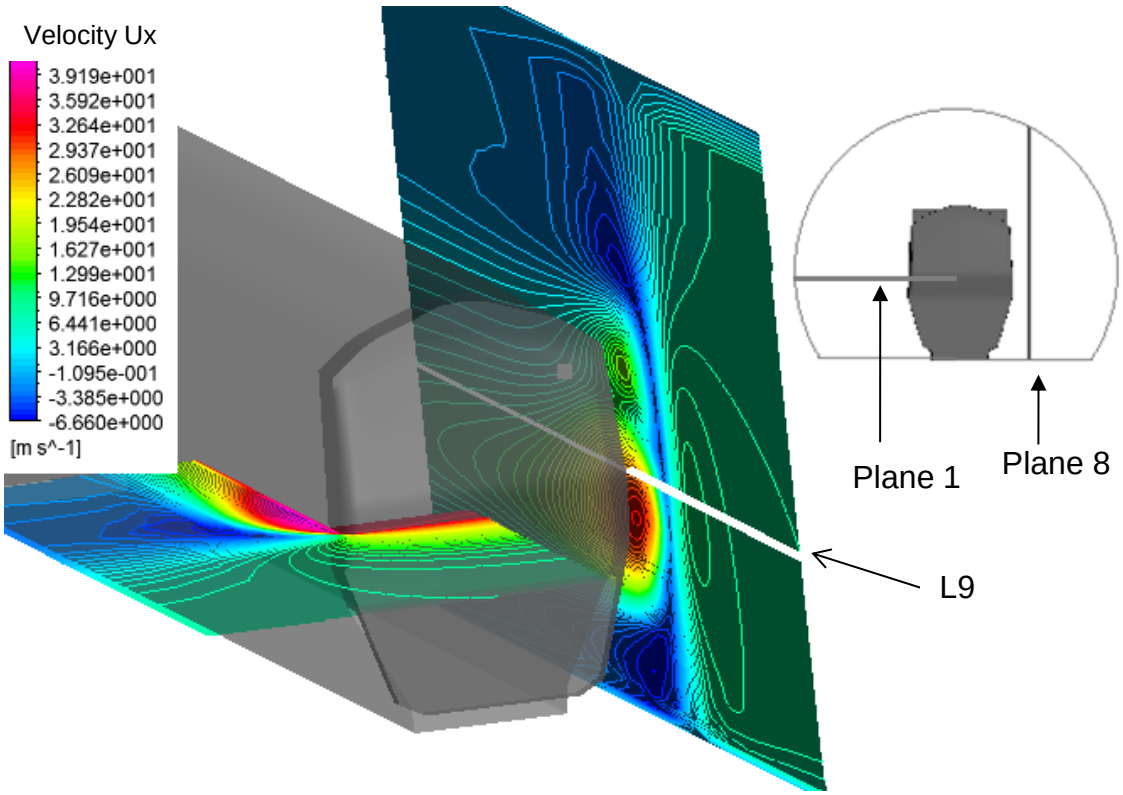

Figure 6.23: Contour of longitudinal component of velocity around the nose inside the tunnel. Planes 1 and 2 are located 0.09m and 0.07m (2.25m and 1.75m in full scale) from the ground and centre of the track respectively. Measurement line L9 is located on Plane 2.

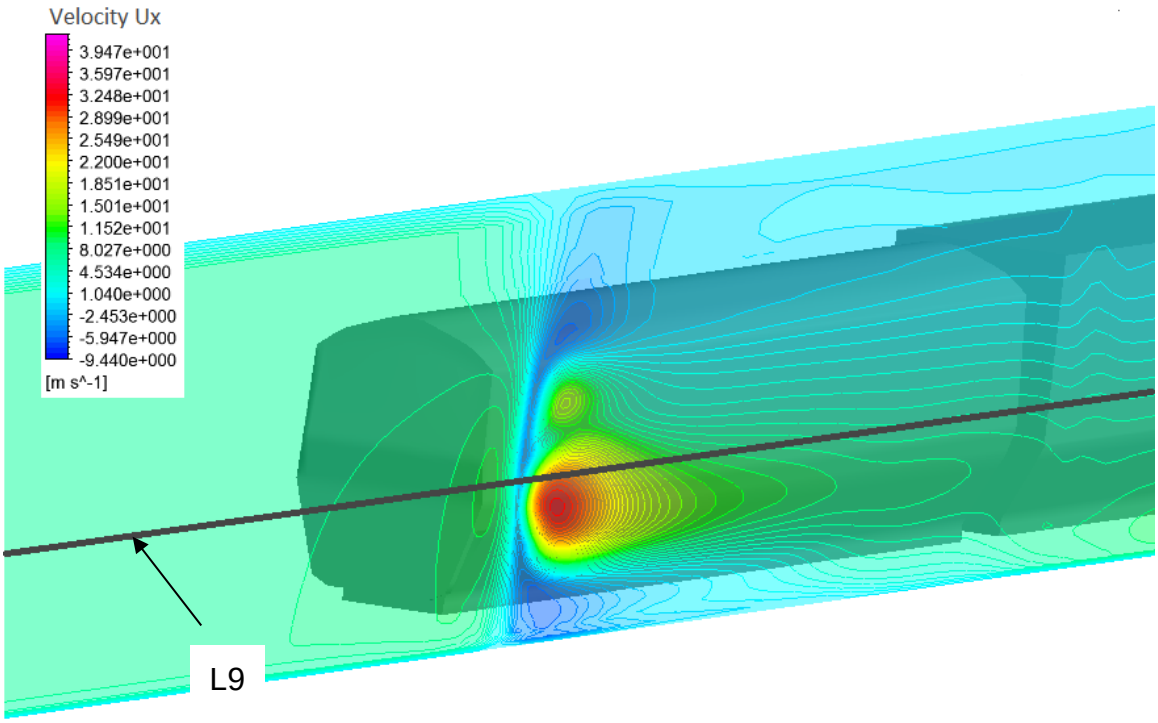

Figure 6.24: Velocity contours at plane 8 (0.07m from the centre of the track)

The open air peak velocity at the nose region is higher than the train speed by 20%. From Figure 6.22, it is evident that the magnitude reduces by 30% when the train is inside the tunnel. Similarly, the peak length is shorter, attributed to the shorter separation bubble inside the tunnel.

Figure 6.23 confirms previous research findings which suggest that the velocity magnitude is related to flow separation around the train and reduces when the distance from the centre of the track increases, both on passenger (Baker, 2010) and freight trains (Soper, Baker and Sterling, 2014). Plane 8 on Figure 6.24 illustrates that the maximum nose velocities are found near the middle-height of the train, where the locomotive corners are closer to the measurement point (L9). This observation

confirms the fact that the closer to the train surface, the higher the velocity. A similar relationship was observed for separation and distance from the surface in the previous sections, confirming that separation and velocities are linked.

Within the boundary layer region, velocity is relatively stabilised due to the homogeneous geometry of the wagons. Soper et al. (2015) found that when the train is partially loaded with container wagons, the leading faces of the containers cause additional velocity peaks making the flow more complex. Although there are no significant fluctuations in the results of the current study in the boundary layer region, any small size effects can be explained by the gaps between the containers.

6.4.3 **Velocity variation along the lateral direction**

Figure 6.25 presents velocities U_x for lines L9-L12.The conclusions drawn from this plot are given below:

- Ahead of the train nose, no differences are found between L9-L12. U_x is constant at approximately 0.22, showing a homogeneous flow field. Near the nose, U_x at L9 increases due to redirected flow, as it the closest line to the train surface. L10-L12 are located further from the surface and not affected. Following this, all lines experience a sudden velocity drop, irrelevant of their location.
- At the train nose (0m), L9 experiences its maximum positive peak because it is near the separation vortex. At higher distance from the vortex (lines L10-L12), the nose peak is negative, with the most extreme values observed for L11,

approximately 25% of the positive peak of L9. L12 has the furthest distance from the train surface but it closer to the tunnel walls, which causes additional friction.

- Between 0.5m and 2.75m of the locomotive length is a region of almost constant or low rate velocity decrease. No significant effects are observed in this region compared to the rest of the plot.
- After 2.75m from the nose, L9-L12 amplitudes tend to increase with the steepest gradient observed at approximately 3.5m (halfway the locomotive length). The higher the distance from the track, the more significant the velocity increase. This indicates that the flow tends to move towards the tunnel wall. At this location, L12 is the closest to the tunnel walls and has the highest peak among all lines, which is approximately 75% of the maximum velocity observed in this study (at L9). This suggests that high velocity peaks are not always linked to the nose.

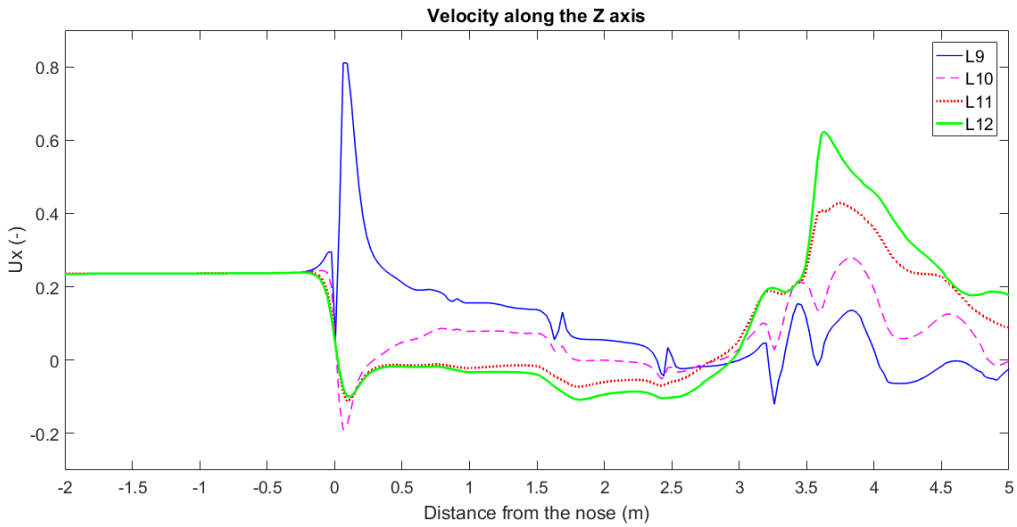

Figure 6.25: Normalized velocity variation with increasing distance from the centre of the track, when the train is halfway throughout the tunnel. The origin of the longitudinal axis represents the nose of the locomotive (scaled distances).

Figure 6.26 can give additional information to the plotted lines of Figure 6.25. The absolute longitudinal component of velocity is shown. The highest velocities are found at the centre of the track above the roof where the flow accelerates because of the separation vortex (see plane 7). The velocities just ahead of the locomotive decrease with distance from the centre of the track, because they are moving further from the air stagnation area.

Plane 8 shows the separation vortex at the sides, which is located at approximately halfway the locomotive height and moves towards the ground as the distance from the nose increases. The maximum velocities within the vortex occur at its centre and are comparable to the ones above the roof (at the centre of the track – see plane 7).

The same plane shows a similar vortex of significantly lower velocities at the upper half of the train, above the main vortex discussed above.

At Plane 9, no remarkable velocities are detected since this plane is further from the locomotive sides.

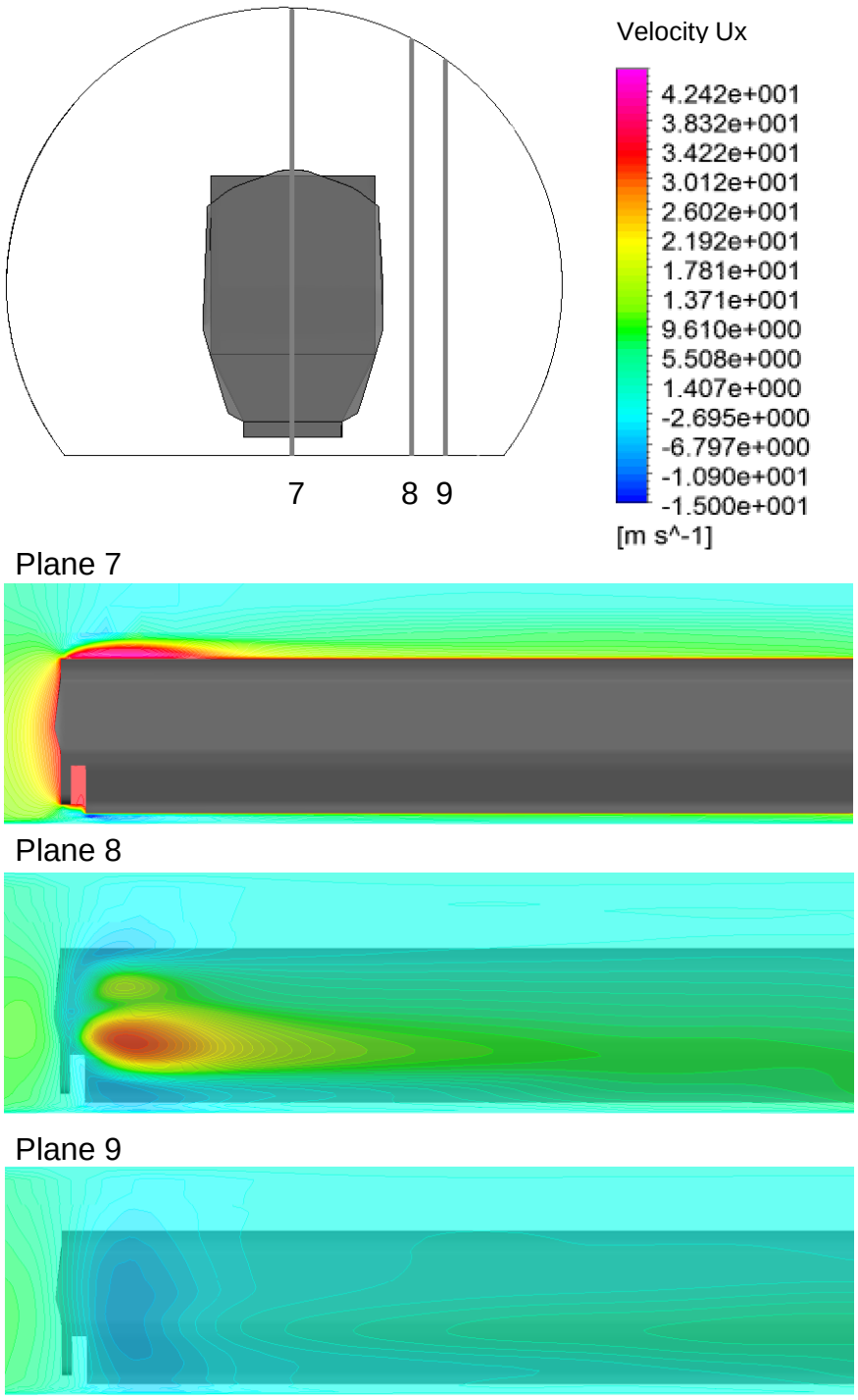

Figure 6.26: a) Schematic of the location of the measurement planes in relation to the train; b) Contours of longitudinal components of velocity - the nose is at 50% of the tunnel length

6.4.4 **Velocity variation along the vertical direction**

Figure 6.27 shows the variation of velocities at the sides of train, as the distance from the ground increases. The following observations have been drawn:

- Ahead of the nose: L9, L13 and L14 experience a velocity rise followed by a drop closer to the nose, attributed to their distance from the separation vortex at the sides. Velocity at L15-L18 drops directly as it located further from the vortex.
- At the nose, the most significant effects are observed for L9 followed by L13, L14 and L15. As the distance from the main separation vortex at the sides increases (L16, L17 and L18), U_x changes at a smaller rate.
- Planes 1-4 are located at the upper half of the train, 1 corresponding to the middle height and 4 approximately to the roof. The maximum velocities are located at Plane 1 followed by planes 2-4. This proves the relation between separation size and velocities, as the analysis in the previous section showed that separation is maximum at the middle height and decreases with distance from it.
- Plane 5 is located above the roof of the locomotive where air velocity is higher than the train speed and the highest recorded for all planes in Figure 6.29. The maximum values occur at the centre of the track where the curved roof is closer to the flat plane.
- Plane 6 is the top plane in the vertical direction. Velocity at this location is not significantly affected by the separated flow around the train.

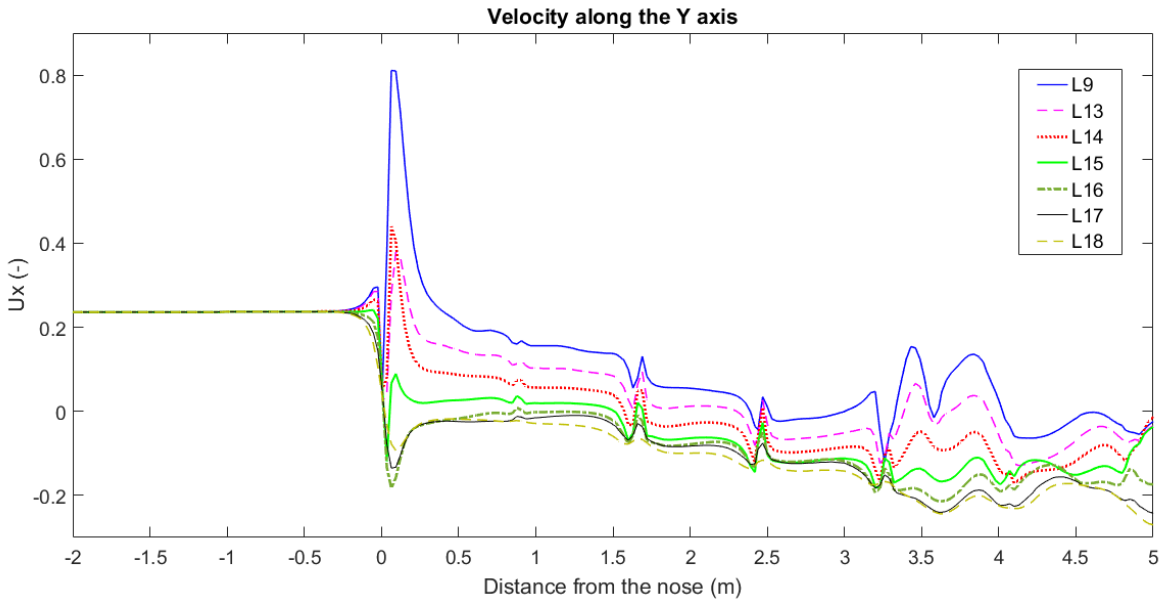

Figure 6.27: Longitudinal component of velocity variation with increasing distance from the ground, when the nose is at 50% of the tunnel length. The origin of the longitudinal axis represents the nose of the locomotive. Distance from the nose is in scaled form.

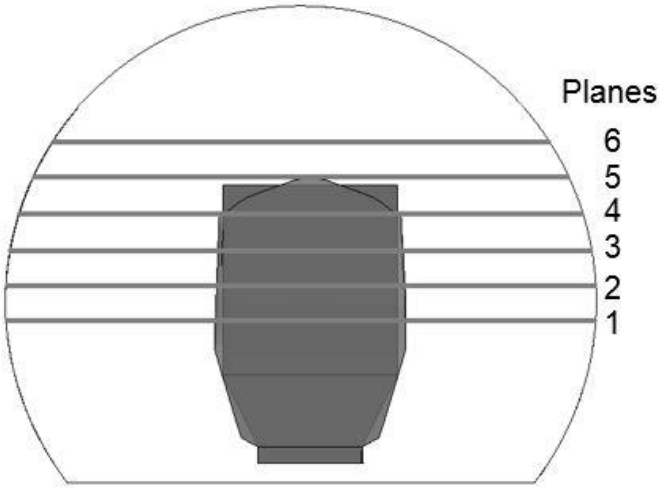

Figure 6.28: Schematic showing the location of two-dimensional Planes 1-6 in relation to the train.

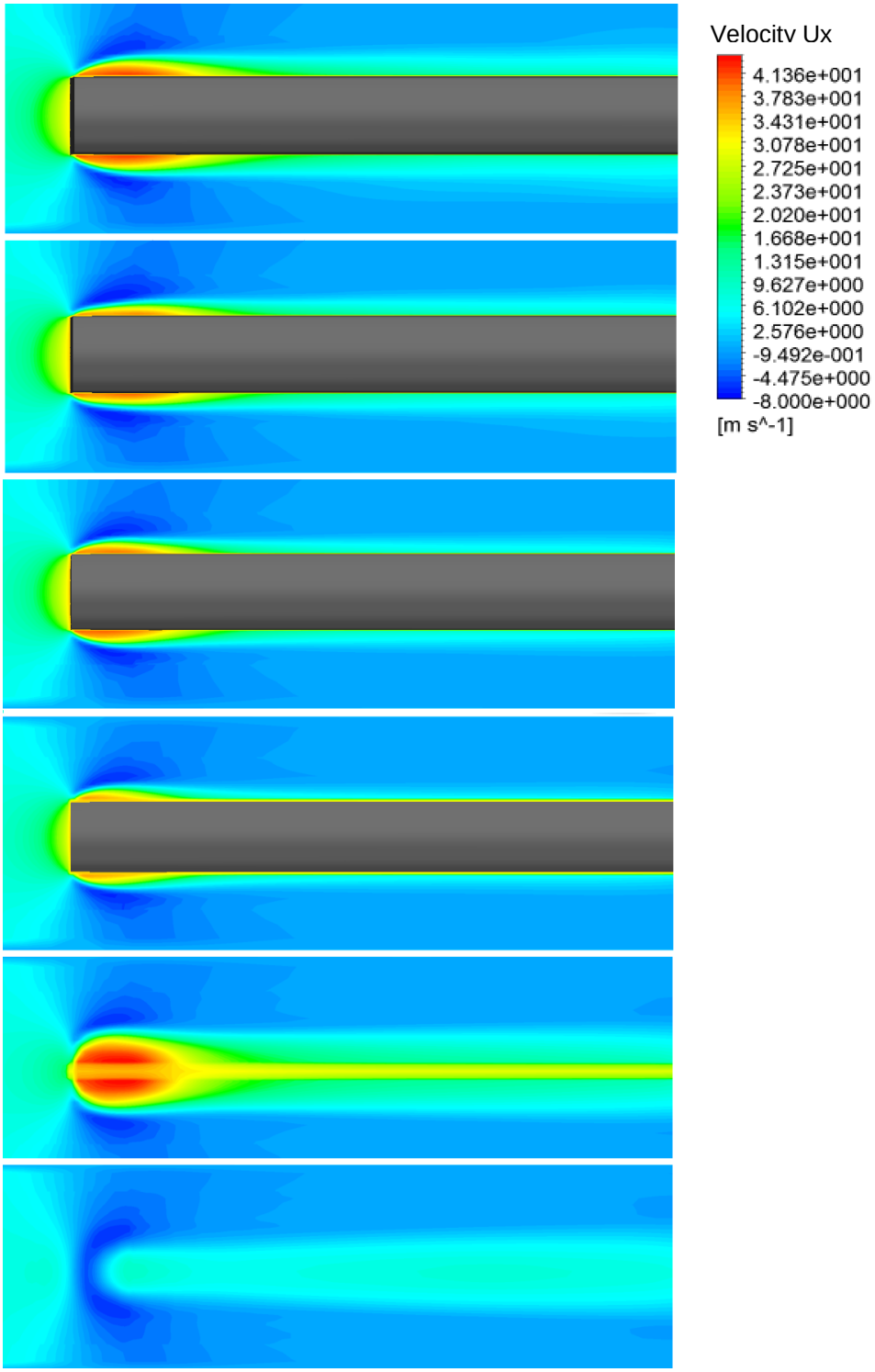

Figure 6.29: Longitudinal component of velocity contours of planes 1-6 (from top to bottom), when the nose is at 50% of the tunnel length.

6.4.5 Velocity dependence on the location of the train and pressure waves

Figure 6.30 shows the instantaneous normalized velocity extracted from L9 at t=0.3439s, along the length of the tunnel in relation to the position of the train and the pressure waves. This instant has been selected based on the fact that a compression wave has just passed from the train tail and therefore, its influence on the velocity field around it can be detected. In addition, the selected time ensures that the train is well inside the tunnel, allowing analysis of the velocity field around the whole train length. The development of the pressure waves until this instant are shown in Figure 6.30b.

Apart from the nose peak, the velocity values between the nose and tail are lower than the rest of the graph and in some cases negative. These effects are believed to be linked to the position of the probe being within or very close to the separated flow along the train which causes energy losses. The lowest negative velocities are found at approximately 50% of the train length.

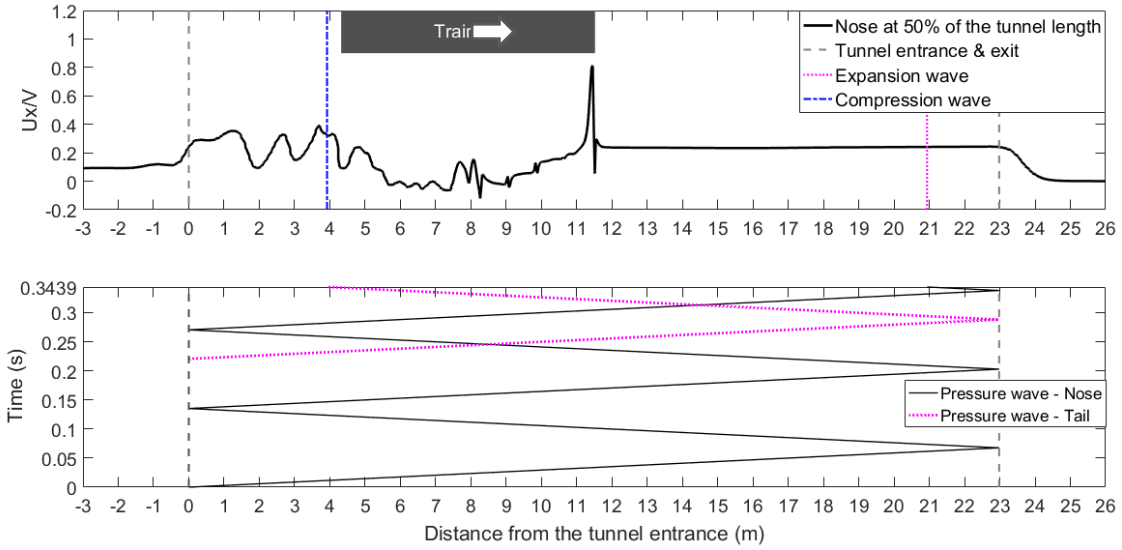

Figure 6.30: Normalised velocity at L9 in relation to the location of the train and pressure waves. The nose enters the tunnel at t=0s.

6.4.6 **Time dependence of velocities**

Figure 6.31 below shows the normalized velocity inside and outside of the tunnel at different snapshots. Outside of the tunnel, the velocities at the exit and entrance are important because of the occurrence of micro-pressure waves and exiting vortex jets respectively.

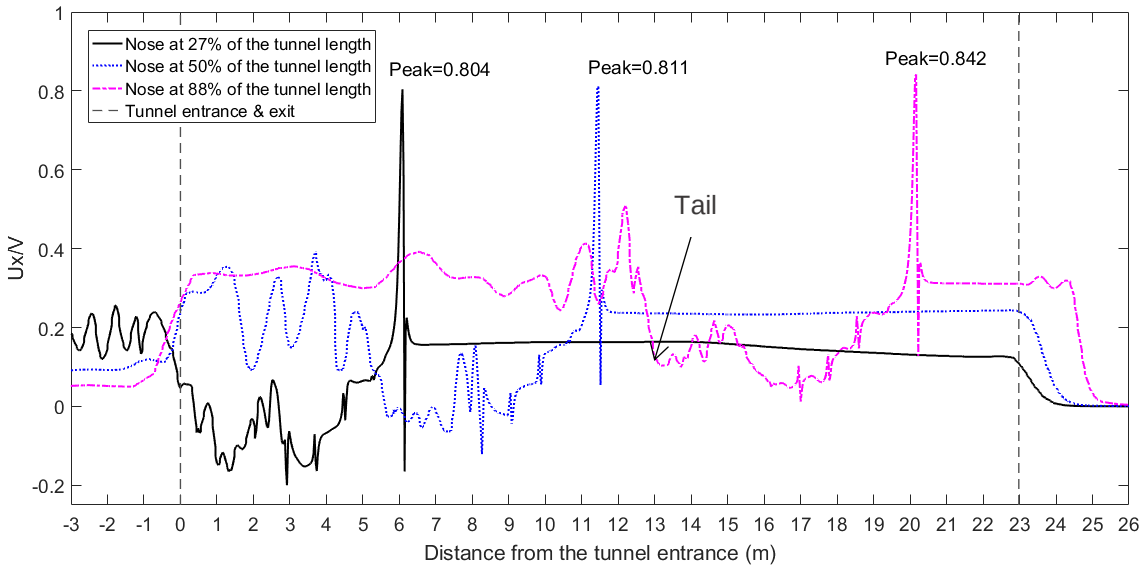

Figure 6.31: Normalized velocity at t=0.1839s, 0.3430s and 0.6038s.

Figure 6.31 shows that as the train moves away from the tunnel entrance, the following effects are observed:

a. The velocity magnitude at the nose increases.
b. The velocity inside the tunnel (ahead and behind the train) increases.
c. The velocity at the exit of the tunnel increases as well as the area of influence outside the tunnel. For example, when the nose is at 88% of the tunnel length, it affects the air as far as 2.5 meters away from the exit. The closer the nose to the exit, the higher the velocity of the displaced air ahead of the train.
d. The air velocity near the tunnel entrance reduces.

The presence of the wake behind the train increases when the train moves away from the entrance, causing flow acceleration inside the tunnel. As a result, this increase in

velocity in the tunnel affects velocities a-c above. On the other side, effect d can be linked to the fact that when the train moves away from the tunnel entrance, the influence of the wake on this region is less significant.

6.4.7 **Effect of nose shape on the velocity field**

This section unravels how the nose shape affects the velocities around the train. Due to noses 1-3 not representing real trains, the comparison is again qualitative. Plane 1 and L9 are analysed, as they are located at the positions where separation is maximum.

Figure 6.32 shows that the most remarkable differences are found between 0 and 1.75m from the nose, at the sides of the locomotive and first wagon. As the nose becomes more rounded (Nose 1), the positive nose peak of U_x reduces significantly. Further rounding of the nose (Noses 2 and 3) converts this peak to negative, because the measurement location is further from separated flow. These negative peaks were observed in section 6.4.3 for measurement lines away from separation. The phenomena observed for L10-L12 for Class 66, are transferred to L9 for noses 1-3, due to the distance between the outer layers of separation and L9 which is increasing. Therefore, during the transition from the Class 66 nose to Nose 3, the outer layers of the separation bubble move towards the train surface.

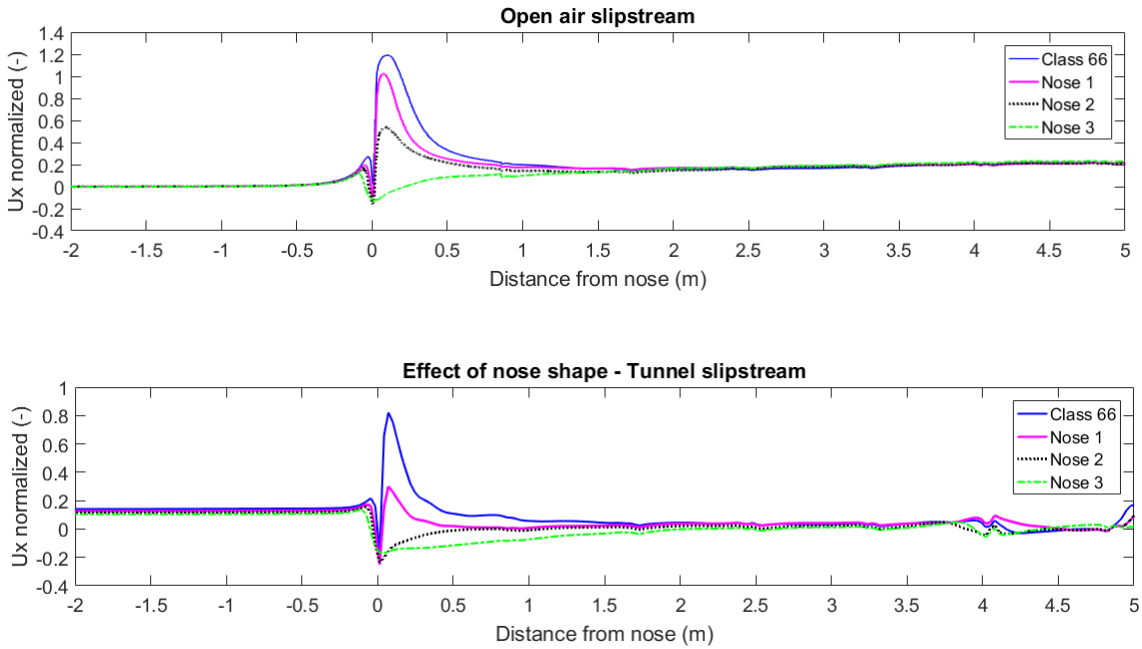

Figure 6.32: Normalized velocity at L9 - 2.25m and 1.75m from the ground and centre of the track respectively (in full scale)

Figure 6.33 suggests that Class 66 produces the highest velocities within the vortex, which then reduce as the shape changes from Nose 1 to 3. Similarly, the velocities in the boundary layer region (behind the bubble) reduce with nose roundness, confirming the findings from Figure 6.32.

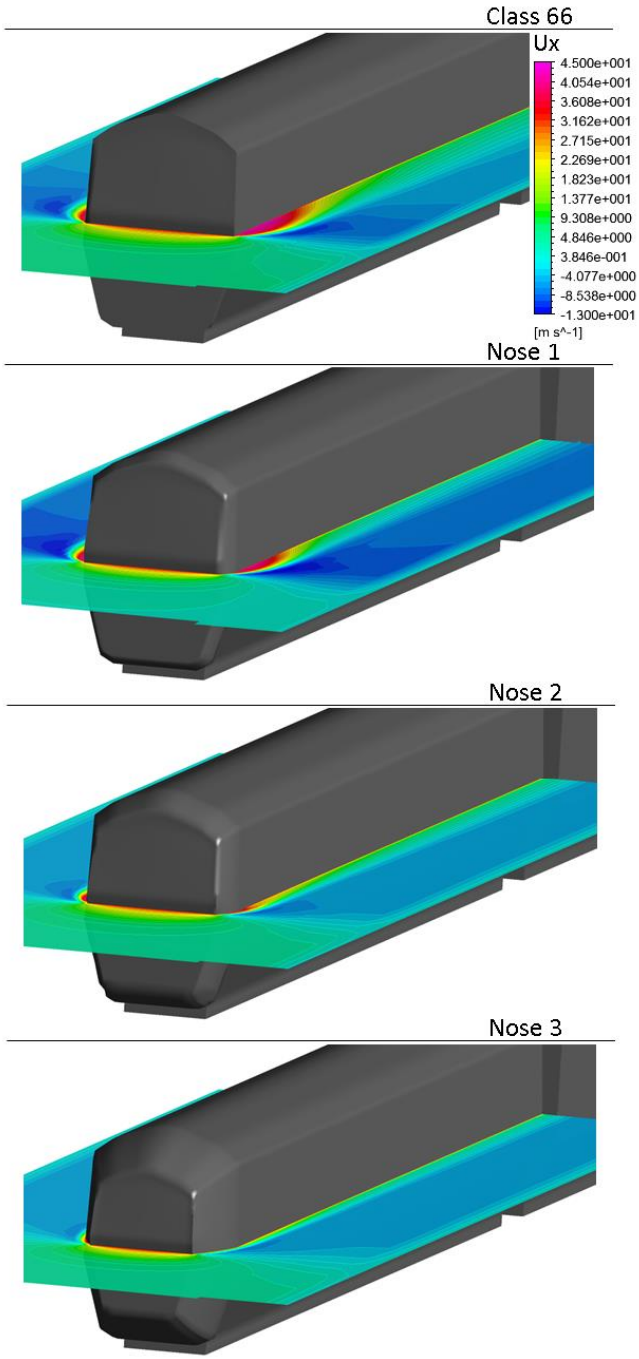

Figure 6.33: Tunnel slipstream. Longitudinal component of velocity contour at Plane 1, 0.09m from the ground (2.25m in full scale)

6.5 Methodological contributions

The results presented in this chapter draw the following conclusions for the numerical methodology adopted, which can be useful for future studies:

a) If the underbody region is represented by a fully filled box, the rail track is not present and the container wagons are represented by square boxes, satisfactory agreement can be obtained with physical experiments which used a representative model.

b) ‘’The gradient of the initial compression wave is calculated accurately while its pressure amplitude is estimated with 10% difference from the experiments. The differences are attributed to differences in the speed of the two models and the CFD model showed very good agreement with experiments.

c) The k-ω SST model predicts the pressure wave amplitude for the remaining of the pressure traces showing satisfactory modelling of the friction effects.

d) The velocity peak at the train nose is captured with 95.5% accuracy while its gradient and length are captured with 100% accuracy’’ (Iliadis et al., 2019, p. 15).

e) To predict the maximum levels of separation and slipstream velocities at the sides, measurements should focus on the widest parts of the locomotive.

Chapter 7

Synthesis of results with 1D analysis

7.1 Introduction

The maximum pressure increase in the tunnel caused by the train entry can be obtained using 1D formulae. The selection of the most suitable formula can be based on the data available for the calculation of coefficients. For this analysis, the nose loss coefficient has been calculated with the formulae from Vardy (1996a), using velocities and pressures from the CFD results. The formula for the prediction of the maximum pressure is provided by the same author in another article (Vardy, 2008). The accuracy of the obtained results is assessed in comparison to the CFD results.

The objective of this analysis is to study whether 1D theory can be used for freight trains with blunt nose. The models' dependence on the nose shape is also investigated.

7.2 Initial compression wave

Figure 7.1 illustrates the pressure changes occurring in the tunnel during the train entry. The two part gradient of the initial pressure rise has been obtained from rounded nose shapes (compared to freight trains). The two gradients are directly related to the nose and main body entry, leading to the maximum pressure in the tunnel.

Equations 25-27 in section 7.3 focus on the prediction of the initial pressure rise Δp_N only, caused by the nose entry. This is due to the fact that the blunt nose of the Class 66 locomotive generates a one-part gradient initial rise. The analysis in this chapter proves that this approach is sufficient for predicting the maximum pressure inside the tunnel for trains with blunt noses, such as the Class 66 locomotive.

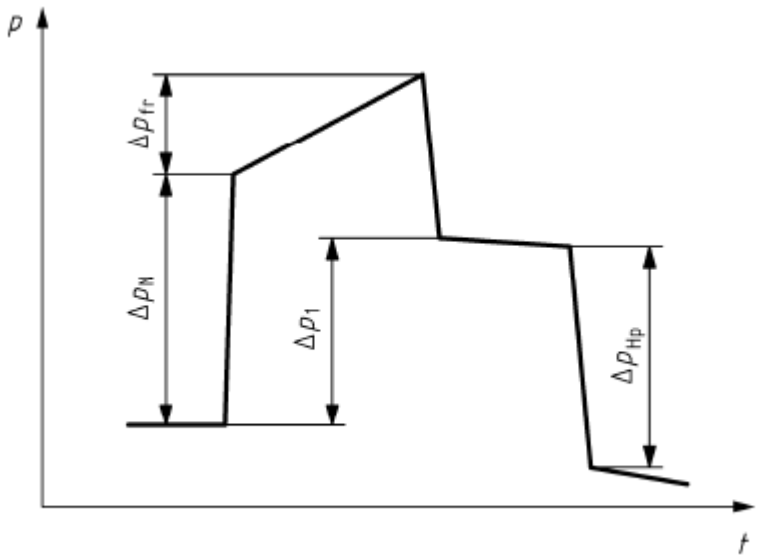

Figure 7.1: The initial pressure rise is composed by a two-part gradient (CEN, 2010)

7.3 Definition of 1D formulae

According to Vardy (2008), the nose wave-front Δp_N associated with the nose entry can be determined using the equation below:

$$\frac{\Delta p_N}{\rho c} = (V_2 - V_0) + \frac{\mathrm{a}}{a}\left[1 - \sqrt{1 + \frac{2a(V_2 - V_0)}{\mathrm{a}}}\right] \tag{25}$$

where

Δp_N *is the pressure rise associated with the nose entry*

V_2 *is the longitudinal component of velocity, relative to the train (location shown in* Figure 7.2*)*

V_0 *is the initial velocity of air inside the tunnel (location shown in* Figure 7.2*)*

a is the speed of sound

α is coefficient defined by eq. (26)

$$\alpha = \frac{1 + k_N}{(1 - \beta^2)} - 1 \tag{26}$$

where

β *is the blockage ratio (train/tunnel cross sectional area)*

k_N *is the pressure loss coefficient at the nose (see eq. 27)*

$$k_N = \left(\frac{P_1 - P_2}{\frac{1}{2}\rho V_2^2}\right) - 2\beta + \beta^2 \tag{27}$$

Figure 7.2 shows the location of the two velocities required to calculate the nose coefficient and pressure rise inside the tunnel. V_2 is relative to the train's velocity and

represents the longitudinal component of velocity. V_0 is the initial air velocity inside the tunnel (longitudinal component), ahead of the wave, at the instant that the train nose has just entered the tunnel. The CFD results have confirmed that the value of V_0 is zero for this train-tunnel case. V_1 is the tunnel velocity ahead of the train and behind the wavefront and it is not used for this calculation. Identical locations are used for pressures P1 and P2.

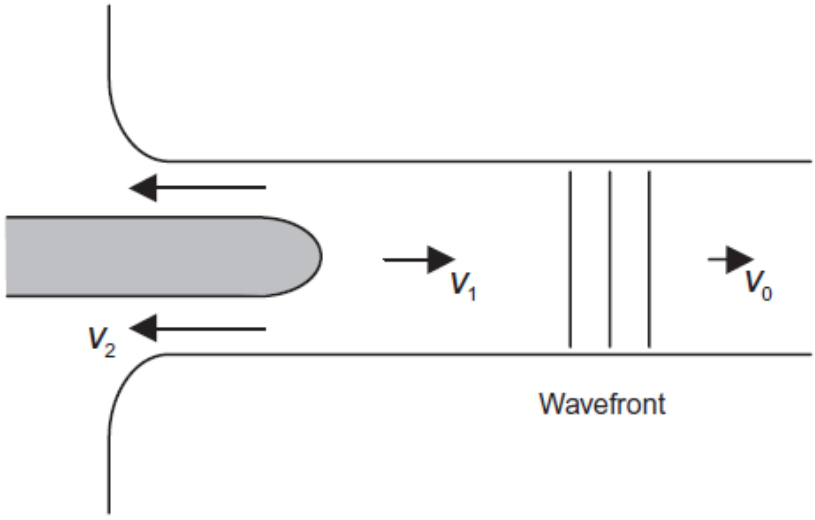

Figure 7.2: Locations 0,1 and 2 are used to extract instantaneous velocities and pressures after the main body entrance (Vardy, 2008).

7.4 Nose coefficient k_N calculation using CFD results

k_N is calculated from eq. (27) and requires the values of V2, P1 and P2 as input. They can be extracted from the CFD simulations at locations 1 and 2 (see Figure 7.2). The instantaneous values are taken when a significant part of the locomotive has entered

the tunnel. For confirmation reasons, a number of instants after the nose entrance have been compared between them, resulting in the same nose coefficient. The data presented in this section is extracted from the instant shown in Figure 7.3, which demonstrates locations 1 and 2 in relation to the train. The use of lines L19 and L20 validates that the flow properties at 1 and 2 are stabilised.

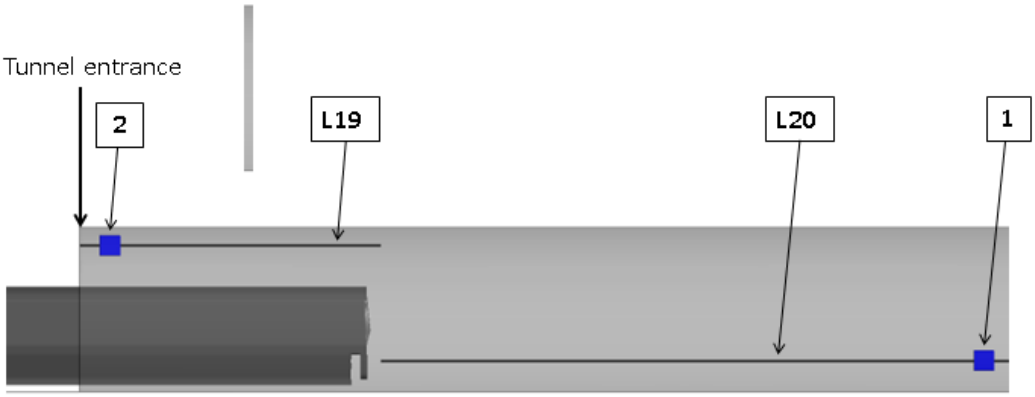

Figure 7.3: Locations 1 and 2 in relation to the train. All velocities and pressures in this chapter have been extracted from this instant.

Figure 7.4 plots the absolute longitudinal component of velocity at L19, which is negative because the air travels towards the tunnel entrance (as shown in Figure 7.2). At point 2, these values can be converted to relative velocities using the formula below:

$$V_2 = V_{tr} - V_2^* \tag{28}$$

where

V_2 *is the relative longitudinal velocity at 2*

V_{tr} is the train speed (33.5 m/s)

V_2^* is the absolute longitudinal velocity at 2 (plotted in Figure 15)

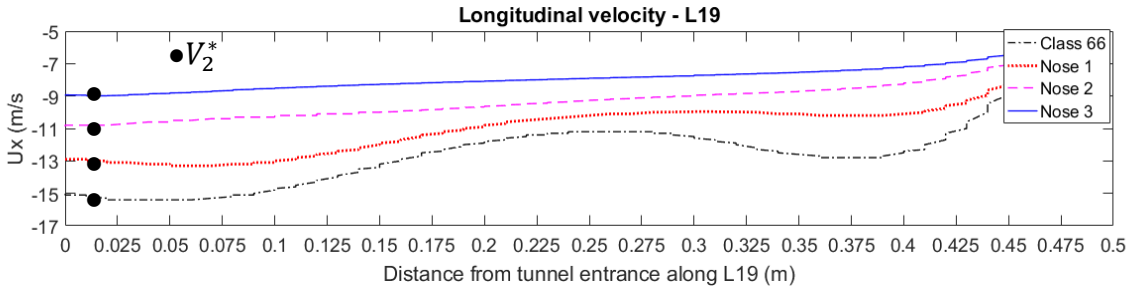

Figure 7.4: Absolute longitudinal velocity V_2^* extracted from CFD results.

In Figure 7.4, V_2^* stabilises near the entrance (origin of the horizontal axis), confirming the selection of location 2. Similarly, Figure 7.5 shows the instantaneous pressures at L19 and L20 where the stabilised values of P1 and P2 are taken from.

The extracted and derived flow properties are summarised in Table 7.1. The use of * next to V_2indicates a relative velocity derived from eq. (28).

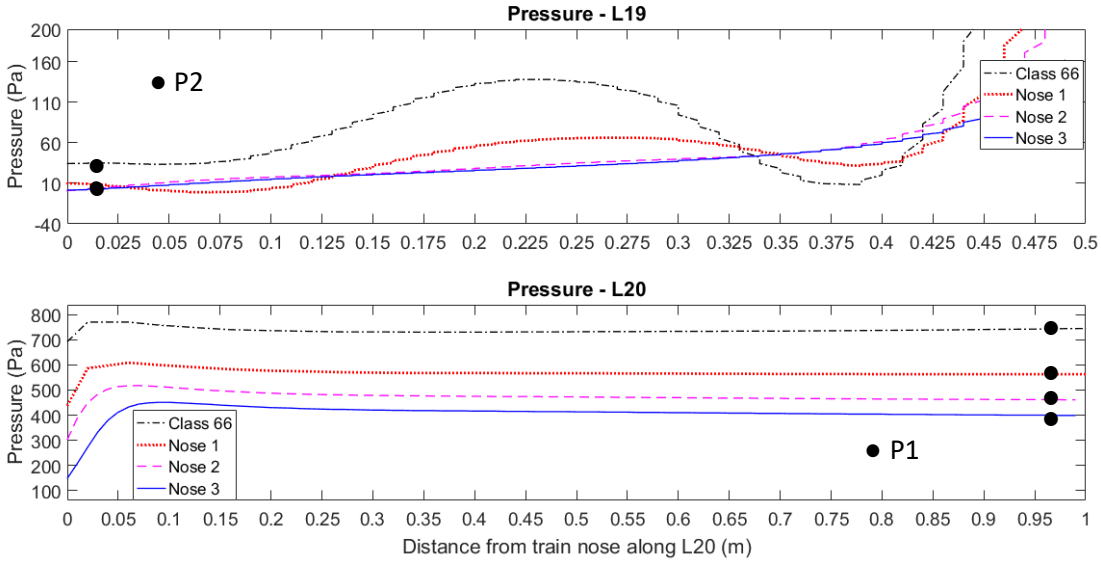

Figure 7.5: Pressures P1 and P2 are extracted from the above graphs. The results were obtained from the CFD simulations.

Table 7.1: Values used for the calculation of k_N

	V_2^* (m/s)	V_2 (m/s)	P_1 (Pa)	P_2 (Pa)	k_N
Class 66	-15.1	48.6	743	34.4	0.1246
Nose 1	-12.9	46.4	563	10	0.0545
Nose 2	-10.8	44.3	462	9.33	0.0119
Nose 3	-8.93	42.43	400	2.17	0.0039

Table 7.1 is in line with literature findings which state that k_N for freight trains is approximately 0.1 and for well-shaped passenger trains approaches 0 (Vardy and Reinke, 1999). The values obtained here can be used by future 1D studies to assist in

the estimation of coefficients. This is a challenging process as it involves the setup of complex physical experiments or numerical simulations.

7.5 Calculation of initial pressure rise using the geometric blockage ratio

The flow properties and coefficients presented in Table 7.1 are substituted into equations 25-27 to calculate Δp_N. The formulae are implemented using the geometric blockage ratio β, as mentioned in literature. An example Matlab program used for these calculations is given in Appendix D. The script requires modification for each nose shape, as the velocities and pressures vary. For all shapes, constant density, speed of sound and zero initial flow in the tunnel are assumed. This approach is expected to have negligible effects on the calculation and to be an accurate representation of the physical conditions.

Table 7.2 presents the results for all nose shapes, including the input values required to compute the initial pressure rise. The disagreement between 1D and CFD results reduces as the nose becomes more rounded. For nose 3, Δp_N is predicted with 90.7% accuracy but this decreases to 57.6% when the shape changes to the blunt nose of the Class 66 locomotive.

Table 7.2: Results from 1D formula and comparison to CFD data

	Input		*Output*	*Comparison with CFD*	
	k_N	Other parameters	Max. pressure (eq. 25) (Pa)	Max. pressure (*CFD) (Pa)*	*Difference*
Class 66	0.1246	ρ=1.23 kg/m^3 a=341 m/s β=0.202 V_{tr}=33.5 m/s V_0= 0 m/s	492	854	42.4%
Nose 1	0.0545		425	644	34.0%
Nose 2	0.0119		384	498	22.9%
Nose 3	0.0039		370	408	9.3%

As discussed before, blunt noses produce a one-part gradient which leads to the maximum pressure inside the tunnel and is caused by the two following events:

- Nose entry
- Separation bubble entry

This is in contrast to more rounded noses for which the initial pressure rise is characterised by a two-part gradient which leads to the maximum pressure inside the tunnel and is attributed to the following:

- Nose entry
- Train main body entry

The above phenomena can be seen in Figure 7.6 which shows the initial compression wave development after the train entry at t=0s.

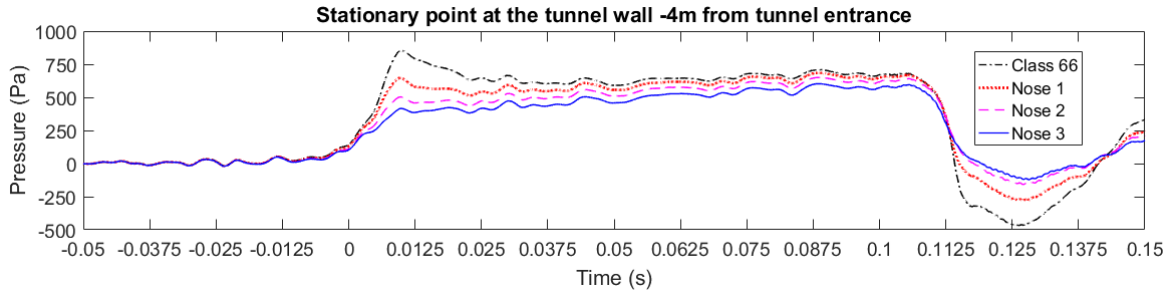

Figure 7.6: Initial pressure wave development for blunt and more rounded noses

Figure 7.7 illustrates that when using the geometric blockage ratio β, equation (25) can predict the maximum pressure rise for rounded noses (graph b) but not for blunt noses (graph a).

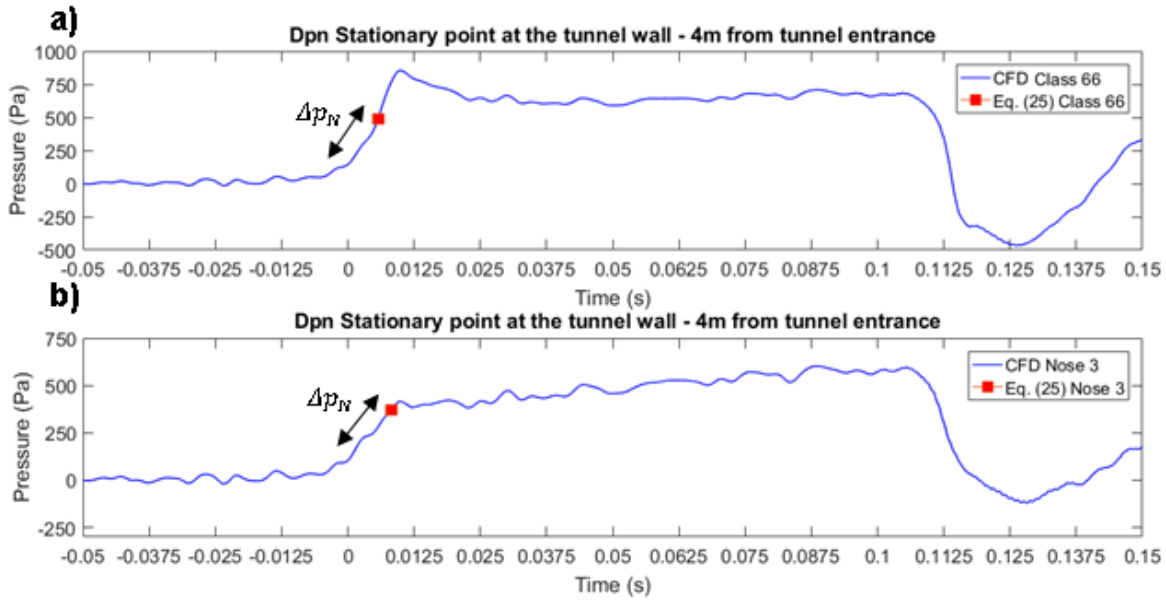

Figure 7.7: Prediction of Δp_N using eq. (25) and comparison with CFD results; a) Class 66 nose; b) Nose 3

In Figure 7.7a, it is believed that Δp_N is predicted accurately using eq. (25), but there is an additional pressure rise associated with the entry of the separation bubble immediately after the nose. The bubble is capable of increasing the blockage area around the train. This effect is not included in the formulae which have been built around passenger trains nose shapes of significantly smaller separation sizes. The findings in section 6.3.5 confirmed that the more rounded the nose, the smaller the bubble size. This effect of the separation bubble on the initial pressure rise is validated in the next section.

7.6 Calculation of initial pressure rise using the effective blockage ratio

In the previous section, the geometric blockage ratio was used on eq. (25). It was shown that blunt noses produce a one-part gradient generated by the nose entry and the entry of the separation bubble behind it. These two events occur subsequently and their contribution to the total rise cannot be detected as they have the same gradient.

Using the geometric blockage ratio provides a very good prediction of the nose entry pressure rise (as confirmed for nose 3), but it cannot account for the bubble entry associated with blunt noses. This leads to the conclusion that a correction must be applied to the use of the formulas and the effective blockage ratio must be used instead. The effective blockage ratio is defined as:

$$\beta^* = \frac{Train\ cross\ section\ area + Separation\ bubble\ cross\ section\ area}{Tunnel\ cross\ section\ area} \qquad (28)$$

The effective cross section area depends on the nose shape which affects the separation bubble size. Therefore, β^* can be calculated for each nose shape using the CFD results, in steps a-c below:

a) Figure 7.8 a) illustrates plane A which is located at the maximum height of the separation bubble, representing the area between the train and the tunnel.
b) Figure 7.8 b) shows the turbulent kinetic energy contours on plane A, indicating the circulation zones around the train.
c) Figure 7.8 c) indicates that by filtering the contours presented in b) based on the turbulent kinetic energy levels, an additional plane (Plane B) can be created. Plane B represents the cross section area outside of the separation bubble, which leads to an effective blockage ratio β^* of 0.399 for Class 66.

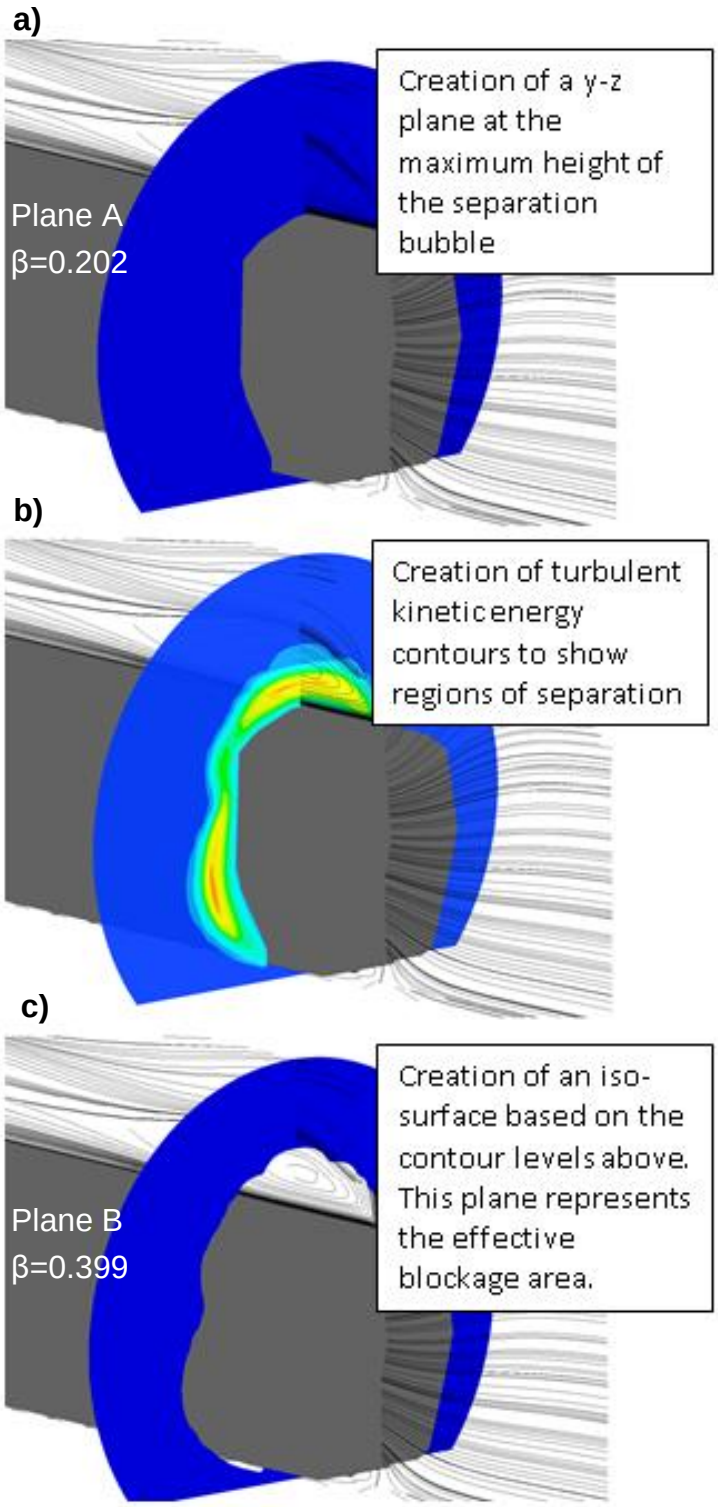

Figure 7.8: Steps for calculating the effective cross sectional area around the Class 66 nose

Figure 7.9: Plane B for Class 66 in blue, representing the effective cross sectional area around the train. The white space represents the separation area around it, at the maximum size of the vortex.

Figure 7.9 presents Plane B from a different view, showing that the separation bubble can occupy cross sectional areas equal to the train's size. At the same time, it confirms previous findings that the maximum separation is found at the centre of the track and middle height of the train.

The Class 66 nose represents the most extreme case among all shapes. Using the three steps described in Figure 7.8, plane B has been generated for all nose shapes. The obtained values are presented in Table 7.3 which proves that the higher the nose bluntness, the most significant the deviation from β^* to β. The disagreement between

eq. (25) and CFD reduces dramatically when using β^* and the maximum pressure inside the tunnel is computed with satisfactory accuracy.

Table 7.3: Calculation of pressure rise using the effective blockage ratio

	Input		***Output***	***Comparison with CFD***	
	k_N	Other parameters	Max. pressure (eq. 25) (Pa)	Max. pressure (*CFD)*	*Difference*
Class 66	0.1246	ρ=1.23 kg/m^3 a=341 m/s V_{tr}=33.5 m/s V_0= 0 m/s	827 $\beta^* = 0.3999$	854	3.2%
Nose 1	0.0545		586 $\beta^* = 0.3280$	644	9.0%
Nose 2	0.0119		453 $\beta^* = 0.2689$	498	15.2%
Nose 3	0.0039		404 $\beta^* = 0.2398$	408	1%

A visual representation of the results is given in Figure 7.10 which shows the agreement between 1D and CFD for the Class 66 locomotive. When Figure 7.10 and Figure 7.7 are combined, the following conclusions can be drawn for the Class 66 nose:

- Using β in eq. (25) can give the nose entry pressure rise Δp_N, which is what the formula is designed to predict.
- Using β^* in eq. (25) can predict both the nose entry pressure rise Δp_N but also the increase associated by the separation bubble entry Δp_{sp}.
- The nose entry is responsible for approximately 42% of the pressure rise and the remaining is caused by the separation bubble entry.

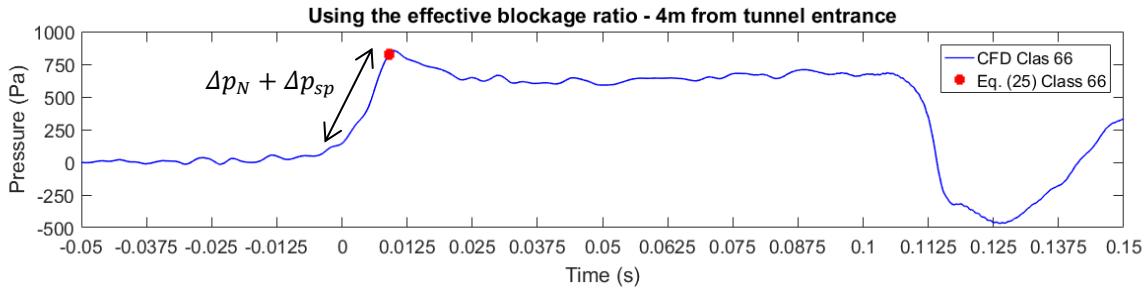

Figure 7.10: Satisfactory prediction of the maximum pressure inside the tunnel using the effective blockage ratio and eq. (25) for the Class 66 nose

7.7 Discussion of 1D analysis

The analysis presented in this chapter combined the CFD results with 1D theory to determine the maximum pressure rise in the tunnel. The implementation of 1D formulae showed that their accuracy depends on the nose bluntness, with best results obtained for round noses.

Current formulae have been designed for relatively round noses which produce a two-part gradient, attributed to the nose and main body entry into the tunnel. The geometric blockage ratio β is used in the 1D equations, which is the ratio of the train to tunnel cross sectional area. On the other side, blunt noses produce a one-part gradient attributed to the large separation bubble just behind the locomotive nose. The analysis suggests that for these cases the blockage ratio calculation should also include the area around the train, occupied by the separation bubble. This is the area of flow circulation which blocks the oncoming air and redirects it to the annulus between the outer layers of the vortex and the tunnel walls.

This study used the turbulent kinetic energy levels obtained from numerical analysis to calculate this area and to derive the effective blockage ratio β^*. Once β is replaced with the effective blockage ratio, 1D formulae can predict can predict the maximum pressure rise for fully loaded trains with blunt nose.

7.8 Methodological contributions

a) For partially loaded trains, the use of 1-D analytical models which focus on the development of the initial compression wave is not recommended. This is based on the fact that the maximum pressure amplitude for this study occurred after the initial wave.
b) For trains with blunt noses (such as freight trains), the area occupied by the separation bubble should be added to the train cross sectional area when calculating the blockage ratio.

Chapter 8

Conclusions and recommendations

8.1 Conclusions - pressure transients

The experimental and numerical results, combined with the 1D analysis conducted in this study, lead to the following novel conclusions for the development of sound waves:

- The Class 66 locomotive has a blunt nose which produces a one-part gradient for the initial compression wave. This phenomenon is reported for the first time and it is different from the two-part gradient observed for more rounded noses. The two-part gradient of rounded noses is attributed to the transition between the front part of the nose and the start of the main body of the locomotive. Blunt noses have no transitional region between these two points. In addition, they have a large separation bubble, which occupies a large cross section area around them, affecting the blockage ratio.

- For partially loaded trains, the maximum pressures can be observed later than the initial compression wave. This is a novel finding and it is in contrast to fully loaded trains which have maximum values during the initial wave. The explanation behind this phenomenon is that the gaps between containers generate low energy pressure waves, which cause additional rises during entry. Thus, for partially loaded trains, analytical models should not be used.
- The gradient of the initial wave for this freight train is significantly steeper and its amplitude larger compared to passenger trains. However, under the current test conditions, compliance with TSI regulations was found for the Class 66 locomotive.
- When implementing 1D analytical models for trains with blunt noses, attention must be paid in the use of blockage ratio. Instead of using the train cross sectional area only, the area occupied by the separation bubble must be added to it.
- ‘’The pressure at the tunnel wall increases whenever a compression wave or the tail passes from a measurement point and decreases when an expansion wave or the nose passes by’’ (Iliadis et al., 2018, p. 11).
- At the tunnel entrance wall, most pressure variations are caused by the exiting vortex around the vehicle towards the entrance and the pressure waves’ arrival at the boundary. As expected, the most remarkable pressure changes occur when the train passes by the entrance wall. The closer the measurement points to the centre of track, the higher the amplitude. Partially loaded trains

were found to cause additional pressure increases whenever an empty wagon passes by the measurement point.

- At the train surface, the highest pressures are observed in the stagnation area (front face), reaching values more than 50% higher than at the tunnel walls. The pressure distribution is uniform at the train front, as no variation was found between the nine pressure taps.
- ‘’The attenuation of the pressure waves is explained by the energy lost due to viscosity, the radiation of the micro-pressure waves and the interference of pressure waves. The waves continue to reflect even after the exit of the tail from the tunnel, until they run out of energy’’ (Iliadis et al., 2018, p. 11).

8.2 Conclusions - separated flow around the train head

The numerical results lead to the following novel conclusions:

- As the train enters the confined space of the tunnel, the separation size reduces by 31% at the sides and 32% at the roof, compared to open air. The presence of tunnel walls causes shrinkage of the separation bubble.
- ‘’The separation bubble is largest at the mid-longitudinal and mid-lateral planes of the train, explained by the extended edges of the locomotive at these regions. Inside the tunnel, at the sides of the train, the longest separation bubble is found at 52% of the train height where it reattaches at 19% of the locomotive length.

- The flow separates again at the rear part of the locomotive (97% of its length) due to the space between wagons. This separation point remains unchanged when the train is inside the tunnel'' (Iliadis et al., 2019, p. 15).
- When changing the nose shape to more rounded, the separation size (length and height of bubble) reduces dramatically. The separation point remains unchanged but reattachment occurs earlier. Both the pressure transients and the velocity field around the train are affected. The former is influenced because the smaller separation bubble results in lower effective blockage ratio.

8.3 Conclusions - velocity field around the train

The conclusions drawn from the analysis of the velocity field around the train are as follows:

- ''The velocity profile along the vertical direction of the separation bubble showed an adverse pressure gradient and backflow of significant strength (130% of the train speed) and identical height of the bubble in open air and inside the tunnel.
- Close to the train side, the nose slipstream velocity peak in open air is 120% of the train speed in open air but reduces by 30% when the train nose is halfway through the tunnel'' (Iliadis et al., 2019, p. 15). This effect can be explained by the tunnel walls which deflect the separated flow around the train and act as additional sources of drag.

- Rounding of the nose can reduce the nose peak significantly, directly linked to the reduced separation size.
- ‘’Inside the tunnel the velocity in the upstream region is significantly increased compared to open air, forming approximately 25% of the nose peak’’ (Iliadis et al., 2019, p. 15).

8.4 Addressing the objectives

- *Plan and develop an experimental methodology for providing the pressure time histories at various locations inside the tunnel, at the entrance portal and train surface.*

The model-scale experiments were performed in line with European Standards using a moving model. Pressure transducers were placed at the tunnel walls, entrance portal and train surface. The experimental results showed adequate repeatability between runs and very good agreement with the numerical simulations. It is firmly believed that this objective has been achieved and the experimental setup was proved suitable for the aim of this study.

- *Create a CAD model which best represents the real geometry and develop a numerical methodology which accurately captures all flow effects (pressure transients, separation and velocity magnitudes) around the train.*

The CAD model was simplified compared to the physical scaled model. Very good agreement with experiments was achieved and the simplifications had no effects on the comparison. The mesh and time-step independent sliding mesh simulations, combined with unsteady RANS modelling were proved to be an effective approach. The amplitude of the initial wave was captured with 90% accuracy and its gradient with 100% accuracy. The open air slipstream velocity was captured with 94% accuracy. The above validations show that the objective of developing a robust numerical methodology has been met, which was a key step that led to further CFD analysis.

- *Investigate the pressure transients generated by the Class 66 locomotive connected to container wagons and unravel how these differ from a passenger train. The compliance of the above effects with current regulations will be presented.*

The pressure gradient of the initial compression for this freight train tested under the current conditions was found to be constant which is different compared to passenger trains. This finding is reported for the first time and led to further analysis using 1D theory. It was found that modifications in the use of formulas for predicting it are required. Under the current tested conditions, the results for the Class 66 locomotive show compliance with TSI requirements.

Therefore, it can be concluded that novel findings were obtained for the development and effects of the pressure waves and this objective has been achieved.

- *Explore the effects of train length, nose shape and loading configuration on the pressure transients using experiments and numerical simulations.*

The effect of the train length was studied and presented no significant impact under the current testing conditions apart from the timing of the pressure waves which changes

The nose shape was investigated using an additional of 3 nose shapes, representing the transition between blunt and rounded shapes. It was confirmed that blunt noses produce a single gradient initial pressure rise while rounded noses produce the typical two-part gradient rise. This has been linked to the large separation bubbles observed for blunt noses, reducing in size with nose roundness.

The effect of loading configuration was explored both experimentally and computationally, representing two separate cases. It was proved that the gaps between wagons generate low energy pressure waves, which cause additional pressure rises. Effectively, the highest pressure inside the tunnel can occur after the initial compression wave which is a very useful finding.

- *Study the tunnel effect on the separated flow around the train nose and analyse it in detail.*

The numerical results gave detailed data about the separated flow size around the front part of the vehicle. Inside the tunnel, the separation bubble is reduced both at the roof and sides. The areas with the longest bubble were identified and explained. A

direct link was found between separation levels and pressure transients, leading to important findings.

- *Analyse the velocity magnitudes around, ahead and behind the train. Show how this differs from open air results.*

It was shown that the velocity peaks at the sides of the train are reduced inside the tunnel, in comparison to open air. The velocity in the upstream region increases as the vehicle approaches the exit. A relationship was observed between the length of separation and peak velocity duration at the nose. Areas with maximum separation length produce the highest velocity magnitudes within the vortex. The above results clearly showed information that were not available in literature and met the requirements of this objective.

- *Use the results obtained in this study to investigate the effectiveness of 1D analytical models in predicting the maximum pressures inside the tunnel, caused by freight trains.*

The nose coefficient was calculated from the CFD results and then inserted into 1D formulae (taken from the literature) to calculate the pressure rise associated with the nose entry. When using the geometric blockage ratio, the initial pressure rise is poorly predicted. To obtain accurate results, the total blockage area should include both the area occupied by the train and the separation bubble around it. Then, very good agreement with 3D experiments and simulations can be achieved.

In addition, it has been shown that 1D models cannot predict the maximum pressure rise for partially loaded trains, as this can be caused by geometric features not accounted for in the formulae (gaps between wagons). Therefore, the analysis described above helped both to explain the experimental and numerical results but also to explore the applicability of 1D theory for freight trains.

8.5 Research limitations

1. Geometry simplifications: Due to geometric simplifications, the underbody of the train and its interaction with the ground were not analysed. However, separation in the underbody is not expected to be as significant as for the upper half of the train due to smaller cross-sectional area.
2. Comparison with full scale data: As reported in the literature review, full scale tests are complex to conduct, especially for tunnel flows. It was not feasible to conduct full scale testing although it could be another source of validation. However, scaled experiments can stand as a validation source due to the fact that they have been performed in line with the suggested methods detailed in CEN.
3. Experimental velocities: Velocity measurements were not performed inside the tunnel due to setup complexity. If Cobra probes (velocity measuring equipment) were placed inside the tunnel, they would be subject to the following limitations: a) uncontrollable position of the probes as they would be enclosed and not easily accessible; b) potential damage to the sealing of the

tunnel after installing an external system to control the position of the probes; this would trigger dissipation of the pressure wave as high pressure from the waves would escape outside; c) potential effect of the probes to the total blockage area. It must be mentioned however that the open air velocities were validated with experiments from a previous study and showed satisfactory agreement.

4. Flow visualization: This requires a clear/transparent tunnel and the use of smoke or PIV system. From an experimental point of view, visual information about the flow could help in identifying the causes behind the results. However, the numerical simulations provided enough visual information to cover this limitation and unpacked important findings.

8.6 Future research directions

1. Loading configuration: Future research could focus on 1D models for calculating the additional pressure rise associated with the gaps between empty wagons (potentially by considering a superposition of multiple 1D trains). The relevance of current TSI regulations needs to be examined as current limits focus on the initial compression wave.
2. Nose shape improvement: The current study analysed an existing freight train design, including modified nose shapes. It is believed that future research could propose realistic nose shapes that produce a) shorter separation length over the roof and sides; b) lower stagnation pressures at the locomotive front;

and c) lower velocities around the train. Mechanisms which achieve separation reduction would be of interest (either fitted to the tunnel or train). All of the above will eventually result in more efficient and safer freight trains in tunnels.

3. Effective blockage ratio: Future research could focus on calculating the effective blockage ratio without the use of CFD (i.e. by using the drag coefficient) and then insert it into 1D models.
4. Full scale tests: Full scale tunnel velocities and pressure histories could validate the scaled experimental and numerical results obtained in this study.
5. Structural loads: It is suggested that future research could focus on the structural loads created by aerodynamic forces. Additional analysis could investigate whether the recorded velocities at the sides of the train have the potential to displace objects or people. Such studies can be conducted using the results presented in this thesis.
6. Vibration: Future studies could conduct analysis on the vibration levels arising from flow separation and the occurrence of pressure waves. The results presented in this thesis have pointed the areas where the above phenomena are expected to be intense. A vibration study could illustrate useful information about the stability of the train.

Chapter 9

References

Ansys 2015a. CFX Modelling Guide. *Release 16.2.* SAS IP, Inc.

Ansys 2015b. ICEM CFD User manual. *Release 16.2.* SAS IP, Inc.

Arakeri, V. H. & Acosta, A. J. 1973. Viscous effects in the inception of cavitaton on axisymmetric bodies. *Journal of Fluids Engineering,* 95**,** 519-527.

Araujo, P. & Rezende, A. 2017. Comparison of turbulence models in the flow over a backward-facing step. *International Journal of Engineering Research & Science,* 3.

Auvity, B. & Bellenoue, M. Vortex structure generated by a train-tunnel entry near the portal. 8th Intl Symp. on Flow Visualization, Sorrento, 1998 Sorento. 1-4.

Auvity, B. & Kageyama, T. 1996. Etude experimentale et numerique de l'onde de compression generee par l'entree d'un train dans un tunnel. *Comptes Rendus,*

Academie des Sciences, Serie II: Mecanique, Physique, Chimie, Astronomie, 323**,** 87-94.

Baker, C. 2010. The flow around high speed trains. *Journal of Wind Engineering and Industrial Aerodynamics,* 98**,** 277-298.

Baker, C. 2014 a. A review of train aerodynamics, Part 2: Applications. *The Aeronautical Journal,* 118.

Baker, C. 2014 b. A review of train aerodynamics Part 1: Fundamentals. *The Aeronautical Journal,* 118.

Baker, C., Dalley, S. J., Johnson, T., Quinn, A. & Wright, N. G. 2001. The slipstream and wake of a high-speed train. *Proceedings of the Institution of Mechanical Engineers, Part F: Journal of Rail and Rapid Transit,* 215**,** 83-99.

Baker, C., Jordan, S., Gilbert, T., Quinn, A., Sterling, M., Johnson, T. & Lane, J. 2014. Transient aerodynamic pressures and forces on trackside and overhead structures due to passing trains. Part 1: Model-scale experiments.

Proceedings of the Institution of Mechanical Engineers, Part F: Journal of Rail and Rapid Transit, 228**,** 37-70.

Bardina, J. E., Huang, P. G. & Coakley, T. J. 1997. Turbulence modeling validation, testing and development. *NASA Technical Memorandum 110446*.

Baron, A., Molteni, P. & Vigevano, L. 2006. High-speed trains: Prediction of micro-pressure wave radiation from tunnel portal. *Journal of Sound and Vibration,* 296**,** 59-72.

Bearman, P. W. 1980. Review - Bluff Body Flows Applicable to Vehicle Aerodynamics. *Journal of Fluids Engineering,* 102**,** 265-274.

Bearman, P. W. & Obasaju, E. D. 1982. An experimental study of pressure fluctuations on fixed and oscillating square-section cylinders. *Journal of Fluid Mechanics,* 119**,** 297-321.

Bell, J. R., Burton, D., Thomson, M., Herbst, A. & Sheridan, J. 2014. Wind tunnel analysis of the slipstream and wake of a high speed train. *Journal of Wind Engineering and Industrial Aerodynamics,* 134**,** 122-138.

Bellenoue, M., Moriniere, V. & Kageyama, T. 2002. Experimental 3-D simulation of the compression wave due to train-tunnel entry. *Journal of Fluids and Structures,* 16**,** 581-595.

Blazek, J. 2015. *Computational Fluid Dynamics: Principles and Applications; Chapter 3 - Principles of Solution of the Governing Equations*, Butterworth-Heinemann.

Bokhortst, E., Kat, R., Elsinga, G. E. & Lentink, D. 2015. Feather roughness reduces flow separation during low Reynolds number glides of swifts. *Journal of Experimental Biology,* 218**,** 3179-3191.

Bosch, G., Kappler, M. & Rodi, W. 1996. Experiments on the flow past a square cylinder placed near a wall. 13**,** 292-305.

Bushnell, D. M. & Moore, K. J. 1991. Drag Reduction in Nature. *Annual Review of Fluid Mechanics,* 23**,** 65-79.

Cen 2003. Railway applications - Aerodynamics. Part 3: Aerodynamics in tunnels. BSI Standards Limited.

Cen 2010. EN 14067-5: 2006+A1: 2010 Railway Applications - Aerodynamics Part 5: Requirements and test procedures for aerodynamics in tunnels. CEN.

Cen 2013. Railway applications - Aerodynamics - Part 4: Requirements and test procedures for aerodynamics on open track. BSI Standards Limited.

Chang, P. K. 1961. Separation of flow. *Journal of The Franklin Institute,* 272.

Choi, J. K. & Kim, K. H. 2014. Effects of nose shape and tunnel cross-sectional area on aerodynamic drag of train traveling in tunnels. *Tunnelling and Underground Space Technology,* 41**,** 62-73.

Curie, I. G. 2012. *Fundamental Mechanics of Fluids*, Taylor & Francis Inc, CRC Press Inc.

Derakhshandeh, J. F. & Mahbud Alam, M. 2019. A review of bluff body wakes. *Ocean Engineering,* 182**,** 475-488.

Diwan, S. S. & Ramesh, O. N. 2007. Laminar separation bubbles: Dynamics and control. *Sadhana,* 32**,** 103-109.

Dorigatti, F. 2013. *Rail vehicles in crosswinds: analysis of steady and unsteady aerodynamic effects through static and moving model tests.* Ph.D, University of Birmingham.

Driver, D. M., Seegmiller, H. L. & Marvin, J. G. 1987. Time-dependent behavior of a reattaching shear layer. *AIAA Journal,* 25**,** 914-919.

First-Sensor 2013. HCLA Series Pressure Sensors. Technical Datasheet.

Flynn, D., Hemida, H. & Baker, C. 2016. On the effect of crosswinds on the slipstream of a freight train and associated effects. *Journal of Wind Engineering and Industrial Aerodynamics,* 156**,** 14-28.

Flynn, D., Hemida, H., Soper, D. & Baker, C. 2014. Detacched-eddy simulation of the slipstream of an operational freight train. *Journal of Wind Engineering and Industrial Aerodynamics,* 132**,** 1-12.

Gilbert, T., Baker, C. & Quinn, A. 2013. Aerodynamic pressures around high-speed trains: the transition from unconfined to enclosed spaces. *Proceedings of the Institution of Mechanical Engineers, Part F: Journal of Rail and Rapid Transit,* 227**,** 609-622.

Hemida, H., Baker, C. & Gao, G. 2012. The calculation of train slipstreams using large-eddy simulation. *Proceedings of the Institution of Mechanical Engineers, Part F: Journal of Rail and Rapid Transit,* 228**,** 25-36.

Hemida, H. & Krajnovic, S. 2010. LES study of the influence of the nose shape and yaw angles on flow structures around trains. *Journal of Wind Engineering and Industrial Aerodynamics,* 98**,** 34-46.

Howe, M. 2014. *Acoustics and Aerodynamic Sound*, Cambridge University Press.

Howe, M. S. 1998a. The Compression Wave Produced by a High-Speed Train Entering a Tunnel. *Proceedings: Mathematical, Physical and Engineering Sciences,* 454**,** 1523-1534.

Howe, M. S. 1998b. Mach number depedence of the compression wave generated by a high speed train entering a tunnel. *Journal of Sound and Vibration,* 212**,** 23-36.

Howe, M. S. 1999. Review of the theory of the compression wave generated when a high-speed train enters a tunnel. *Proc IMechE, Part F: J Rail and Rapid Transit,* 213**,** 89-104.

Howe , M. S., Iida, M., Fukuda, T. & Maeda, T. 2000. Theoretical and experimental investigation of the compression wave generated by a train entering a tunnel with a flared portal. *Journal of Fluid Mechanics,* 425**,** 111-132.

Huang, Y., Hong, T. H. & Kim, C. N. 2012. A numerical simulation of train induced unsteady airflow in a tunnel of Seoul subway. *Journal of Mechanical Science and Technology,* 26**,** 785-792.

Iliadis, P., Hemida, H., Soper, D. & Baker, C. 2019. Numerical simulations of the separated flow around a freight train passing through a tunnel using the sliding mesh technique. *Proceedings of the Institution of Mechanical Engineers, Part F: Journal of Rail and Rapid Transit*.

Iliadis, P., Soper, D., Baker, C. & Hemida, H. 2018. Experimental investigation of the aerodynamics of a freight train passing through a tunnel using a moving model. *Proceedings of the Institution of Mechanical Engineers, Part F: Journal of Rail and Rapid Transit*.

Irwin, H. P. A. H., Cooper, K. R. & Girard, R. 1979. Correction of distortion effects caused by tubing systems in measurements of fluctuating pressures. *Journal of Wind Engineering and Industrial Aerodynamics,* 5**,** 93-107.

Jahanmiri, M. 2011. Laminar separation bubble: Its structure, dynamics and control. Goteborg, Sweden: Department of Applied Mechanics, Chalmers University of Technology.

Johnson, T. & Dalley, S. 2002. 1/25 Scale Moving Model Tests for the TRANSAERO Project. In: Schulte-Werning B., Grégoire R., Malfatti A., Matschke G. (eds) TRANSAERO — A European Initiative on Transient Aerodynamics for Railway System Optimisation. *Notes on Numerical Fluid Mechanics and Multidisciplinary Design (NNFM),* 79**,** 123-135.

Jovic, S. 1996. An experimental study of a separated/reattached flow behind a backward-facing step. *NASA Technical Memorandum 110384.* Eloret Institute, Ames Research Center, Moffet Field, California: NASA.

Khayrullina, A., Blocken, B., Janssen, W. & Straathof, J. 2015. CFD simulation of train aerodynamics: Train-induced wind conditions at an underground railroad passenger platform. *Journal of Wind Engineering and Industrial Aerodynamics,* 139**,** 100-110.

Kikuchi, K., Lida, M. & Fukuda, T. 2011. Optimization of train nose shape for reducing micro-pressure wave radiated from tunnel exit. *Journal of Low Frequency Noise, Vibration and Active Control,* 30**,** 1-19.

Kim, J. & Moin, P. 1985. Application of a fractional-step method to incompressible Navier-Stokes equations. *Journal of Computational Physics,* 59**,** 308-323.

Kiya, M. & Sasaki, K. 1983. Free-stream turbulence effects on a separation bubble. *Journal of Wind Engineering and Industrial Aerodynamics,* 14**,** 375-386.

Kwon, H. B., Kim, T. Y., Lee, D. H. & Kim, M. S. 2006. Numerical simulation of unsteady compressible flows induced by a high-speed train passing through a tunnel. *Proceedings of the Institution of Mechanical Engineers, Part F: Journal of Rail and Rapid Transit,* 217**,** 111-124.

Li, X.-H., Deng, J., Chen, D.-W., Xie, F.-F. & Zheng, Y. 2011. Unsteady simulation for a high-speed train entering a tunnel. *Journal of Zhejiang University SCIENCE A,* 12**,** 957-963.

Maeda, T. 1999. Railway technology today 9: Protecting the trackside environment. *Japan Railway & Transport Review,* 22**,** 48-57.

Maeda, T., Matsumura, T., Iida, M., Nakatani, K. & Uchida, K. Effect of shape of train nose on compression wave generated by train entering tunnel. Proceedings of the International Conference on Speedup Technology for Railway and Maglev Vehicles, 1993 Yokohama, Japan. Japan Society for Mechanical Engineers, 315-319.

Mechel, M. P. 2008. *Formulas of Acoustics*, Springer-Verlag Berlin Heidelberg.

Mei, Y. 2013. A Generalized Numerical Simulation Method for Pressure Waves Generated by High-Speed Trains Passing through Tunnels. *Advances in Structural Engineering,* 16**,** 1427-1436.

Moussaed, C., Salvetti, M., Wornom, S., Koobus, B. & Dervieux, A. 2014. Simulation of the flow past a circular cylinder in the supercritical regime by blending RANS and variational-multiscale LES models. *Journal of Fluids and Structures,* 47**,** 114-123.

Ndt. nd. *Ultrasound - Attenuation of Sound Waves* [Online]. [Accessed 28/10 2018].

Neumann, J. On time-dependent behaviour of controlled turbulent flow with separation and reattachment. PAMM Proceedings in Applied Mathematics and Mechanics 3, 2003. 44-47.

Norris, S. E. 2000. *A Parallel Navier Stokes Solver for Natural Convection and Free Surface Flow.* Ph.D, University of Sydney.

Novak, J. Single train passing through a tunnel. Proceedings of the European conference on computational fluid dynamics,, 2006 TU Delft, Netherlands. European conference on Computational Fluid Dynamics.

Ota, T. & Kon, N. 1979. Heat transfer in the separated and reattached flow over blunt flat plates —Effects of nose shape. *International Journal of Heat and Mass Transfer,* 22**,** 197-206.

Ozgoren, M. 2006. Flow structure in the downstream of square and circular cylinders. *Flow Measurement and Instrumentation,* 17**,** 225-235.

Quinn, A., Hayward, M., Baker, C. J., Schmid, F., Priest, J. A. & Powrie, W. 2010. A full-scale experimental and modelling study of ballast flight under high-speed trains.

Proceedings of the Institution of Mechanical Engineers, Part F: Journal of Rail and Rapid Transit, 224**,** 61-74.

Raib 2007. Rail Accident Report: Locomotive runaway near East Didsbury 27 August 2006. Department of Transport.

Rety, J. M. & Gregoire, R. 2002. Numerical Investigation of Tunnel Extensions Attenuating the Pressure Gradient Generated by a Train Entering a Tunnel. *TRANSAERO — A European Initiative on Transient Aerodynamics for Railway System Optimisation. Notes on Numerical Fluid Mechanics and Multidisciplinary Design (NNFM),* 79**,** 239-248.

Ricco, P., Barron, A. & Molteni, P. 2007. Nature of pressure waves induced by a high-speed train travelling through a tunnel. *Journal of Wind Engineering and Industrial Aerodynamics,* 95**,** 781-808.

Rigby, P. R. 1993. Survey of air turbulence for transit vans carried on carflats, and the effect on pushchairs.: British Rail Research Report LR AER 072.

Roshko, A. 1993. Perspectives on Bluff Body Aerodynamics. *Journal of Wind Engineering and Industrial Aerodynamics,* 49**,** 79-100.

Sajben, M. 1970. Fluid mechanics of train-tunnel systems in unsteady motion. *AIAA* 9**,** 1538-1545.

Samson, A., Sarkar, S. & Anand, K. 2012. Experimental investigation of a separation bubble on a flat plate with semi-circular leading edge for different Reynolds numbers. *9th International Conference on Heat Transfer, Fluid Mechanics and Thermodynamics.* Malta.

Schewe, G. 2001. Reynolds-number effects in flow around more-or-less bluff bodies. *Journal of Wind Engineering and Industrial Aerodynamics,* 89**,** 1267-1289.

Sheard, G. J., Thomson, M. C. & Hourigan, K. 2003. From spheres to circular cylinders: the stability and flow structures of bluff ring wakes. *Journal of Fluid Mechanics,* 492**,** 147-180.

Shin, C.-H. & Park, W.-G. 2003. Numerical study of flow characteristics of the high speed train entering into a tunnel. *Mechanics Research Communications,* 30**,** 287-296.

Singh, N. K. & Sarkar, S. 2011. DNS of a Laminar Separation Bubble. *International Journal of Mechanical and Mechatronics Engineering,* 5.

Soper, D. 2014. *The aerodynamics of a container freight train.* Ph.D, University of Birmingham.

Soper, D., Baker, C. & Sterling, M. 2014. Experimental investigation of the slipstream develoment around a container freight train using a moving model facility. *Journal of Wind Engineering and Industrial Aerodynamics,* 135**,** 105-117.

Soper, D., Baker, C. & Sterling, M. 2015. An experimental investigation to assess the influence of container loading configuration on the effects of a crosswind on a container freight train. *Journal of Wind Engineering and Industrial Aerodynamics,* 145**,** 304-317.

Sterling, M., Baker, C., Jordan, S. C. & Johnson, T. 2008. A study of the slipstream of high speed passenger trains and freight trains. *Proceedings of the Institution of Mechanical Engineers, Part F: Journal of Rail and Rapid Transit* 222**,** 177-193.

Sturm, H., Dumstorff, G., Busche, P., Westermann, D. & Lang, W. 2012. Boundary layer separation and reattachment detection on airfoils by thermal flow sensors. *Sensors,* 12**,** 14292-14306.

Suzuki, M. 1996. Aerodynamical studies of the vibration of a trai in a tunnel. RTRI Report, Special No. 8.

Temple, J. & Johnson, T. 2008. Effective Management of Risk from Slipstream Effects at Trackside and Platforms. *Technical Report: A Report Produced for Rail Safety and Standards Board.*

TSI 2014. Commission Regulation (EU) No 1302/2014 2 of 18 November 2014 concerning a technical specification for interoperability relating to the 'rolling stock - locomotives and passenger rolling stock' subsystem of the rail system in the European Union. *In:* COMMISSION, E. (ed.). Official Journal of the European Union.

UNSW 2010. Acoustic impedance, intensity and power, The University of New South Wales.

Vardy, A. 2008. Generation and alleviation of sonic booms. *Engineering and Computational Mechanics,* 161**,** 107-119.

Vardy, A. E. 1996a. Aerodynamic drag on trains in tunnels Part 1: Synthesis and definitions. *Proceedings of the Institution of Mechanical Engineers Part F Journal of Rail and Rapid Transit,* 210**,** 29-38.

Vardy, A. E. 1996b. Aerodynamic drag on trains in tunnels: Part 2: Prediction and validation. *Proceedings of the Institution of Mechanical Engineers Part F Journal of Rail and Rapid Transit,* 210**,** 39-49.

Vardy, A. E. & Reinke, P. 1999. Estimation of train resistance coefficients in tunnels from measurements during routine operation. *Proceedings of the Institution of Mechanical Engineers, Part F: Journal of Rail and Rapid Transit,* 213**,** 71-87.

Wang, S., Avadiar, T., Thomson, M. & Burton, D. 2019. Effect of moving ground on the aerodynamics of a generic automotive model: The DrivAer-Estate. *Journal of Wind Engineering and Industrial Aerodynamics,* 195.

William-Louis, M. & Tournier, C. 2005. A wave signature based method for the prediction of pressure transients in railway tunnels. *Journal of Wind Engineering and Industrial Aerodynamics,* 93**,** 521-531.

Wolf, C. C. 2013. *The subsonic Near-Wake of Bluff Bodies.* Ph.D, University of Aachen.

Woods, W. A. & Pope, C. W. 1981. A generalized flow prediction metthod for the unsteady flow generated by a train in a single-track tunnel. *Journal of Wind Engineering and Industrial Aerodynamics* 7**,** 331-360.

Yoon, T. S., Lee, S., Hwang, H. & Lee, D. H. 2001. Prediction and validation on the sonic boom by a high-speed train entering a tunnel. *Journal of Sound and vibration,* 247**,** 195-211.

Zhang, L., Yang, M., Liang , X. & Zhang , J. 2017. Oblique tunnel portal effects on train and tunnel aerodynamics based on moving model tests. *Journal of Wind Engineering and Industrial Aerodynamics,* 167**,** 128-139.

Appendix A: Geometry simplifications

Figure A-1 shows the following:

a) Full scale Class 66 locomotive of which the drawings have been used to build the models for this study.
b) simplified physical model scaled at 1/25th
c) simplified CAD model scaled at 1/25th

The CAD model shown in the lower part of the figure has additional simplifications compared to the scaled physical model in the middle. However, it has been proved that these simplifications do not affect the overall results, as the cross section area and the nose shape have been retained.

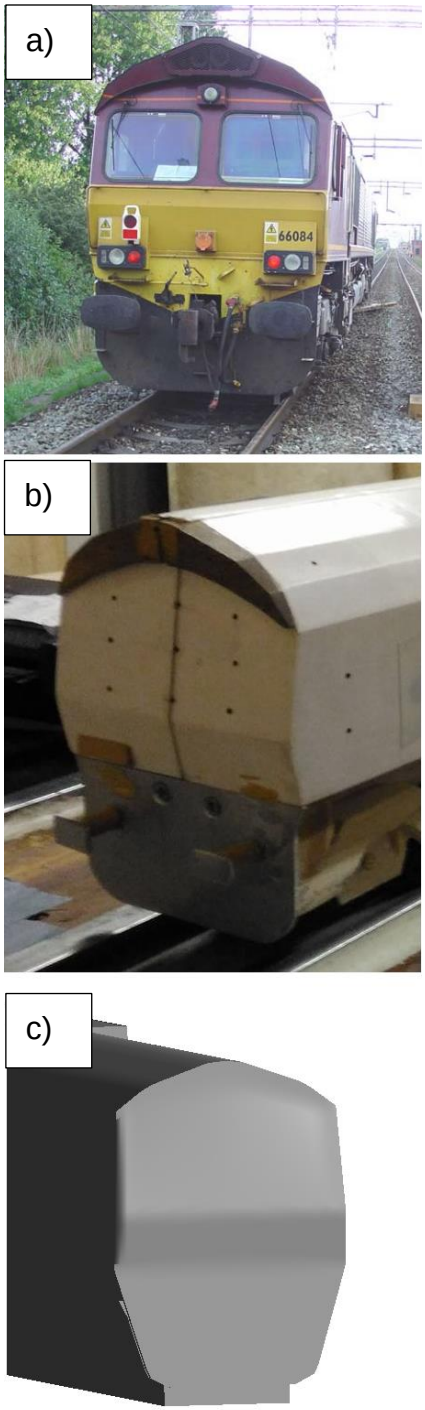

Figure A- 1: a) Front view of Class 66 locomotive, adapted from (RAIB, 2007) ©Crown; b) Front part of the simplified experimental model used at the TRAIN Rig; c) Simplified CAD model used for the CFD simulations

Appendix B: Experiments: measuring equipment

The figures below illustrate the measuring equipment used during the model-scale experiments. The equipment shown is:

1. Sixteen channel data logger for stationary measurements at the tunnel and entrance walls (2 of them were used in total).
2. Pressure sensors attached to the entrance wall
3. Pressure sensors attached to the tunnel walls

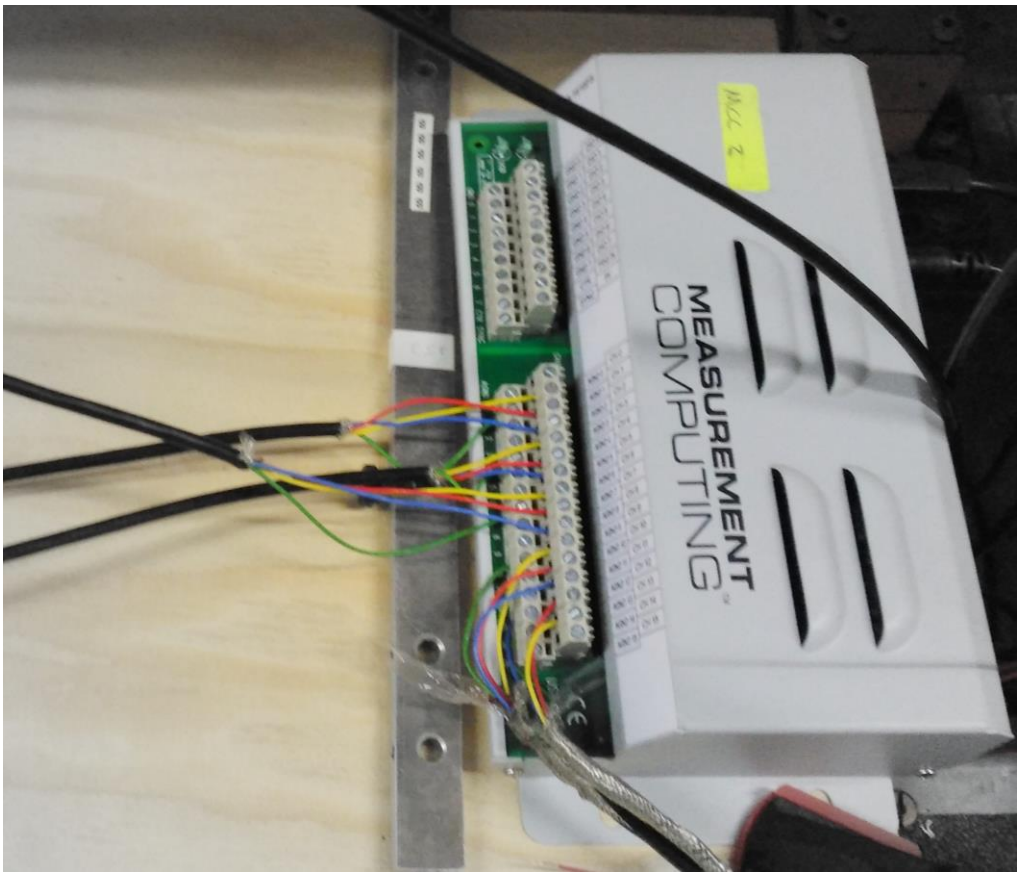

Figure B- 1: Data logger with 16 channels used for stationary points measurements

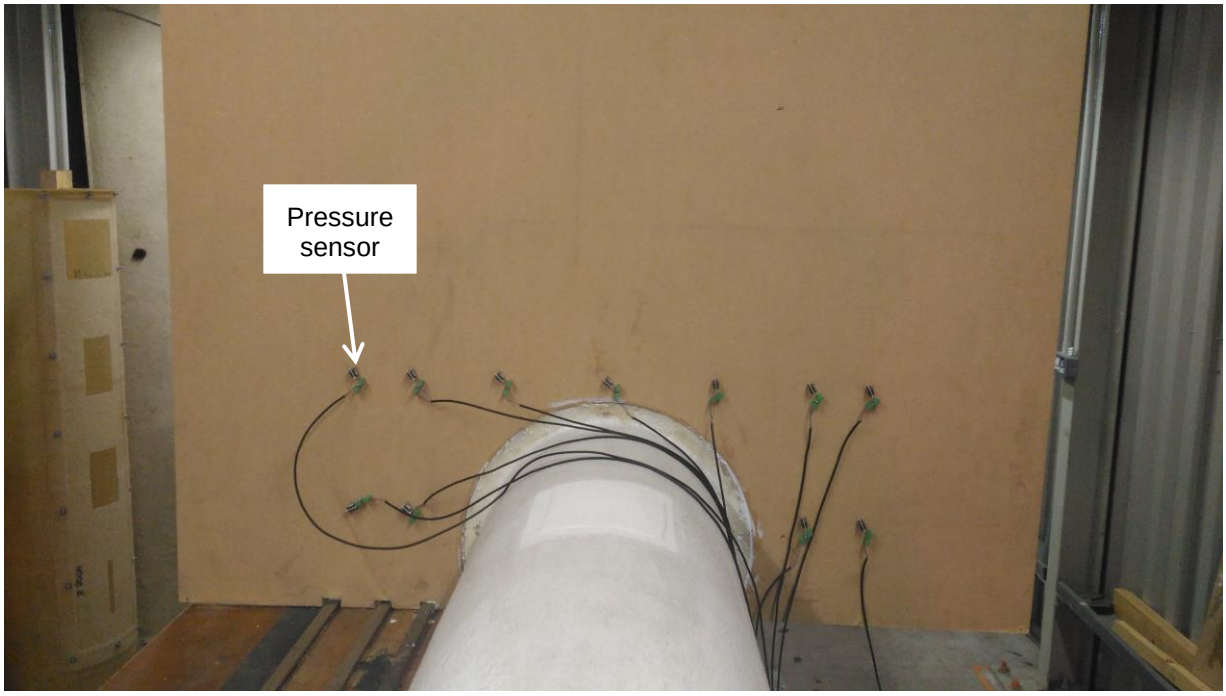

Figure B- 2: Back view of the 11 pressure sensors attached to the entrance wall

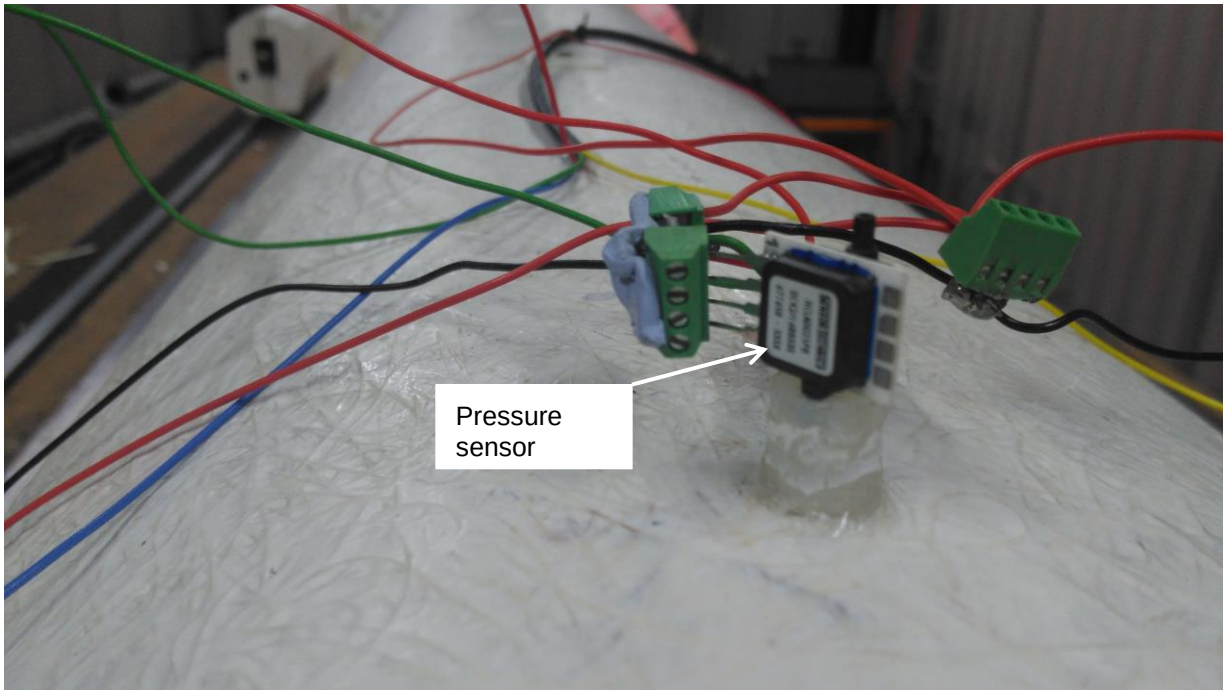

Figure B- 3: Pressure sensor attached to the tunnel walls

Appendix C: CFD: blocking strategy for structured mesh

Figures C-1 and C-2 show the blocks' distribution in the moving and stationary domain respectively. In Figure C-1, the blocks in the centre of the domain represent the areas ahead and behind the train, as the solid volume of the train does not contain blocks. In Figure C-2, the blocks shown are located at the pre-entrance and post-exit domain. The solid lines in the both figures illustrate the geometry boundaries.

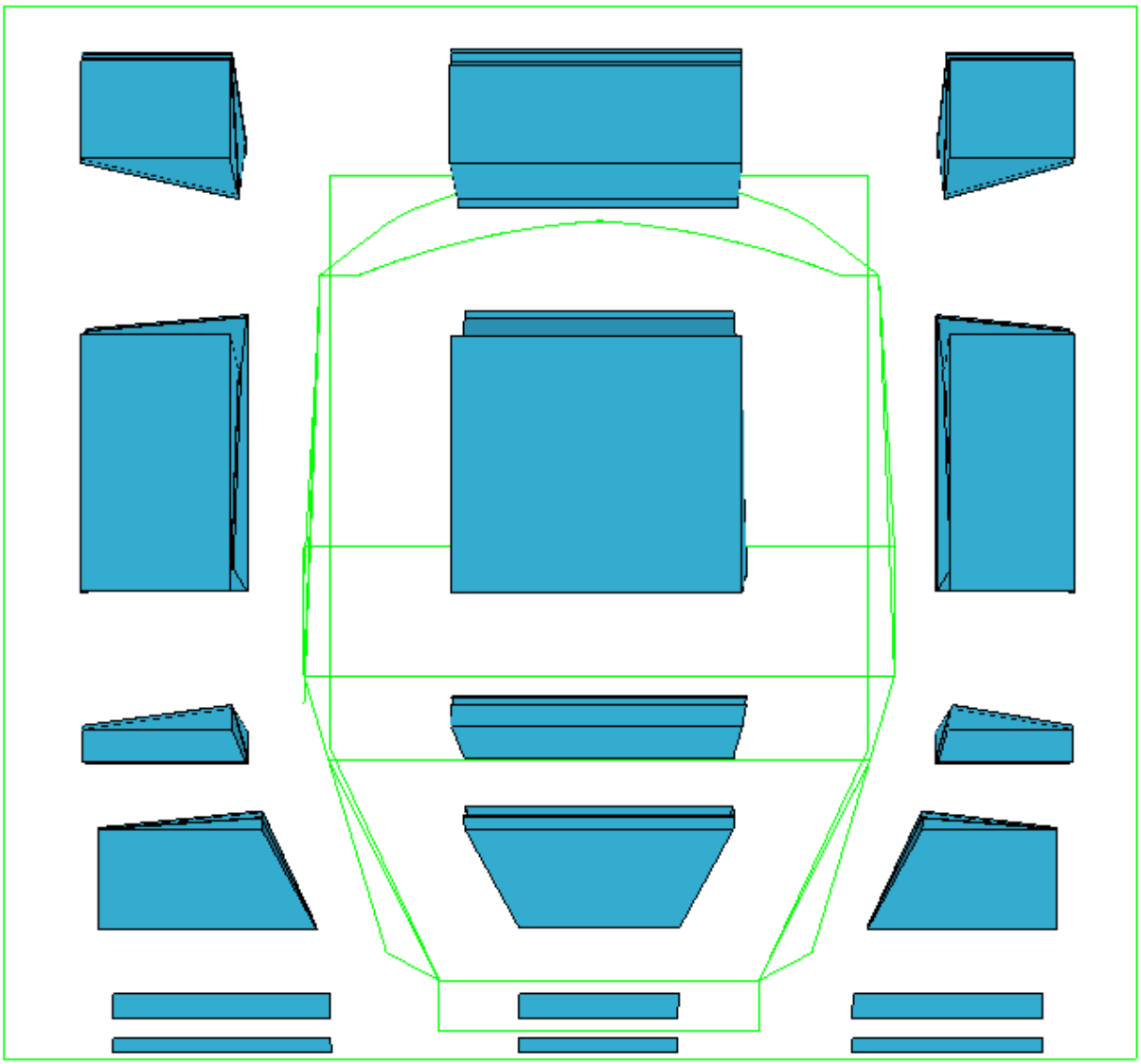

Figure C- 1: Moving domain; Distribution of blocks around the locomotive, in the vertical and lateral direction

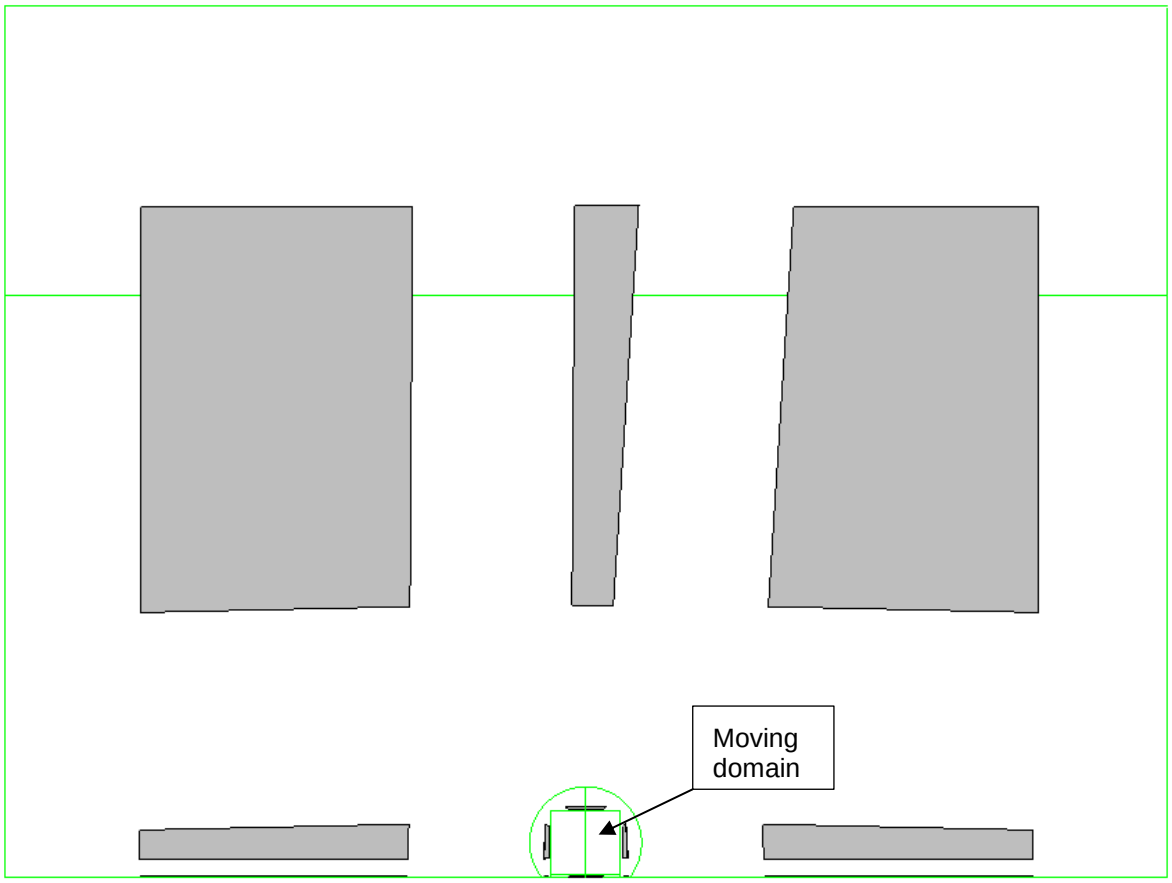

Figure C- 2: Stationary domain; Distribution of blocks outside of the moving domain, in the vertical and lateral direction

Appendix D: Ensemble average

Tunnel and entrance walls data

Figures D-1 and D-2 show the pressure histories at the tunnel walls. The initial pressure change is triggered by the compression wave. When comparing the three runs, insignificant differences are found for this wave, explained by small deviations of the train speed. For the remainder of the graph, areas with large oscillations indicate that the nose and tail pass by the measurement point. The most significant variations are observed due to the separated flow around the train which is turbulent and unstable.

However, the size of oscillations discussed above are relatively insignificant compared to the maximum pressure amplitudes, and three runs are enough for ensuring stability.

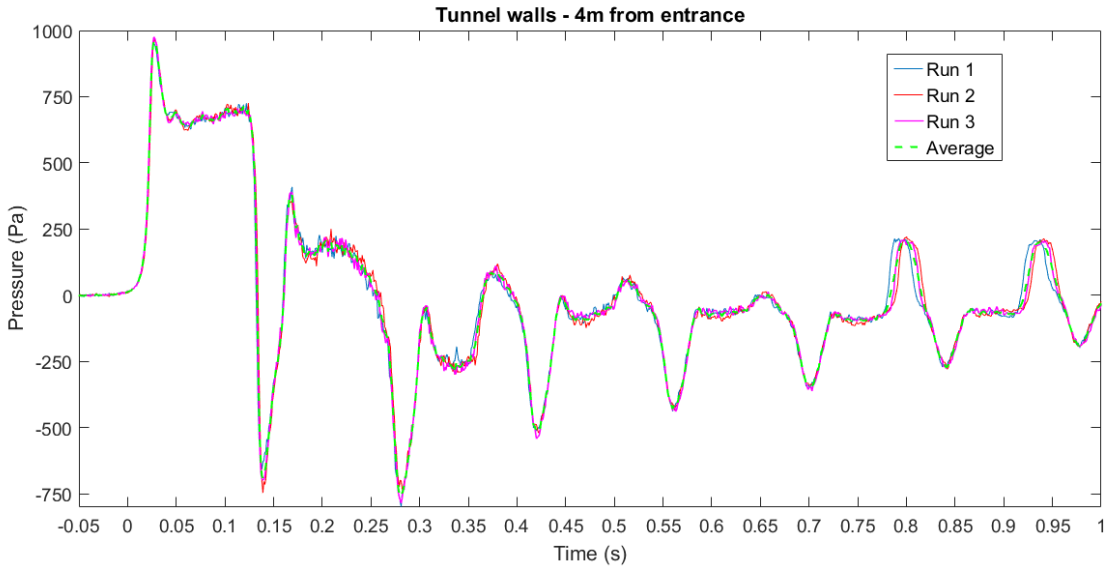

Figure D- 1: Repeatability of measurements at the tunnel walls

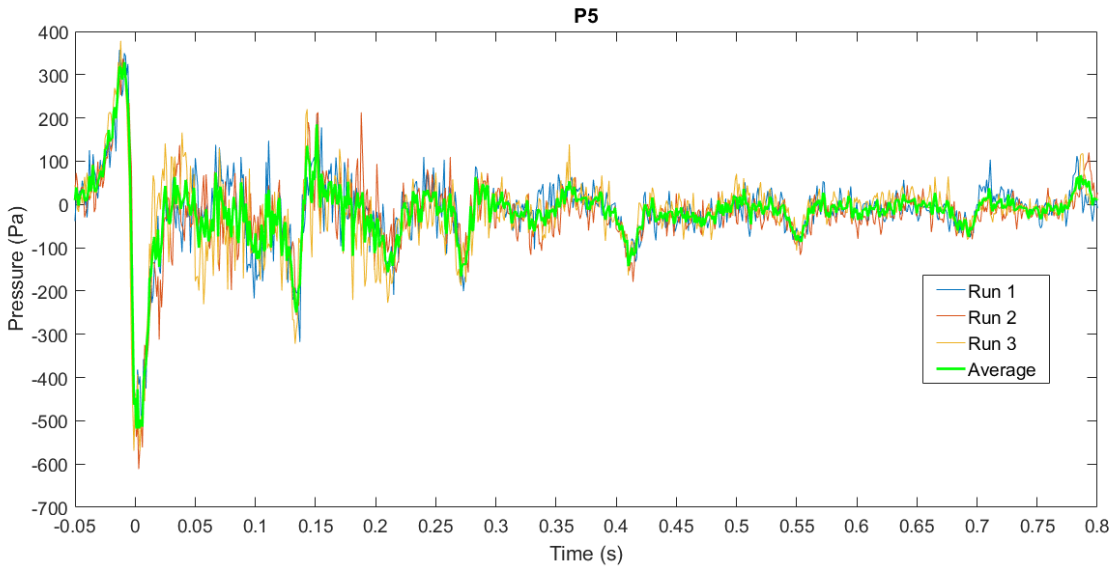

Figure D- 2: Repeatability of measurements at the entrance wall

Onboard data

Figures D- 3 to D- 5 below represent the pressure histories for 15 runs on the surface of the train. The flow becomes unstable when it comes in contact with the train surface, which is evident from the size of oscillations.

Tap 5 is located at the centroid of the train nose which is an air stagnation area. The pressure histories at this point are significantly more unstable when compared to the tunnel walls, maintained throughout the journey of the train through the tunnel (see Figure D- 3). This confirms that the oscillations are caused by the separated flow around the train and not from the pressure waves, as the latter are brought in contact with the measurement points periodically.

At the sides of the locomotive, tap 12 is located near the nose of the train (see Figure D- 4). Pressure histories are more stable compared to tap 5, although it is within the separated region.

The results confirm that for measurement points on the surface of the train, 15 runs are enough to ensure stability. This number of runs has also been confirmed through an ensemble stability analysis by Dorigatti (2013) and Soper (2014) who measured on-board pressures.

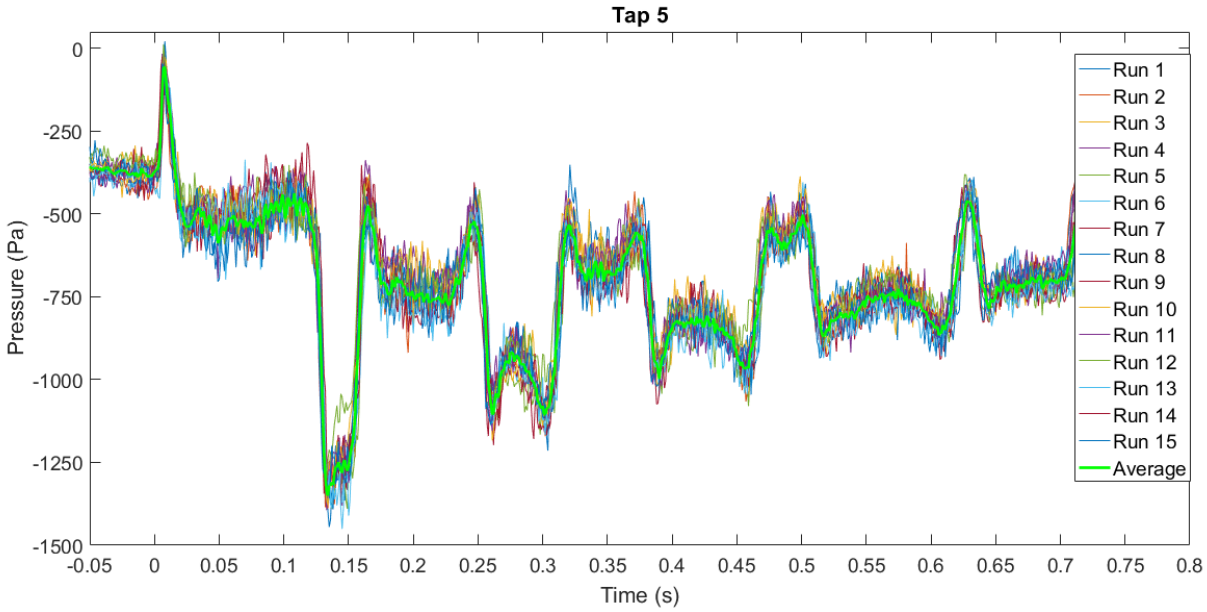

Figure D- 3: Repeatability of onboard measurements at the locomotive nose

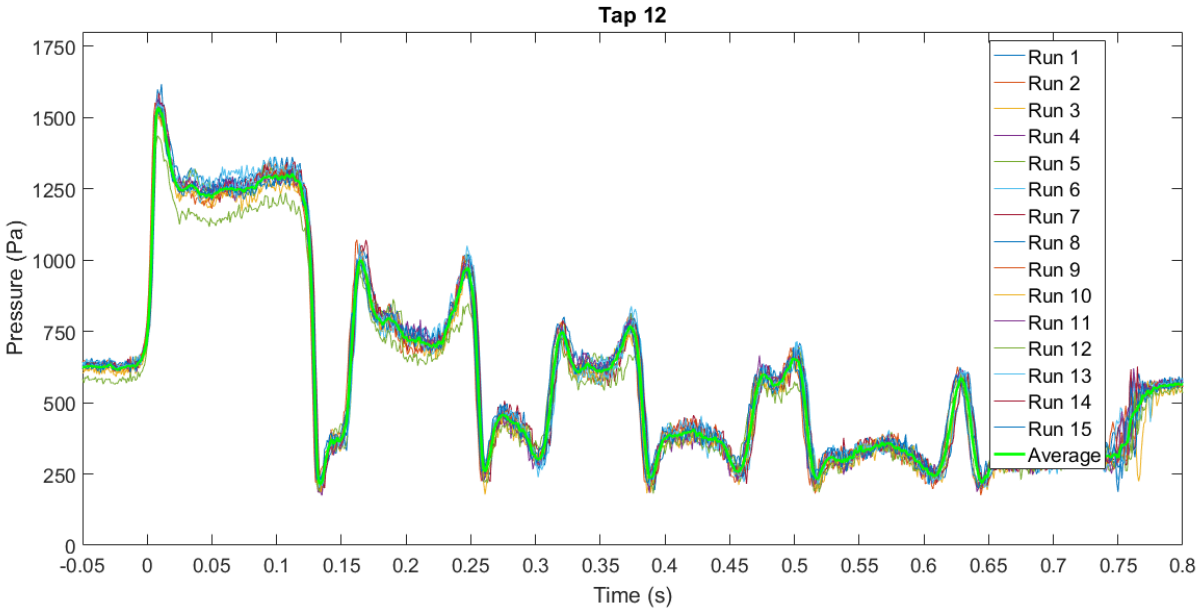

Figure D- 4: Repeatability of on-board measurements at the side of the locomotive (near the nose)

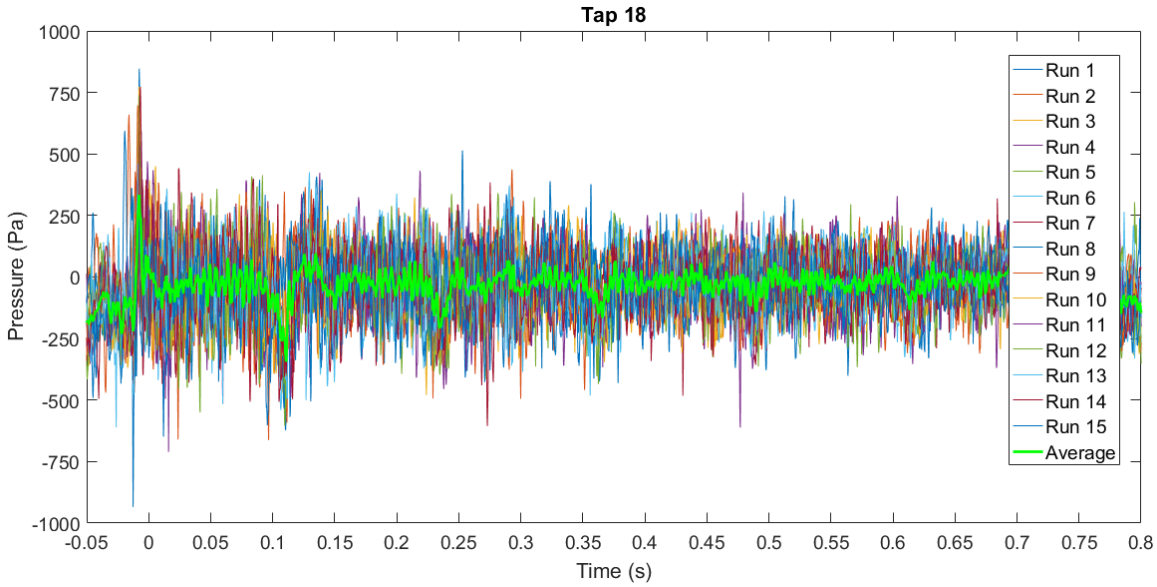

Figure D- 5: Repeatability of on-board measurements at the side of the locomotive (near the middle length)

Appendix E: Matlab code for 1D formulae

Calculating Δp_N for Nose 3

```
clc

rho=1.23; %air density kg/m^3

a=341; %speed of sound in m/s

vtrain=33.5; % train velocity in m/s

v0=0; %initial flow velocity in the tunnel in m/s

b=0.202; % geometric blockage ratio



ptun=400; %P1

pann=2.17; %P2

vann=vtrain-(-8.93); %V2 (relative velocity



kn=((ptun-pann)/(0.5*rho*vann.^2))-(2*b)+(b.^2); % eq. 27

alpha=((1+kn)/(1-b).^2)-1; %eq. 26



Dp=rho*c*((vtrain-v0)+(a/alpha)*(1-sqrt(1+(2*alpha*(vtrain-v0)/a))));    %
eq. 25
```